# Optimization of thin film flexible solar cell production process

Rahul Papriwal

Technical University Delft

TU Delft

# Optimization of thin film flexible solar cell production process

by

## Rahul Papriwal

to obtain the degree of Master of Science
at the Delft University of Technology,
to be defended publicly on Friday November 26, 2021 at 10:00 AM.

| | | |
|---|---|---|
| Student number: | 5132002 | |
| Project duration: | November 15, 2020 – November 26, 2021 | |
| Thesis committee: | Prof. dr. Arno. Smets, | TU Delft, ESE-PVMD, Supervisor |
| | Dr. Luana. Mazzarella, | TU Delft, ESE-PVMD |
| | Dr. Jianning. Dong, | TU Delft, DCE&S |
| | Dr. Gianluca. Limodio | TU Delft, ESE-PVMD, Daily supervisor |

An electronic version of this thesis is available at `http://repository.tudelft.nl/`.

# Acknowledgements

My first deepest gratitude is for Prof.Dr.Arno Smets who gave me an opportunity to work in his research group. I have been always been inspired by his work in the field of Solar Energy. It was his research work and courses in the Solar Energy track that inspired me to join TU Delft and work in this field. I will always be grateful to you for your support and motivation. Thank you for always guiding us.

I would like to express my thanks to my daily supervisor Dr.Davide Bartesaghi who has been the best teacher any student can ever imagine. I appreciate his patience and composure in explaining concepts to me. He has helped me develop and solidify my knowledge and background. I have learnt the art of researching and problem solving from him. Without his support I would have never been able to reach the goal of my thesis.

I would also like to thank Dr.Gianluca Limodio for his constant support and motivation. Thank you for always pushing us as calmly as possible. His guidance and willingness to share his vast knowledge has helped me understand the thesis in greater depths and complete the tasks on time.

The completion of this study would not have been possible without the expertise of Dr.Edward Hamers, under whose guidance we strive to excel. The motivation and inspiration received from him helped me progress ”hurriedly but as slowly as possible”.

I express my sincere gratitude to all the staff and operators at HyET Solar who have always helped me with a smiling face. Without their support I would have not learned so many skills.

I would like to thank my family. Thank you for providing me an opportunity to study in Netherlands, to learn and to grow. Your support has always pushed me to develop in life. Finally, my heartfelt thanks to all my friends who have been a constant support and have always motivated me to progress. I hope this thesis is just the start of my journey towards shaping a sustainable future and returning back to the society.

# Abstract

The quest for a cleaner and greener fuel has necessitated the development of renewable energy sources. Sun has been a source of energy for human civilization since agrarian times. With the recent developments in science and technology, Solar energy has evolved as the front runner to power the future energy needs. The plentiful, eco-friendly, and abundant solar energy resource has been evolved from the first generation solar comprising of crystalline silicon based solar panels to second generation photovoltaic cells.

This work is based on the scope of the FlamingoPV project which is the collaboration between TU Delft and HyET Solar, Netherlands, to realize large scale commercialization of second generation thin film flexible solar cells. The second generation solar cells offer flexibility, economic viability, and ease of manufacturing. To reach the desired goals of roll-to-roll production of a-Si:H/nc-Si:H and a-Si:H/nc-Si:H/nc-Si:H with stabilized efficiencies of 13% and 14% respectively, various production processes need to be optimized.

The current production line at HyET Solar faces losses in performance due to high open circuit resistance and low parallel (shunt) resistance. Moreover, the lab processing route needs to be optimized to improve the yield of the samples produced. The sputtering process of depositing the back contact is considered as one of the potential causes of low shunt resistances in the lab samples. Hence, the sputtering process is optimized for electrical and optical properties. The effect of sputtering pressure and RF power is understood to develop dense and compact films for the Aluminium doped Zinc Oxide (AZO) films used in the back contact of the solar cell stack. It is found that a lower sputtering pressure provides better optical and electrical properties. Furthermore, optical simulation from GenPro4 suggest an increase in intrinsic layer absorption under specific conditions of AZO deposition.

Furthermore, the monolithic series interconnection process at HyET Solar is a bottleneck in the lab processing route. Additionally, the laser power used for scribing is not optimized for tandem and triple junction solar cells. To ensure faster learning cycles for understanding the quality of the silicon layers deposited a novel way of processing solar cells is developed. This approach helps to distinguish various losses generated in the solar cell and ensures quality control in the production line. Finally, a series of triple junction solar cells deposited on the aluminum substrate is processed without laser scribing to demonstrate the possibilities of the process.

The PECVD tool at HyET Solar needs to be optimized to deposit good quality bottom cell for the micromorph solar cells. The continuous variable thickness series have been used to understand Lambert Beer relation for short circuit current density and deposition thickness. The ASA software is used to simulate case studies for troubleshooting deposition of the bottom cell. The results from the electrical simulation are used to understand the problems with the silane dilution ratios in the previous PECVD runs. Furthermore, the results of the simulation suggest the sensitivity of the process to ensure good quality nanocrystalline silicon deposition. It is observed that the first layer of growth is very critical for the nanocrystalline silicon deposition while after a certain thickness of nanocrystalline silicon inclusion of amorphous material does not affect the properties of the absorber layer.

Overall, the production process has been optimized from the lab scale to the industrial scale. One of the causes of low performance in solar cells has been addressed. The bottleneck in the production of lab samples has been addressed ensuring good quality material for faster learning cycles. The deposition conditions for the growth of nanocrystalline silicon have been analyzed. This can help in troubleshooting the production process and maintaining a high-quality deposition process.

# Contents

# List of Figures

# List of Tables

# Chapter 1

# Introduction

Throughout the course of human history, mankind has been worshipping the Sun. Human civilizations from ancient India, Egypt or China, the Aztecs in America or any other agrarian civilization can be seen worshipping the Sun in one form or another. The reason the Sun was worshipped was due to its ability to give warmth. Although over the years most civilizations may not worship the Sun in the same manner the human need for energy has been the same. With extensive development of science and the need for a cleaner fuel humans have realized Sun is the ultimate source of energy.

In the present scenario, solar energy is attributed as a key sustainable energy resource that can fuel developments of the future. With the ever-rising population and technological advancements there will be an increase in demand of energy. Environmental concerns and climate change have put pressure on conventional sources of energy to be sustainable. Solar energy which is readily available, plentiful and eco-friendly can fulfill the energy requirements of the future. Photovoltaic (PV) technologies which work on the principle of photovoltaic effect have gone immense technical breakthroughs in the past 20 years. These advancements have lead to reduction in cost of photovoltaic systems while improving the yield, efficiency and reliability of the technology [1]. These factors has resulted in exponential growth of PV power generation in the last decade. The cumulative installed PV power increased 30 times from 2009 to 2019 as seen in Figure 1.1. In 2019 PV installed power reached 635 GW$_p$ of which 130 GW$_p$was installed in the same year as seen in Figure 1.1 b. In 2019, 45% of the new global energy generation addition was through PV systems [1].

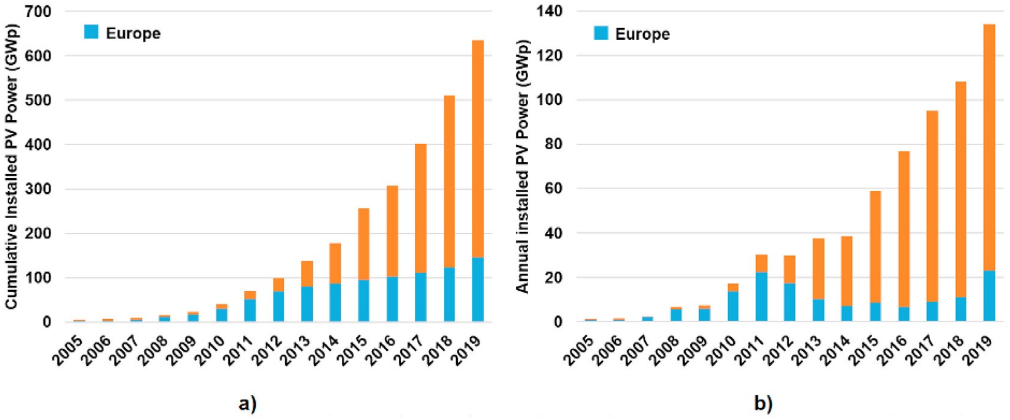

Figure 1.1: Photovoltaic development from 2005-2019: (a) Global Cumulative Installed PV Power (GW$_p$) (b) Global Annual Installed PV Power (GW$_p$) (Global values shown in orange, Europe values shown in blue) [1]

## 1.1 Photovoltaic cells

Photovoltaic cells or PV cells which can convert the Sun's solar radiation into electrical energy work on the photovoltaic effect. The incoming radiation from the Sun ionizes the region near the built-in potential barrier of the semiconductor by generating a potential. The system is characterized by the amount of current it can power to an external load. A potential barrier in a PV device can be formed by introducing a suitable impurities in the semiconductors. These impurities can then form the p and n semiconductor layers [2].

The p and n layers formed by doping impurities when brought in contact create a p-n junction with a electric potential between the p and the n type semiconductor layers. This electric potential helps the electrons to jump to n-type semiconductor and simultaneously the holes wander across the junction as seen in Figure 1.2. This migration of electrons and holes leave behind a static positive and negative charge. After a certain level, no more charge carrier migration can occur and a depletion zone is created at the p-n junction [3]. An electric field is created across the depletion zone due to the separated negative and positive static charges. This built in potential acts as a driving voltage for the current across the external circuit across a load. When photons from Sun radiation falls on the semiconductor layers, the energy from photons are transferred to the electrons. The highly excited electrons then move to the conduction band from the valence band, leaving a hole in the valence band. This absorption of energy results in a creation of electron hole pair. When connected to an external circuit, the voltage difference causes the electron to move towards negative direction and holes towards positive direction [4].

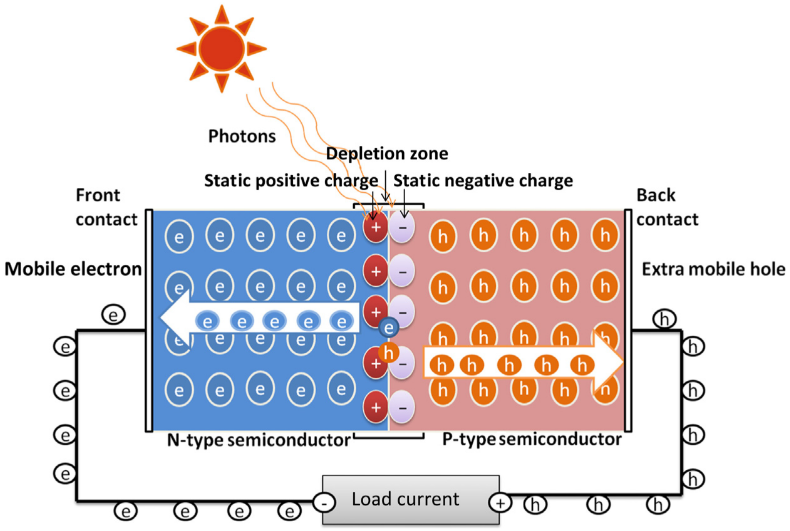

Figure 1.2: Schematic representation of a simple PV cell [3]

Based on the type of semiconductor, relative cost and efficiencies used the PV technologies can be broadly classified into 3 main classes called generations [5]. The first generation solar are the conventional wafer based cells which are made of crystalline silicon and hold around 90% market share as seen in Figure 1.3. The second generation solar were introduced as response to reduce the high material usage and cost of Silicon required for first generation solar cells. However, as seen in the Figure 1.3 second generation solar cells have seen a reduction in market share from 2015 to 2019 from about 6.5% to 5.4%. Third generation PV aims to bypass the Shockley-Queisser limit [**?**] which limits efficiency of single bandgap devices to 31% [6]. The following sections briefly discuss the different generations of PV technologies.

### 1.1.1 First generation PV cells

As it is already mentioned the first generation solar cells are manufactured using silicon wafers. It offers high power efficiencies which make it one the most popular technology for PV energy generation [7].

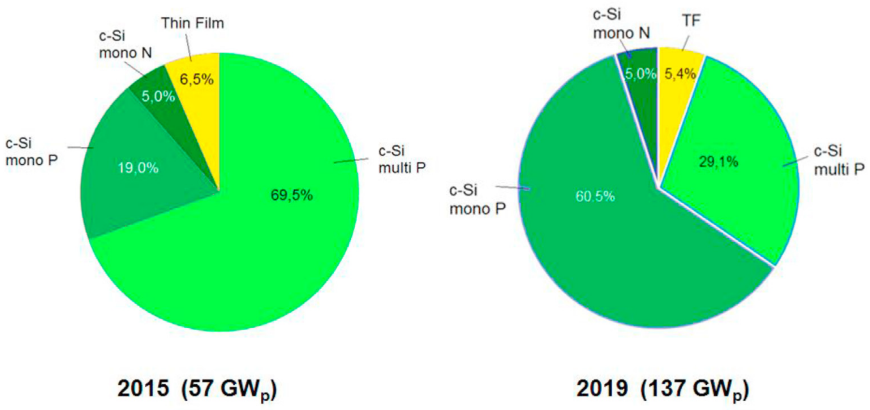

Figure 1.3: Comparison of different PV technologies by market share [1]

The silicon wafer technology can further be classified into two categories:

- Mono-crystalline silicon solar cells
- Multi-crystalline silicon solar cells

Mono-crystalline solar cells are manufactured from single crystals of silicon offering higher efficiencies of 17-18% generally. However, the manufacturing process for mono-crystalline is more complex and expensive as it requires a process of recrystallization. On the other hand, Polycrystalline or Multicrystalline technologies are cheaper to fabricate and requires different crystals coupled to each other in a single cell. The efficiency is the trade-off here, as the polycrystalline based technologies offer about 12-14% efficiencies [7].

### 1.1.2 Second generation PV cells

The thin film based solar cell technologies which were developed to provide economical advantage over silicon based first generation technologies are considered as second generation. The silicon based technologies comprise of 350 $\mu$m thick absorbing layers, while thin film technologies have absorber layers in the range of 1 $\mu$m or less [7]. This is advantageous as the high costs of silicon wafer, glass substrate and encapsulation of first generation technologies can be avoided in second generation cells. The thin film solar cells can be further classified into:

- a-Si (amorphous silicon)
- CdTe (cadmium telluride)
- CIGS (copper indium gallium selenide)

Thin film technologies offer a wide variety of depositing mechanisms like physical, chemical or plasma based technologies that can be used for deposition of the same type of material. Different types of electronic junctions, single or tandem junctions are feasible with thin film technologies [8]. However, thin films properties are highly sensitive to deposition parameters leading to problems in controlled manufacturing of the cells. Between the different thin film technologies, a-Si based thin films cells are the oldest, however, CdTe based solar cells are the current dominant thin film technology in the market [5]. CIGS based technologies are promising as they offer higher energy yield while having less payback time compared to other technologies.

### 1.1.3 Third generation PV cells

The third generation solar cells were developed to beat the Shockley-Queisser limit. These are promising technologies, however the commercial viability of these technologies has not been investigated [6]. The most developed third generation solar cell technologies are:

- Nano crystal based solar cells
- Polymer based solar cells
- Dye sensitized solar cells
- Perovskite based solar cells

To achieve efficiency improvements to go beyond the Shockley-Queisser, multiple energy threshold devices are required. Two power loss mechanisms in solar cells are single bandgap cells inability to absorb photons and thermalization of photon energies exceeding the bandgap [6]. With these third generation solar cells can utilize this lost energy through multiple threshold approach.

## 1.2 FLAMINGO PV

The work of this research falls in the scope of FlamingoPV which is a joint project between TU Delft and Hyet Solar, Netherlands. FlamingoPV stands for Flexible Lightweight Advanced Materials in Next Generation of PV. Hyet Solar is a Dutch PV manufacturer situated in Arnhem, the Netherlands. The deliverables of FlamingoPV are:

1. Lab-scale flexible a-Si/nc-Si:h PV cell (5 $cm^2$) and module (5x5 $cm^2$) with 13% stabilized module efficiency
2. Roll-to-roll production modules of 30x30 $cm^2$ of 12% aperture area stabilized efficiency with 80% production yield
3. Industry standard lifetime (>80% intial performance) convincingly proven for lifetime >35 years
4. Design and cost model for bottom cell PECVD tool with CAPEX < 0.2 MEuro/MWp
5. Lab-scale flexible a-Si:H/nc-Si:H/nc-Si:H PV cell (5 $cm^2$) and module (5x5 $cm^2$) with 14% stabilized module efficiency

These deliverables will ensure production of PV products which can compete with crystalline silicon technologies available in the market for large scale commercial and BiPV (Building Integrated Photovoltaic) applications. All of these deliverables have multiple subgoals which have been constantly discussed throughout this report to achieve the required deliverables.

## 1.3 Hyet process

The production process of HyET Solar, Arnhem comprises of a series of complex processing steps. The production process involves deposition of all the layers in house in Hyet solar. The production of flexible, thin-film solar modules done at Hyet Solar is called as *roll-to-roll* (R2R) manufacturing process. Here, an aluminium roll is used instead of glass as a temporary carrier on which further processing and deposition of subsequent layers is carried on. The temporary aluminium foil provides the advantage of having processing homogeneity and ease of scaling up the R2R production process. The Al foil also promotes the usage of high process temperatures which help in production of high-quality transparent conductive oxide (TCO) and photo-active silicon layers as shown in Figure 1.4 [9]. As discussed by E. Hamers et al the following section will discuss each step followed in the R2R production at Hyet solar briefly [9].

1. Al foil texturing - the aluminium foil used in processing is 350 mm wide. To enhance better light scattering crater like structures are created in the Al foil. These craters are created using wet-chemical etching where diluted NaOH is used to etch the Al foil creating craters. After the etching the Al foil is cleaned in acidic bath of $H_3PO_4$ to remove any resides from the etching.

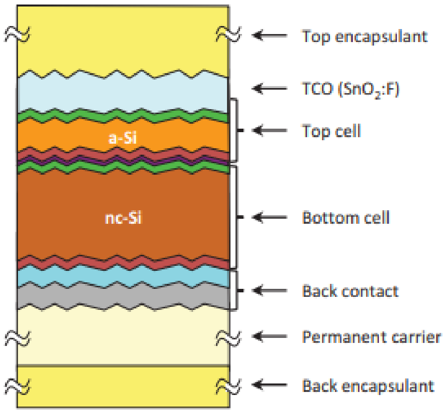

Figure 1.4: HyET Solar PowerFoil different layers for a tandem solar cell configuration [9]

2. Front TCO deposition - the HyET stack uses $SnO_2$:F layer as the front TCO layer which provides more stability against corrosion occurring from moisture and acid attack. The $SnO_2$:F is deposited using atmospheric pressure chemical vapor deposition (APCVD) technique on textured Al foil. The advantageous Al foil allows high temperature deposition at 500°C. A 750 nm of TCO is deposited in this process.

3. Silicon deposition - the silicon deposition is carried out as a single pass or multiple pass depending on the type of stack that needs to be deposited in a plasma-enhanced chemical vapour deposition (PECVD) technique. The silicon layer deposition occurs in superstate configuration where a RF frequency of 13.56 MHz and a temperature of 200°C is used. The deposition machines continuously deposit different layers like p-doped, intrinsic and n-doped layers in the different chambers. For a tandem solar module, a two pass approach is used where in the first pass top cell is deposited while in the second pass the bottom is deposited.

4. Monolithic series interconnection - laser scribing is used to define different cells constituting in a module. There are different scribes used to break different layers from adjacent cells. The first scribe is provided through FTO and a-Si:H layers which is then filled with an ink to separate adjacent cells electrically. The second scribe penetrates only the a-Si:H layer and connects the n- doped and p-doped layers of adjacent cells forming a series interconnection.

5. Back contact deposition - the back contact consisting of AZO/Al is deposited using sputtering technique. For AZO RF sputtering is used while for Al DC sputtering provides the required deposition. The typical thickness for AZO and Al deposited is around 70 nm and 300 nm respectively. The back contact also fills the scribes as discussed in monolithic series interconnection section. The lift-off ink as discussed previously is removed using a certain technique that helps in breaking the back contact from the adjacent cell.

6. Permanent carrier - the stack with the back contact is laminated on a permanent carrier foil to provide rigidity. The next step involves etching of the temporary Al foil exposing the active region on the front TCO. To ensure the mechanical stresses are transferred to a polymer material a encapsulation layer is used from the back.

7. Removal of Al substrate - wet-chemical etching is used to etch the temporary Al foil exposing the active region on the front TCO side.

8. Encapsulation - in the final step the modules are cut and encapsulated from the front side to protect from any moisture or chemical attack. Finally, the electrical connectors are added to finish the product.

## 1.4 Motivation of work

As mentioned in Section 1.2 the deliverables of the FlamingoPV project are motivation to carry out this research work. Among the several deliverables of the FlamingoPV, this work is majorly focused on the first deliverable. The goal of delivering lab-scale flexible amorphous silicon/microcrystalline silicon tandem cell (5 cm$^2$) and module (5x5 cm$^2$) with 13% stabilized module efficiency requires optimization of the lab processing line to demonstrate the efficiency on HyET Solar substrate.

The current lab processing at HyET Solar posses limited yield due to two factors, firstly, low electrical performance of the fabricated solar cells and secondly, due to bottleneck in the lab processing line. The Figure 1.5 and 1.6 depict the losses in the performance of the solar cells made in HyET lab route. The low efficiencies for single junction a-Si:H based solar cells are affected by the low shunt resistance as seen in Figure 1.5. Here, the solar cells with $R_p$ less than 0.5 k Ω cm$^2$ are shunted which limit the efficiency of the single junction solar cells to less than 6%. Moreover, the open circuit resistance component of the solar cell affect the efficiency as shown in Figure 1.6. The efficiency of the solar cell is limited by open circuit resistance which is factored by other resistance components like stack resistance, sheet resistance and laser interconnection resistance ($R_{lic}$). Here, the low performing solar cells have high open circuit resistance of more than 10 Ω cm$^2$, limiting the higher efficiency. Hence, one of the objective of the this work is to improve the lab scale yield and performance of the single junction and eventually the tandem solar cells produced at HyET Solar, Arnhem.

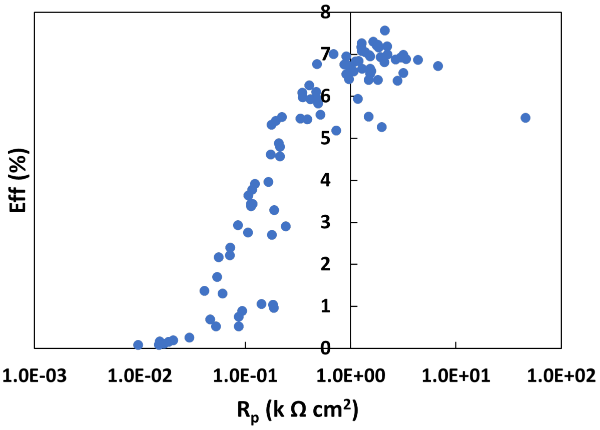

Figure 1.5: Performance measurements of lab samples produced at HyET Solar, Arnhem. Figure illustrating the effect of shunt resistance (logarithmic scale) on the efficiency of the solar cell [Data retrieved from HyET Solar]

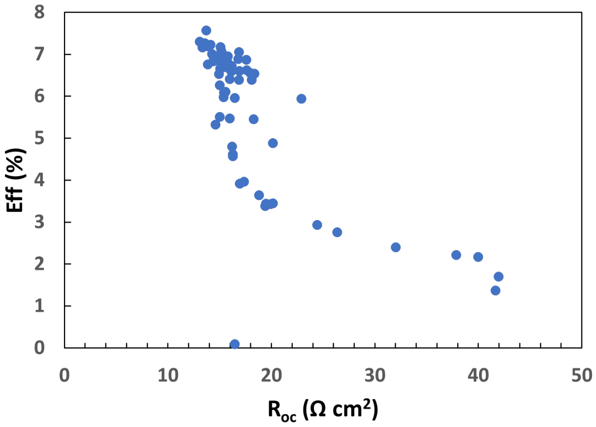

Figure 1.6: Performance measurements of lab samples produced at HyET Solar, Arnhem. Figure illustrating the effect of open circuit resistance on the efficiency of the solar cell [Data retrieved from HyET Solar]

Furthermore, the lab samples production at HyET Solar is further limited by the availability of laser scribing tool. The current configuration of the cells fabricated are cells on foil which require monolithic series interconnection process as discussed in Section 1.3. The cells on foil (CoF) configuration which will be discussed in later section, can have low performance due to various contributing factors of $R_{oc}$. The solar cells are more prone to shunting due to the laser interconnection process. Hence, to improve on the learning cycles and have cells which better feedback on the quality of absorber layers a new fabrication route needs to be developed. The new processing route should avoid the laser scribing process improving the throughput time while eliminating the effect of $R_{lic}$ on the performance of the solar cell. Overall, this would improve the learning cycle for depositing the absorber layers in the PECVD tool, hence, helping in demonstrate the last deliverable of FlamingoPV.

The second deliverable of FlamingoPV as discussed in Section 1.2 is to produce roll-to-toll modules sized 30x30 cm$^2$ with 12% aperture area stabilized efficiency and 80% production yield. To realize this goal, the PECVD tool at HyET Solar needs to be optimized to produce tandem solar cells with amorphous silicon/microcrystalline silicon absorber layers. Hence, the final objective of the thesis is to optimize the PECVD tool at HyET Solar to produce solar cells with the required efficiencies.

## 1.5 Thesis outline

To achieve the goals of FlamingoPV as discussed in Section 1.4 the production process needs to be optimized. A controlled high yield production process will enhance the learning cycles for developing and improving the efficiency of the product manufactured at HyET Solar, Arnhem. The main objective of this thesis is to improve the processing of amorphous silicon based solar cells manufactured in HyET Solar, Arnhem. The study has the following sub-objectives:

1. *Understanding the cause of low shunt resistance in lab processed solar cells*: this will provide insights in improving the shunt resistance and hence improving the overall performance of the solar cell
2. *Investigating the back contact sputtering deposition conditions*: the HyET Solar back contact sputtering tool has been updated over the years with mechanical and electrical parts. Hence, to find the optimal conditions for deposition of the back contact will improve the electrical performance and yield of the solar cells
3. *Developing a new processing route for fabrication of solar cells*: a new processing route will help improve the throughput time of the cells fabricated and improve the feedback on the material deposited, hence, providing better learning cycles
4. *Optimizing the deposition conditions for bottom cell for tandem configuration in the PECVD tool*: this will help in finding the optimum conditions for developing high efficiency solar cells

This thesis will guide the reader through the steps undertaken to reach these objectives. To begin, Chapter 2 introduces the fundamentals of amorphous silicon based solar cells, discussing the electrical replacements scheme. The electrical replacement scheme discusses various loss mechanisms in solar cells based on the series and shunt resistance parameters. Moreover, it discusses one of causes of high leakage current in amorphous silicon based solar cells. Chapter 3 discusses the various deposition techniques used to fabricate solar cells along with the various techniques used to characterize them. It also introduces various lab scale samples fabrication methods. Further, Chapter 4 describes the experiment conducted for optimizing the back contact sputtering process at HyET Solar. Finally, it discusses the results for the best deposition conditions based on electrical and optical analysis. Chapter 5 introduces the concept of SuperCoF (Super Cells on Foil) used as a new fabrication technique for solar cells. Here, two approaches are compared and then a final approach is selected. Moreover, Chapter 6 provides preliminary results for finding the optimum conditions for depositing the bottom cell for a tandem amorphous silicon/microcrystalline silicon based thin film flexible solar cell. Moreover, it discusses the problems with low performance of the previous runs at HyET Solar. Finally, Chapter 7 finalises with the conclusions of this research work along with further recommendations on future research directions regarding optimizing the production process.

# Chapter 2

# Fundamentals

## 2.1 Amorphous silicon

The growth of crystalline silicon solar industry in 2005-2008 was limited to the availability of pure silicon feedstock. This constraint opened up new opportunities for thin film technologies as the raw material requirements were comparatively less than wafer based technologies. Among the different approaches in thin film photovoltaics, amorphous hydrogenated silicon (a-Si:H) proved to be advantageous due to short energy payback time, facilitating the use of low cost substrate materials an fabrication using abundant raw materials with no economical risk [10].

### 2.1.1 Structure of amorphous silicon

Amorphous silicon as the name suggests lack order over longer distance over the crystal lattice. The crystallinity is not maintained and deviations become large over longer range as seen in Figure 2.1. However, amorphous solids have short-range order. As seen from the Figure 2.1 (a) the atoms (small circles) have neighbours in almost same position as in corresponding crystal (broken line) [11].

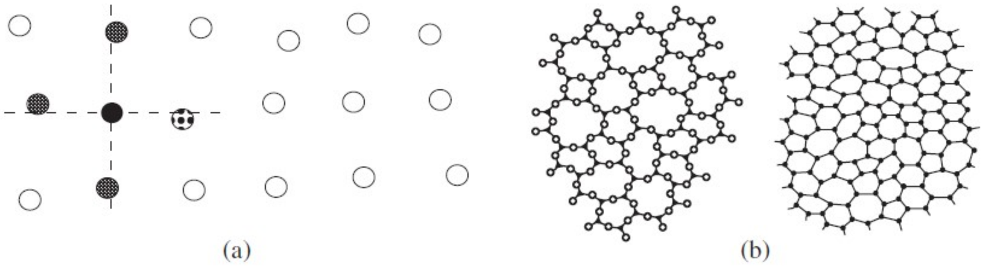

Figure 2.1: Schematic two-dimensional figure of amorphous silicon solid material structure: (a) diagram suggesting atoms (small circles) have nearest neighbours in same position as crystalline structure (broken line); (b) diagram suggesting larger disorder in amorphous silicon structure [11]

The atomic disorder in short range atomic configuration as suggested in Figure 2.1 (b) leads to certain amount of disorder in the lattice. The disorder can affect the bond length and bond angle distributions. For crystalline silicon the bond angle between adjacent Si-Si- atoms is 109°28' as seen in Figure 2.2. However, for amorphous silicon we have a bond angle with a standard deviation of 6° to 9° [11]. The same trend follows for bond length for crystalline silicon it is fixed at 0.235 nm while for amorphous silicon, one finds a random distribution around the crystalline silicon value.

A highly disordered material consists of varying bond angles and bond lengths. This is typical nature of amorphous silicon where a high disorder leads to high density of ”mid-gap defects” or ”dangling bonds” which makes it unsuitable for fabrication [11]. These dangling bonds are material defects which

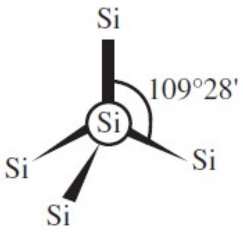

Figure 2.2: Atomic model for crystalline silicon [11]

results in missing bonds where a silicon atom will be bonded to three neighbouring atoms instead of four as shown in Figure 2.3 (a). Dangling bonds have electronic states near the mid gap and act as recombination centers. For fabrication of a-Si devices under Plasma-Enhanced Chemical Vapor Deposition (PECVD) a large proportion of dangling bonds are passivated by hydrogen which comes from the use of silane (SiH4). The passivated dangling bonds do not act as recombination centers as shown in Figure 2.3 (b). Amorphous silicon without hydrogenation or passivation would have very high defect densities (>$10^{19}$ $cm^{-3}$) resulting in fast recombination of the photo-excited charge carrier [12]. Hence, hydrogenation passivates defects in materials leading to defect densities around $10^{16}$ $cm^{-3}$ making the material suitable for PV applications [12].

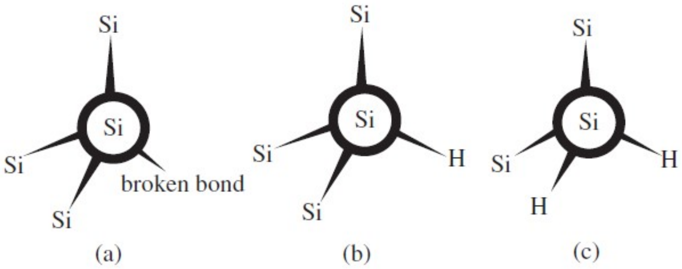

Figure 2.3: Model for silicon atom with : (a) unpassivated dangling bond; (b) passivated dangling bond ; (c) two hydrogen atoms connected [11]

### 2.1.2 Stabeler-Wronski effect

The first development of a-Si:H solar cells was reported by Carlson and Wronski in 1976 [10]. However, a year later a severe drawback was observed which suggested light induced degradation of a-Si:H called as Staebler and Wronski effect (SWE). This effect suggested that after certain hours of exposure to light the efficiency of a-Si:H solar cells decreases until it reaches a saturation level. As discussed in Section 2.1.1 the silane flow can help with passivation of dangling bonds, however if the silicon atoms in hydrogenated amorphous silicon (a-Si:H) gets bonded with two hydrogen atoms as shown in Figure 2.3 (c) we can observe a pronounced light induced degradation effect [11].

### 2.1.3 a-Si:H based solar cells

The bandgap of amorphous silicon can be tuned with the amount of hydrogen fusing in the silicon network of the material. However, the usual bandgap for amorphous silicon is in the range of 1.6 eV up to 1.8 eV. Amorphous silicon has a higher bandgap than crystalline silicon ( 1.12 eV) due to the distortions in bond angle and bond lengths as discussed in Section 2.1.1. However, the bandgap of nanocrystalline silicon is close to that of crystalline silicon due to the crystalline network in the grain structure [12]. Nanocrystalline (also known as microcrystalline) are materials which are in between the well organized structure of crystalline silicon (c-Si) and the disordered one of a-Si. The nanocrystalline silicon phase consists of grains which can vary in the range of nanometers upto microns.

The amorphous disordered structure of amorphous silicon results in a poorly defined electron momentum in comparison to that of crystalline silicon. Hence, amorphous silicon is a direct bandgap material while crystalline silicon is indirect bandgap material. Therefore, the absorptivity of a-Si:H in the visible spectrum is higher than that of crystalline silicon as shown in the Figure 2.4 [12]. As suggested from the figure in certain wavelength regions like the visible region the higher absorption allows for a thinner silicon film to be used in comparison with crystalline silicon. The Figure 2.4 also shows the absorption coefficient of a-SiGe:H which is even higher than a-Si:H.

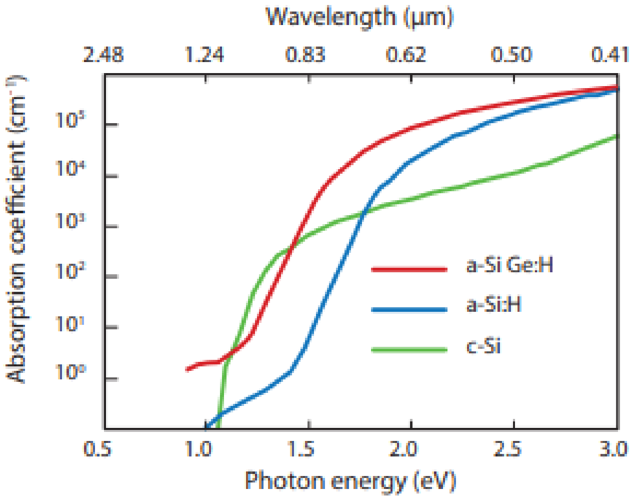

Figure 2.4: Absorption coefficients of different thin-film silicon materials[12]

### 2.1.4 Design of thin-film silicon solar cells

As already discussed in Section 2.1.1 the disordered structure of amorphous silicon result in dangling bonds which act as a defect site. These defects can limit the lifetime of light excited charge carriers which can be described by the Shockley-Read-Hall recombination [12]. Due to lower lifetime of the charge carriers the diffusion length is around 100 to 300 nm. Hence, the transport charge carriers cannot rely on diffusion in a thick absorber material.Therefore, a-Si:H based solar cells are not based on p-n junctions. Instead an undoped intrinsic layer is sandwiched in a p-i-n configuration as shown in Figure 2.5 [12].

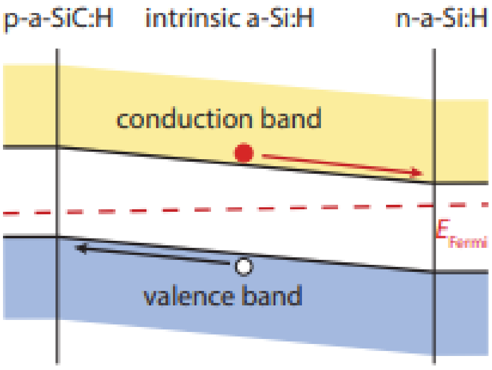

Figure 2.5: Band diagram of amorphous silicon solar cell[12]

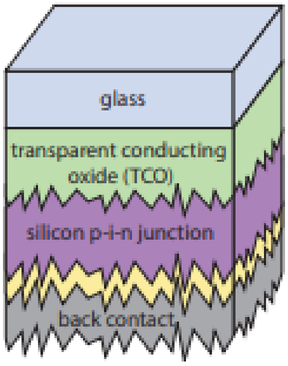

Figure 2.6: Single junction amorphous silicon solar cells layers[12]

Here since all the layers are connected the fermi level has to be same throughout the junction. The slope in the intrinsic layer electronic band reflect the built-in electric field. It is due to this electric field the holes move up in the valence band towards the p-a-SiC:H layer while the electrons move down in the conduction band towards the n-a-Si:H layer. This electronic drift act as the dominant transport mechanism making a-Si:H devices as drift device. Furthermore, due to low diffusion length of p-layer and n-layer, both the layers must be thin. The dominant transport mechanism in p-layer and n-layer is through diffusion.

#### Single junction amorphous silicon solar cells

The single junction amorphous silicon solar cell stack is show in Figure 2.6. The following stack is deposited in p-i-n superstate configuration suggesting the first deposited layer is where light is incident first on the solar cell. On a substrate like glass before p-i-n deposition, a transparent front contact made from transparent conducting oxides (TCO) needs to be deposited. The Figure 2.6 represent texturing which help light absorption across the absorber layers. Furthermore, the p-type layer is usually made with materials with higher bandgaps such as silicon oxides or silicon carbides doped with boron in order to reduce the parasitic absorption in the ultraviolet part of the light spectrum [12]. For n-layer a-Si:H can be used with phosphorus as the dopant.

However, due to bandgap of amorphous silicon which is in order of 1.75 ev only wavelengths shorter than 700 nm are absorbed [12]. The maximum current density that has been achieved by single junction amorphous silicon based solar cell is around 17 to 18 mA/cm$^2$ with an External Quantum Efficiency (EQE) averaged over the spectrum of 74 to 77%. Therefore to optimize the spectral utilization multi-junction approach is used. Here, a nanocrystalline silicon film can be used in a tandem structure with amorphous silicon films to form a micromorph solar cell.

#### Micromorph silicon solar cells

Figure 2.7 shows a band diagram for micromorph solar cells. On the left side of the Figure 2.7 is the band diagram for amorphous silicon where the short wavelengths are absorbed. While right side of the same figure depicts the bottom cell with nanocrystalline silicon which absorbs the red and infrared wavelengths [12]. In both the top cell and bottom cell electron and hole pairs are generated. The holes in the top cell drift towards top of p-layer and electrons in the bottom cell drift towards bottom of n-layer where they are collected by the front and back contacts respectively. The remaining electron and hole from the top cell and bottom cell respectively are recombined in a tunnel recombination junction (TRJ) which is placed in between both the cells. A thin defect rich layer made of silicon oxide can be used for TRJ. The total current density for the cell would be dominated by the current density of cell which is lowest. Hence, it becomes important to match the current densities of both the cells by using techniques like light management.

## 2.2 Electrical replacement scheme

The equivalent circuit model is used to evaluate performance of solar cells by predicting the voltage and current outputs. It uses an equivalent electrical circuit with temperature and radiation dependent components to predict the performance [13]. The following section briefly discusses the electrical model as developed by E.Hamers et al in HyET Solar to formulate the equivalent circuit model. This model will be used to understand the electrical parameters of solar cells fabricated at HyET Solar and optimize the yield and performance.

### 2.2.1 Ideal diode

As discussed in the previous sections, thin film a-Si:H cells are p-i-n junctions which are fabricated as thin semiconductors. When these junctions are exposed to light which has photon energy greater than

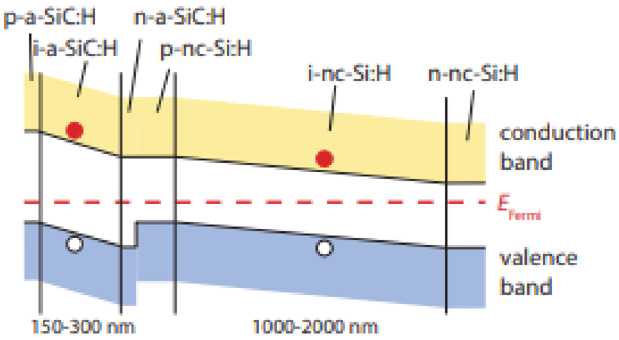

Figure 2.7: Band diagram of micromorph silicon solar cell[12]

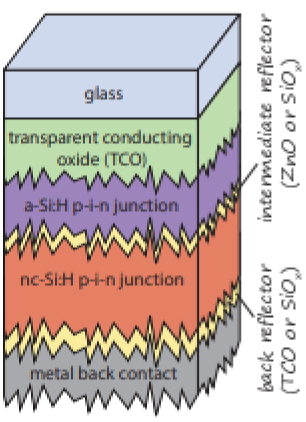

Figure 2.8: Micromorph silicon solar cells layers[12]

that of the bandgap of the semiconductor material used, then a photo current is generated [14]. This photo current is proportional to the amount of solar radiation that is incident on the solar cell. However, under the dark conditions, the IV characteristics of the PV cell is similar to that of diode as seen in Figure 2.9. The current density (J) through the diode under the application of an applied voltage (V) is describe by the Eq 2.1.

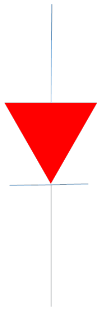

Figure 2.9: 1D solar cell equivalent circuit with only diode (red)

$$J = J_0 \left[ \exp\left(\frac{eV}{nkT}\right) - 1 \right] \tag{2.1}$$

Here, $J_0$ is the dark current of the diode, n is the ideality factor, k is the Boltzmann constant and T is the temperature.

### 2.2.2 Adding a linear parallel resistance

A non-ideal contribution forming between the front and back contact is added in parallel to the diode as shown in Figure 2.10. This parallel resistance is also called as shunt resistance. Shunts are leakage current in low forward biases occurring under dark conditions [15]. a-Si:H based solar cells are notoriously known for their low shunt resistances, affecting the current and voltage parameters under dark. So ideally we want a solar cell with high shunt resistance so to avoid high leakage current.

Here, in Eq 2.2 we see the added contribution of a parallel shunt resistance. Here the extra added term $\frac{V}{R_p}$ is the linear contribution of the shunt resistance. In the case where V<0, the contribution of the diode is small and shunting may dominate the current.

$$J = J_0 \left[ \exp\left(\frac{eV}{nkT}\right) - 1 \right] + \frac{V}{R_p} \tag{2.2}$$

Here $R_p$ is the ohmic shunt resistance. It can be seen from Figure 2.11 that increasing the shunt resistance improves the solar cell performance since there is more resistance to leakage current.

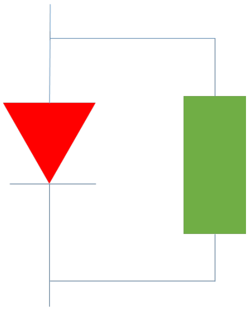

Figure 2.10: 1D solar cell equivalent circuit with diode (red) and shunt resistance (green)

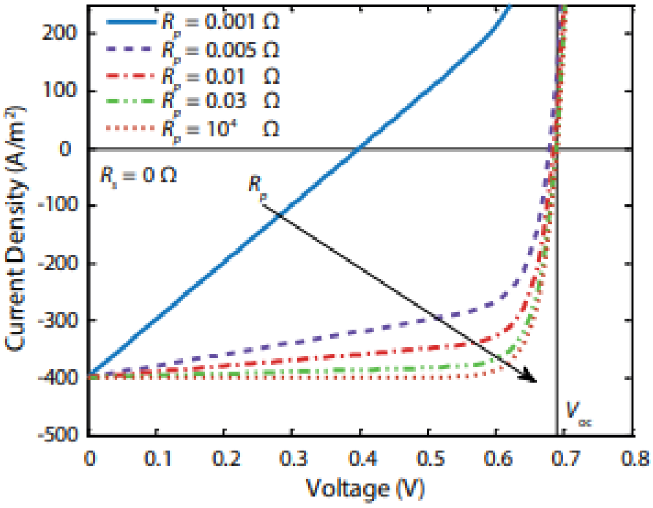

Figure 2.11: Effect of shunt resistance on J-V characteristics of solar cells [12]

### 2.2.3 Adding a non-linear parallel resistance

The linear addition term of shunt resistance as discussed in Section 2.2.2 is insufficient to describe the dark current measured. Hence, a non-linear term is added it to the shunt resistance to understand the dark current measured.

$$J = J_0\left[\exp\left(\frac{eV}{nkT}\right) - 1\right] + \frac{V}{R_p} + \frac{V^3}{R_{ppp}} \tag{2.3}$$

Hence, the added term $\frac{V^3}{R_{ppp}}$ helps in explaining the behaviour observed under the dark current measurements. Here, $R_{ppp}$ is the non-ohmic shunt resistance. $R_{ppp}$ is expressed in kOhm cm$^2$ V$^2$.

### 2.2.4 Adding photo-current with recombination

The effect of light falling on the solar cell intrinsic layer will generate electrical current. As we increase the intensity of light we increase the photo-generated current proportionally. The light that falls on the absorber layer will excite electron from valence band to the conduction band of the semiconductor. Similarly, the hole is left behind in the valence band. Figure 2.12 depicts a 1D condition where a photo-current source is placed in parallel to the diode and the shunt resistance.

$$J_{ph} = J_{pho}\frac{V_{bi} - V}{V_{mu}}\left[1 - \exp\left[-\frac{V_{mu}}{|V_{bi} - V|}\right]\right] \tag{2.4}$$

The photo-generated current $J_{ph}$ as shown by Eq 2.4 is adopted from internal literature of HyET Solar. Here, the terms $V_{bi}$ is the built in voltage, $V_{mu}$ represents the recombination voltage and $J_{pho}$

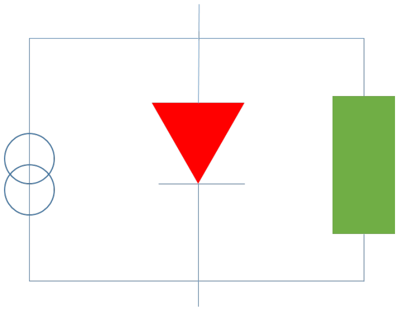

Figure 2.12: 1D solar cell equivalent circuit with diode (red) , shunt resistance (green) and parallel current source

is the starting photocurrent density. To find the current density for solar cell under illumination we can add the Eq 2.3 and Eq 2.4.

$$J = J_0 \left[ \exp\left( \frac{eV}{nkT} \right) - 1 \right] + \frac{V}{R_p} + \frac{V^3}{R_{ppp}} + J_{pho} \frac{V_{bi} - V}{V_{mu}} \left[ 1 - \exp\left[ -\frac{V_{mu}}{|V_{bi} - V|} \right] \right] \tag{2.5}$$

So the current density can be expressed in terms of diode current, shunt resistance and the photo-generated current as follows:

$$J = J_d + J_{Rp} + J_{R_{ppp}} + J_{ph} \tag{2.6}$$

### 2.2.5 Adding series resistance

The series resistance is added in 1D to complete the equivalent circuit. The series resistance has contributions from various factors which will be discussed in further sections. The current generated in the parallel circuit will induce a voltage drop over the series resistor as shown in Eq 2.7.

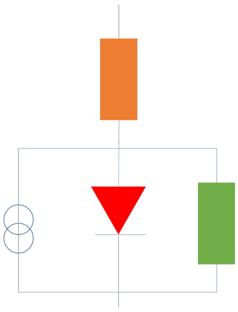

Figure 2.13: 1D solar cell equivalent circuit with diode (red) , shunt resistance (green), parallel current source and series resistance (orange)

$$J = J_0 \left[ \exp\left( \frac{e\,[V_a - JR_s]}{nkT} \right) - 1 \right] + \frac{[V_a - JR_s]}{R_p} + \frac{[V_a - JR_s]^3}{R_{ppp}} + J_{pho} \frac{V_{bi} - [V_a - JR_s]}{V_m} \left[ 1 - \exp\left[ -\frac{V_{mu}}{|\,V_{bi} - [V_a - JR_s]} \right] \right] \tag{2.7}$$

However, it is important to note here the effect of series resistance on the fill factor as can be seen from the Figure 2.14. The JV parameters decrease with an increase in the series resistance which affect the fill factor. For large values of R$_s$, the short circuit density is reduced. Hence, to optimize the efficiency of solar modules, R$_s$ should be kept as low as possible.

## 2.3 Shunt resistance

Thin-film amorphous silicon p-i-n offer superiority over crystalline silicon solar cells considering their lower manufacturing and installation costs. However, thin-film amorphous silicon cells are notoriously

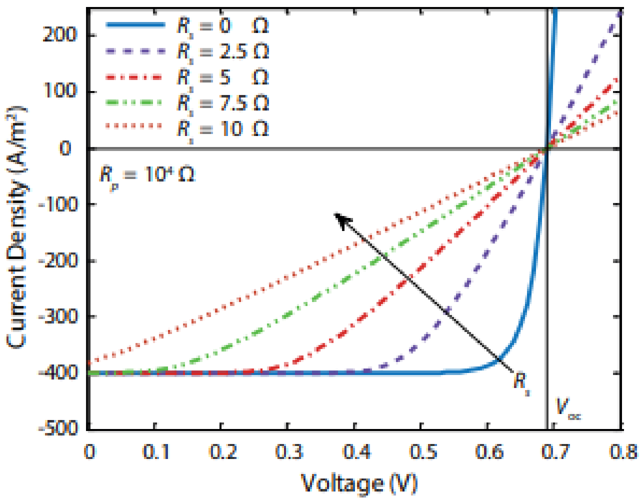

Figure 2.14: Effect of series resistance on J-V characteristics of solar cells [12]

known to exhibit high leakage current at low forward and reverse biases as discussed in Section 2.2.2 [15]. The phenomena of this leakage current is known as shunt current. The importance of understanding the physics behind the shunt current is to improve the module output hence improving the cell efficiency.

Shunts have been characterized by non-uniformity's caused by debris on the panel surface during the deposition process. The shunts which are caused due to deposition conditions are known as extrinsic shunts and can be reduced by controlling the deposition conditions. These extrinsic defects are macroscopic in nature and are visible on the surface of the film (for example: pinholes) However, even with the optimum deposition conditions, significant shunts are observed in the cells degrading the performance [16]. These are intrinsic type of defects which cannot be attributed to any visible defect or non-uniformity. These intrinsic shunts can be observed as bright spots under dark thermography imaging. Such methodology of imaging is used to understand the shunt nature.

### 2.3.1 Types of shunts

Breitenstein et al in 2004 used precision lock-in thermography techniques to understand the types of bright features visible in solar panels. Nine different types of shunts have been identified for solar cells using scanning electron microscope (SEM) and transmission electron microscope (TEM). Two types of shunt formation has been discussed in literature, namely, process induced shunts and material induced shunts [17].

- Process induced shunts [17]

  1. Linear edge shunts - These shunts are dominant where edge isolation technologies are not predominant. In the current solar cell technologies this type of shunt is not frequent.
  2. Nonlinear edge shunts - These shunts have nonlinear IV characteristics. They have recombination sites at the edge of the surface. They have high ideality factor of 3 and above.
  3. Cracks and holes - Cracks can be generated while processing or be present in the material beforehand. These are ohmic shunts where an emitter layer gets established across the crack forming a linear shunt. Pinholes can be generated during post processing techniques like laser cutting.
  4. Schottky type shunts - These may occur if sintering of emitter metalization is not optimized and it goes out of the emitter leading to Schottky type contact between n-type material base and the metal. It may also occur if emitter metalization is printed at position where there is no emitter layer at all. It does not have an ideality factor of unity.

5. Scratches - These bring the p-n junction to the surface resulting in high recombination centers. They are nonlinear type of shunt and they have large ideality factors.
6. Aluminium particles - Whenever aluminium particle reaches the front surface of the absorber layer it create shunt path.

- Material induced shunts [17]
    1. Strong recombination crystal defects - It is observed that normal grain boundaries do not lead to shunts, however, if crystal defect is strong enough the recombination current can become a shunt.
    2. Macroscopic inclusions - If a solar cell is processed from material that contain macroscopic inclusions then a nonlinear IV characteristics for the shunt is observed.
    3. Inversion layer at precipitates - This occur when a local transformation of material happens from n-type to p-type, caused by presence of fixed positive charges in the corresponding grain boundaries.

Breitenstein at al suggested that a key experiment for identifying shunts is the comparison of lock-in thermography imaging taken under forward and reverse bias. Moreover, it is further observed that linear shunt can become an inversion channel for conversion of n-type material into p-type, if its not an underlying hole or crack. Furthermore, shunts with nonlinear characteristics are attributed to be recombination shunts caused by surface states or crystal defects [17].

### 2.3.2 Space charge limited shunt current

Shunt current (I$_{sh}$) in initial literature was attributed to be ohmic in nature caused due to microscopic pinhole defects. All the thin-film solar cell technologies like amorphous and microcrytsalline (a-Si:H/$\mu$c-Si:H), cadmium telluride (CdTe), copper indium gallium diselenide (CIGS) and organic photovoltaics (OPVs) have shunting affecting performance consistency in excess variable dark leakage current at low biases [18]. However, with further experiments 3 key empirical features for shunt were attributed which could not be explained by classical explanation of ohmic shunt caused by pinhole defects. The results of phenomenological model as suggested by Dongaonkar et al characterized three key empirical features, namely I$_{sh}$ being symmetrical about V=0, leakage current showing non-linear voltage dependence and weak temperature dependence of shunt current in a-Si:H based solar cells [15].

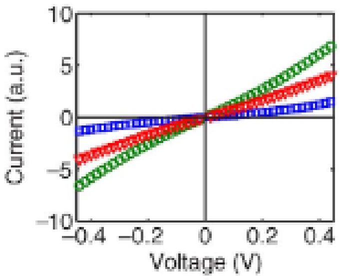

Figure 2.15: Symmetry of leakage current at V=0 for 3 identical cells [15]

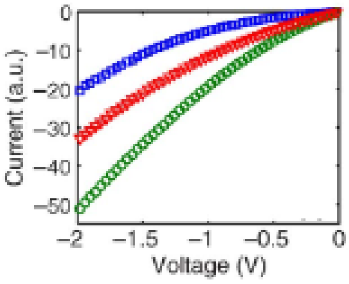

Figure 2.16: Non-linear dependence on voltage of the leakage current for 3 identical cells [15]

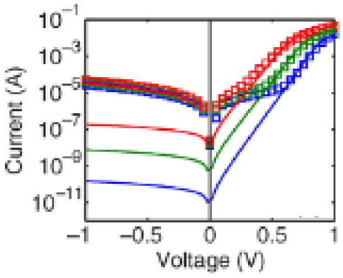

Figure 2.17: Temperature dependence IV curve for one device at 45°C, 85°C, 120°C [15]

#### A. Phenomenological Model

The three key empirical features presented by Dongaonkar et al as shown in Figure 2.15,2.16 and 2.17 present contrasting results from a rectifying p-i-n diode structure. The results shown in the figure are from single junction a-Si:H devices manufactured by PECVD process with ZnO:Al as the top contact. The features of I$_{sh}$ were further analyzed to be reproducible and statistically robust in large-area cells establishing I$_{sh}$ as a parasitic current [16]. The ohmic shunt caused by pinhole defects could capture the voltage symmetry and weak temperature dependence of I$_{sh}$, the ohmic nature could not explain the power dependence law [16]. The transport mechanism through space-charge limited (SCL) current (I$_{SCL}$) could capture all the features observed for I$_{sh}$.

$$I_{\text{SCL}} = A\varepsilon\mu_c(\gamma)\frac{V^{\gamma+1}}{L^{2\gamma+1}} \tag{2.8}$$

The SCL transport features single-carrier transport in a symmetric structure like metal/semiconductor/metal is showed in general form in Eq 2.8 [16]. Here, L is the thickness, $\epsilon$ is the dielectric constant, A is the area of the cell while $\gamma$ is a function of trap distribution inside the bandgap and captures the observed non-linear voltage dependence of I$_{sh}$. Here, it is observed weak temperature dependence of I$_{sh}$ as the only parameter because mobility depends weakly on temperature. The SCL current model explains the conduction through localized shunt path which explain the electrical properties of I$_{sh}$, however the physical origin of shunt path requires further analysis.

### B. Localized p-i-p shunt model

To understand the physical origin of parasitic symmetric shunt path that creates a SCL shunt path, Dongaonkar at al proposed a hypothesis which suggests formation of localized p-i-p structure doing cell fabrication. For a-Si:H cell that is deposited on fluorinated tin oxide (FTO) with aluminium-doped zinc oxide (AZO) top contact a p-i-p structure can be created due to local incursion of Al from AZO in the semiconductor layer as shown in the Figure 2.18. This would result in creation of a parallel localized current path in addition to the bulk exponential diode current.

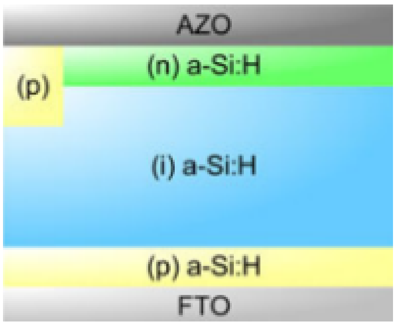

Figure 2.18: Proposed p-i-p structure causing a shunt path [16]

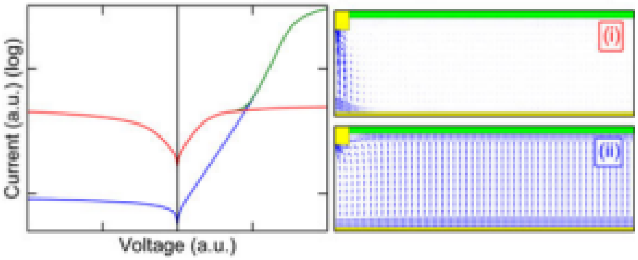

Figure 2.19: Dark IV simulations showing shunt (red), diode (blue) and total current (green). Furthermore, Quiver plots showing current condition in p-i-p structure in (i) at low bias while diode conduction ; in (ii) at high bias [16]

A numerical stimulation in 2-D structure was carried out using commercial Synopsys Medici TCAD software, to reproduce essential feature of SCL shunt as shown in Figure 2.19. It can be observed from the Quiver plots as shown in the Figure 2.19(i) that at lower biases the current is localized to the p-i-p shunt region while as seen in Figure 2.19(ii) the p-i-n diode current becomes uniform across the bulk device at higher forward biases [16].

The formation of pre-existing shunts which are intrinsic to the cell is attributed to diffusion of aluminum from AZO into the n-type a-Si:H layer counter-doping it to p-type [19]. A small incursion of aluminum near the AZO grain boundaries or regions of high a-Si:H void density can create a p-i-p shunt path since the n-type layer is of small thickness (about 20 nm) [16]. This phenomena affect the cell stability as aluminum can diffuse at low temperatures range of about 200-300°C [19]. Therefore, the sputtering process for processing the top contact can diffuse aluminum to sufficient depths (>20nm) destroying the n-i junction forming parasitic shunts. One possible solution to this diffusion of Al as suggested in literature is to introduce a barrier layer to prevent diffusion, although, the extra series resistance needs to be accounted which might be caused by the diffusion barrier.

### C. Statistics of shunt formation

Dongaonkar et al analyzed the large spread in the shunt-current magnitude to understand the distribution of shunts on the cell surface [16]. After a series of plotting cumulative distribution function (CDF) for cells of various i-layer thickness against the shunt current, it was concluded that the largest shunt meaning the lowest resistance path offered dominates the total shunt current generated in a cell. Furthermore, the second largest shunt in the cell was found to be 1-2 order magnitude smaller than the largest one [16]. These observations suggest that only a small amount of large shunt dominate the total shunt loss. It is these shunts that need to be removed to improve the cell performance.

### 2.3.3 Metastable shunt busting

For large area thin film solar cells to become commercially feasible, shunt removal during processing or post processing is necessary. Removing shunt while processing requires equipment and processes which tend to increase the cost of solar cells. Hence, a method was developed by Nostrand et al in 1979 to burn out the shunts by application of reverse bias which is less than the breakdown voltage of the cell [20]. However, in the recent literature it is has been understood that threshold switching of shunts using the reverse bias is metastable in nature i.e. $I_{sh}$ can decrease or increase on application of reverse bias [16].

The metastability of the diode in the literature has been understood using reverse voltage (OFF transition) and current sweep (ON transition) [16]. It was observed that during the reverse voltage sweep the $I_{sh}$ would decrease by a magnitude of 1-2 orders while $I_{sh}$ would increase and stay higher after a reverse current sweep. The following sections discusses the shunt formation physics responsible for metastability.

#### A. ON transition

It was observed that ON transition is a voltage driven process [16] meaning an increase in $I_{sh}$ is triggered at the threshold voltage ($V_{critical}$). For the p-i-p structure it means the positively charged Al ions under the influence of the electric field migrate into the a-Si:H layer. As seen in Section 2.3.2 that a small incursion at depths of around 20 nm is sufficient to form p-i-p shunt path. Hence, it is suggested that due to Al migration from AZO top contact layer the ON transition occurs.

#### B. OFF transition

The OFF transition as reported in literature occurs due to power threshold and not to voltage threshold [16]. This suggests that OFF transition could occur because of local heating which could lead to dissolution of the migrated Al filament. As already discussed in Section 2.3.2 the largest shunt path carries the most current, a high temperature due to local heating could disperse off the shunt caused by the Al migration hence resulting in decrease in $I_{sh}$ [16].

### 2.3.4 Effect of annealing

The instability problem of a-Si:H materials has been detrimental in growth of the thin film technology. The instabilities caused due to thermal and light induced changes are said to create degradation in solar cell efficiency over the lifetime [19]. According to M.Haque et al the Staebler-Wronski effect which is light induced degradation is reversible in nature. It is through annealing of cells at temperature above 150°C the solar cell efficiency can be restored [19]. However, annealing cannot restore the efficiencies to the original values. This reduction in efficiency is due to reduction in the shunt resistance, suggesting the presence of an irreversible degradation mechanism occurring in parallel with light induced degradation.

M.Haque et al have suggested that due to random network present in a-Si:H, it becomes easier for a-Si to interact with other materials. The degradation of solar cell performance parameters (such as $\eta$, FF, $V_{oc}$) was observed in the range of 100-300°C in literature. For 150°C and higher temperatures a significant reduction in shunt resistance was observed. This reduction in shunt resistance can be attributed to the interaction of Al with the n-layer in the p-i-n layer as seen in Section 2.3.2. For the cells annealed at temperatures of 180°C, shunt resistance reduced by a factor of 50. The cells annealed at

200°C and above degraded beyond the point of recovery due to the a-Si:H/Al degradation. Furthermore, the results of Raman analysis indicated that microcrystalline silicon was present at sites where a-Si and Al were in contact with each other during annealing [19].

## 2.4 Series resistance

The series resistance is a parasitic loss which dissipates power factor of a solar device. The series resistance affect the current voltage parameters of the solar cell, which influences the maximum achievable power output of a solar cell. Series resistance can provide useful information as a feedback to control the production process while improving the cell performance [21]. In a 1D representation of a solar cell as shown in Section 2.2.5 the series resistance can have components in both vertical and horizontal direction namely, the TCO sheet resistance and the stack resistance. Apart from these two contributions there is additional laser interconnection resistance which can degrade the performance of the solar cell. Ideally all the contributions of series resistance should be as low to improve the current voltage characteristics of the solar cell as suggested in Figure 2.14. As shown in Figure 2.13 the series resistance can be represented by adding an additional resistor in series. The following section discusses the various factors that affect the series resistance in a solar cell.

### 2.4.1 Stack resistance

The resistances in the stack that can result in losses in the solar cell. Each layer has some resistance to the flow of the current. It is a type of intrinsic resistance offered by a stacked layer against the local current flow. The stack resistance can be of different types like resistance offered by the p-layer, contact resistances between metal and semiconductor layers or contact resistance between p-layer and the TCO. Since, it is an intrinsic parameter of the solar cell the quantification of the stack resistance becomes difficult and hence, it is not discussed further.

### 2.4.2 Sheet resistance

The solar cell in its stack consists of layers of Transparent Conductive Oxides (TCO) which can contribute to sheet resistance of the solar cell. The TCO in the front contact can cause a voltage drop across the width of the solar cell. The TCO's in general have higher resistance than that of good metals, increasing the resistance in the solar cells [22]. In the Figure 2.20 a thin film of thickness t, length l and width b is depicted. The $\rho$ is the resistivity which is roughly inversely proportional to the concentration of free charge carriers (n) [23] as shown in Eq 2.9. Here, q is the unit charge while $\mu$ is the mobility. The sheet resistance ($R_{sq}$) of a square conductive sheet depends only on the thickness of the sheet. The relation between sheet resistance and resistivity of the layer is shown in Eq 2.10 [23]. The unit for sheet resistance is ohms per square (Ω/□).

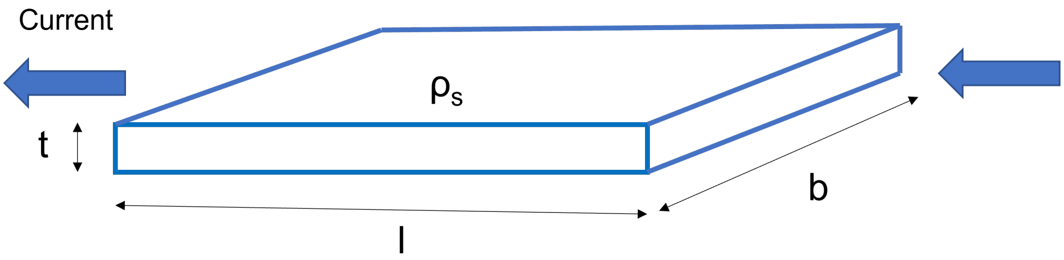

Figure 2.20: Schematic diagram illustrating the concept of sheet resistance and the parameters affecting it [Retrieved from HyET Solar]

$$\rho_s = \frac{1}{q \times \mu \times n} \tag{2.9}$$

$$R_{\mathrm{sq}} = \frac{\rho}{t} \tag{2.10}$$

To understand the effect of sheet resistance on series resistance a model was developed for the cases of discrete and continuous distributions of sheet resistance. The Figure 2.21 illustrates a cross-section of n-p junction solar cell where $\rho_s$ is the continuous TCO sheet resistance, $\rho$ is the bulk semi-conductor resistivity, while R is the discrete TCO resistance and r is the discrete semiconductor resistance. Based on these parameters, a relation for the sheet resistance and series resistance was developed [24].

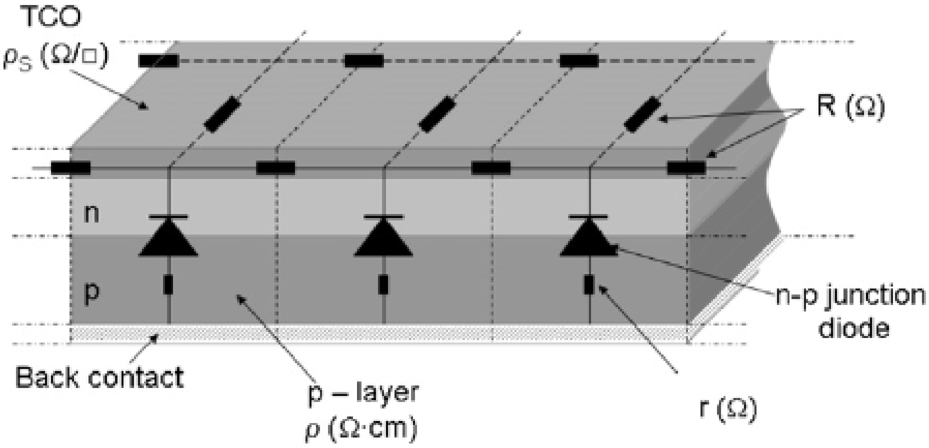

Figure 2.21: Cross section of a n-p junction solar cell [24]

$$R_S \cong \frac{\rho_S L^2}{2} \tag{2.11}$$

The Eq 2.11 gives the empirical relation between the sheet resistance and the series resistance of the solar cell. Here, it can be seen that the series resistance is directly proportional to the sheet resistance. The sheet resistance affects the fill factor (FF) while leaving the open-circuit voltage ($V_{oc}$) and the short-circuit current density ($J_{sc}$) unchanged [24]. Hence, it becomes important to optimize the sheet resistance to improve the collection of electron-hole pairs across the solar cell and improving the performance of the solar cell.

### 2.4.3 Laser interconnection resistance

The laser interconnection process ensures separation of cells. It breaks boundary of one cell from another while providing a route for the current to flow through the solar cell. The laser interconnection has influence on the series resistance which affects the JV curve. However, as discussed by E. Hamers et al the influence of laser interconnection resistance is not as straightforward and is explained using the Figure 2.22. The figure shows the cross-section of solar cell with the laser scribing process. Here, different laser scribes like P1, P2 and P3 are used to define the solar cell area. Finally, the bus bar scribes are used to collect the current from the module.

The various contributions to the interconnect resistance are as follows:

- **TCO resistance** - The TCO strip from the P1 scribe to the end of P2 scribe forms a part of interconnect resistance.

- **Pin scribe** - The contact resistance of the back contact with the TCO in the pin scribe forms the pin scribe resistance. The area of contact between the back contact and the TCO describes the resistance offered between the interfaces.

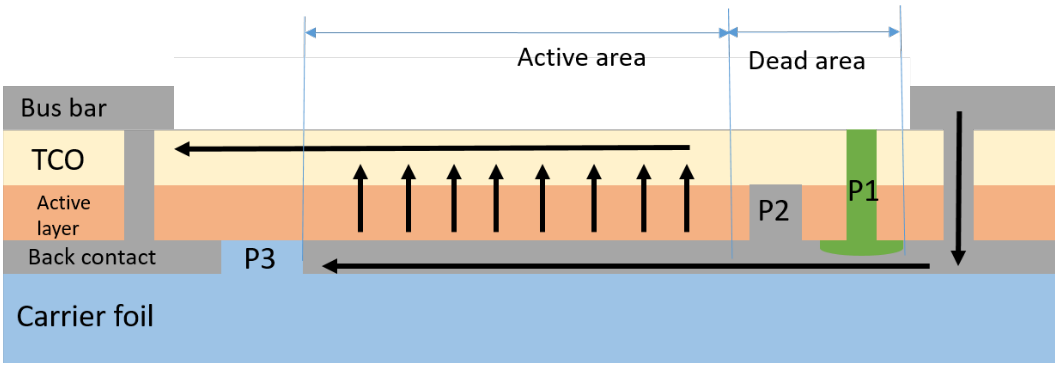

Figure 2.22: Cross section of a solar cell under illumination, for a forward bias below Voc [Retrieved from HyET Solar]

- **Back contact resistance** - The back contact resistance from the start of the active region to the adjacent cell offers a resistance component. However, since the back contact offers a very low sheet resistance of 0.1 Ω/□, its contribution can be neglected.

To conclude, the series resistance of a solar cell should be as low as possible. A high series resistance affects the JV curve around the Voc, hence decreasing the maximum power output from the solar cell. The contribution of series resistance to a solar cell can be controlled, however, there are always some intrinsic contributions to the series resistance like the stack resistance. The other two components to the series resistance are sheet and laser interconnection resistance. These contributions need to be optimized to get the best performing solar cell.

# Chapter 3

# Experimental details: device fabrication and characterisation

The fabrication process, as discussed in Section 1.3 briefly discussed about the manufacturing process of HyET Solar. This chapter will focus on the different manufacturing and deposition techniques for the various layers deposited across the manufacturing process. Furthermore, the lab-scale fabrication route is also discussed to understand better the characterization route. Finally, the different characterization techniques used in this work are discussed.

## 3.1 Deposition mechanisms

The explosive growth of the semiconductor industry has led to the development of various vapour deposition mechanisms for different types of materials, including fibres, thin films and multilayer coatings. Amorphous and nanocrystalline alloys have been produced as thin films due to the vapour deposition mechanisms in thickness ranges from micrometres to nanometers [25]. The thin film deposition techniques are classified on the nature of deposition as shown in Figure 3.1. The deposition nature is based on the physical or chemical process involved [26]. The chemical processes include gas-phase and solution-based deposition methods, namely, chemical vapour deposition (CVD) and solution-based chemistry (SBC). Physical vapour deposition (PVD), which involves physical vapour, is the third type of vapour deposition technique. The CVD process deposition occurs by chemical reaction, while PVD deposition is due to condensation. PVD process is exothermic while CVD is endothermic [27].

Among the various deposition mechanisms discussed in Figure 3.1 the CVD and PVD mechanisms are currently employed in the fabrication of thin-film flexible solar cells at HyET Solar. Hence, this report will further discuss the CVD and the PVD mechanisms. The PVD mechanism based on the way of generating the vapour flux comprises Thermal evaporation, Sputtering, Laser-based deposition and Molecular beam epitaxy techniques, as shown in Figure 3.1. While the CVD mechanisms based on the application of the pressure consists of Atmospheric pressure CVD (APCVD), Plasma enhanced CVD (PECVD) and Low-pressure CVD (LPCVD).

### 3.1.1 Physical Vapour Deposition (PVD)

PVD is a vaporization coating technique that can deposit the metal vapour at the atomic level. The process is carried out under high vacuum conditions (10-6 torr) in a vacuum chamber. The process of PVD can be described in the following sequence of steps : (1) the material vapour is formed using a physical mechanism like a high-temperature vacuum or gaseous plasma, (2) the vapour needs to be transported to a region of low pressure from its source to the substrate, (3) finally, the vapour can undergo condensation to form the desired thin film on the substrate [28]. In general, the PVD process can be divided into two groups: evaporation and sputtering [29]. The evaporation mechanism involves the deposition of the thin film using thermal means, while the sputtering mechanism is based on the atoms to be dislodged from the solid target through the impact of gaseous ions or plasma. Generally, the sputtered atoms have higher energy than evaporated atoms resulting in better adhesion properties, superior mass densities and crystalline structures with columnar growth.

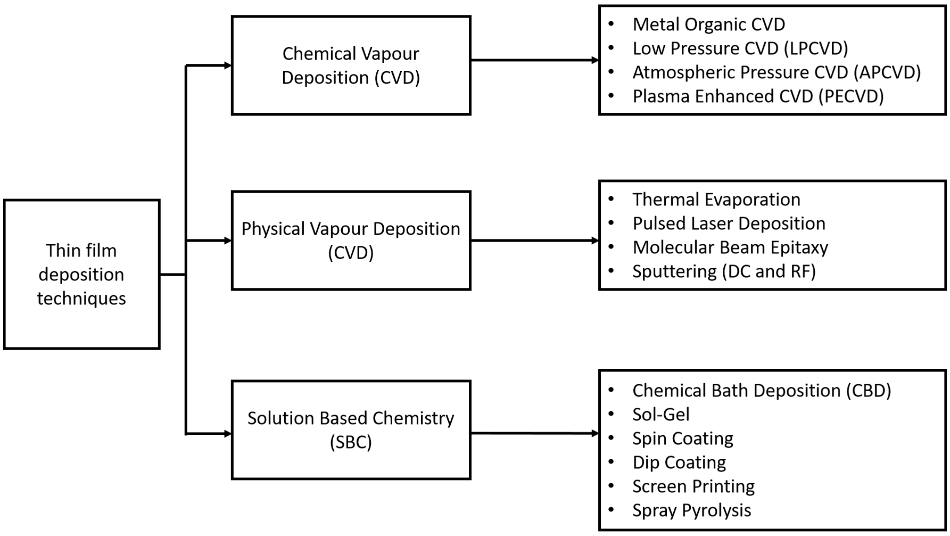

Figure 3.1: Classification of thin film deposition methods [26]

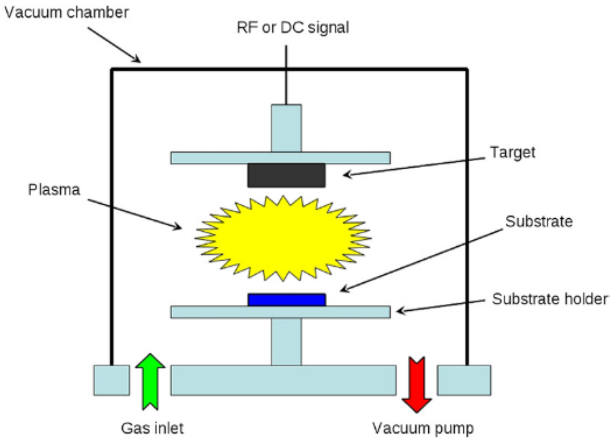

Figure 3.2: Simple schematic diagram of the sputtering a type of PVD mechanism [30]

The sputtering mechanism as a type of PVD at HyET Solar is used as the deposition technique for the back contact and the buffer layer in the front contact of the solar cell. The sputtering mechanism, as discussed in the previous sections, requires high vacuum and plasma to enhance the growth of the desired film. The major components involved in the sputtering tool as shown in Figure 3.2 are the target which is made of the metal that needs to be deposited, the substrate on which the target metal needs to be sputtered, gaseous ions, a neutral gas like Ar to bombard the target for dislodging the target atoms and a power generator to ignite the plasma. The secondary electrons emitted from the target surface as a result of the ion bombardment play a vital role in keeping the plasma ignited [30].

Based on the material of the film that needs to be sputtered, there are three types of sputtering, namely, DC Sputtering, RF Sputtering and magnetron-assisted sputtering. The significant difference between the RF sputtering and DC sputtering is based on the type of generator used for igniting the plasma [30]. The simplest of them all is DC sputtering, which requires a cathode, an anode, DC power supply and a sputtering gas in a vacuum chamber. A large target can be used for this process which can result in an improved thickness homogeneity of the deposited film [30]. However, not all the materials can be deposited using a DC sputtering mechanism; hence, for electrically insulating materials like polymers or oxides, RF sputtering is used. Magnetron sputtering is another mechanism that uses a magnetic field to increase the plasma and current density at the cathode. As shown in Figure 3.3 we use different materials in a traditional single-junction stack manufactured at HyET Solar; the following section will discuss both RF sputtering and DC sputtering used.

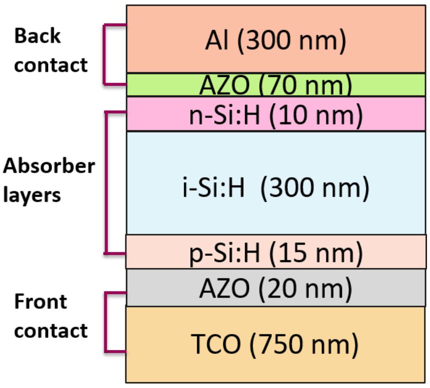

Figure 3.3: Schematic diagram of the different layers in a single junction solar cell manufactured at HyET Solar

### RF Sputtering

As discussed previously, the oxides layer and polymers require RF sputtering. Hence, to deposit the TCO back contact layer in lab scale samples, RF sputtering is required. Figure 3.3 shows the schematic diagram for the different layers in a typical single-junction solar cell made at HyET Solar. The 70 nm AZO (Aluminum doped zinc oxide) layer, a TCO, needs to be deposited using the RF sputtering mechanism. For a TCO material, the charge build-up on the target can prevent the dislodging of atoms from the target. Hence, a radio frequency (RF) power supply helps in a half periodic cycle of acceleration of positively charged ions towards the target surface with enough energy to cause deposition of the film on the substrate. While in the other half cycle, the atoms reach the surface of the target to prevent the charge build-up, which inhibits the sputtering process. With this periodic half cycle of power supply, we can generate the required plasma for sputtering.

The typical RF sputtering tool in a schematic diagram is shown in Figure 3.4. Here the different components, as discussed previously, are shown. The vacuum chamber is kept at low vacuums of around $<10^{-5}$ Pa. The size of targets is around 314 $cm^2$. The targets are provided with cooling water to ensure proper temperature conditions for the targets. The RF power supplied for standard baseline conditions is 407 W, creating a power density of 1.3 W/ $cm^2$. The typical frequency used for RF sputtering is around 13.56 MHz. A shutter is placed between the targets and substrate to create a condition of pre-sputter to ensure the plasma is ignited before the actual sputtering process. The Argon gas is fed in before the plasma is ignited to ensure that the targets are bombarded with high energy ions at the right pressure conditions. Furthermore, as discussed before, magnets are also provided in the targets to assist with a better deposition process. In the tool at HyET Solar, the substrate temperature cannot be controlled, hence to optimize the sputtering mechanism, the power and the chamber pressure based on the flow rate of the Argon gas are the only parameters that can be optimized.

### DC Sputtering

The DC sputtering, as shown in Figure 3.3 is used for sputtering 300 nm of Aluminum in the back contact. The working principle is similar to that of the RF sputtering; however, the parameters are changed. The power generator used here is DC-based since metal layers do not have the problem of charge accumulation on the target. Furthermore, the power used is around 1380 W, with the same target size as that of AZO. The flow rates for argon gas flow for the DC sputtering is lower than that of the RF sputtering. The pre-sputtering and sputtering times are lower as well based on the fact that DC sputtering is more straightforward than RF sputtering. Magnetron assisted sputtering is also present

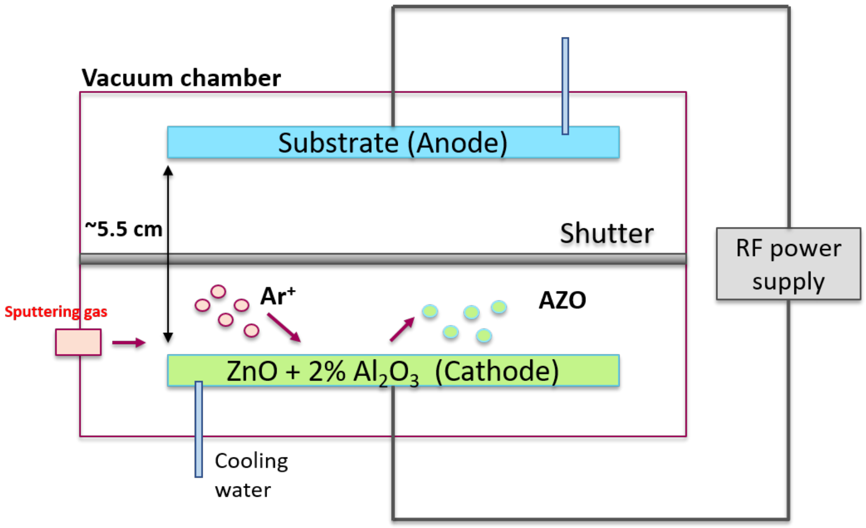

Figure 3.4: Schematic diagram of the sputtering tool at HyET Solar for RF sputtering

for DC sputtering in the HyET tool.

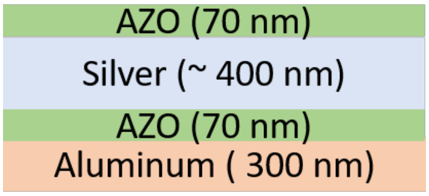

Figure 3.5: Schematic diagram of the back contact based on silver (Ag) with the top AZO in contact with silicon

Apart from the traditional back contact layers as shown in Figure 3.3 another stack of back contact based on DC sputtering was developed for the triple-junction solar cells based on amorphous silicon /microcrystalline silicon/ microcrystalline silicon stack. Figure 3.5 shows the silver-based back contact that can be sputtered using the same DC sputtering and RF sputtering tool available at HyET Solar. Here, a thicker Ag-based reflector helps to improve the reflection back into the cell, improving the current generation. This structure was used to process a batch of triple junctions, which results will be discussed further in this report.

The configuration of the DC sputtering for silver back contact was similar to that of the aluminium-based back contact. Here a DC power of 1400 W was used for the same sputtering as that of aluminium. An AZO layer is provided between the silver and aluminium back contact to prevent the diffusion of aluminium into the silver. The additional aluminium layer with 300 nm of thickness is sputtered to ensure adhesion to the carrier foil.

### 3.1.2 ZnO:Al films prepared by sputtering deposition

As already discussed in section 1.4 one of the objectives of this work is to improve the performance of the lab samples produced at HyET Solar, hence a literature study on ZnO:Al as back contact deposited by sputtering was done to understand the various factors affecting the film growth during the sputtering process. This section will briefly discuss the effect of various parameters on the optical, electrical and structural properties of the ZnO:Al sputtered film, which will be used as a reference for optimising the sputtering process at HyET Solar.

### Structural properties

Thornton model has been developed to understand the effect of substrate temperature and sputter pressure on the growth of sputtered metal films. However, since there are some fundamental differences between metals and TCO, a modified Thornton model has been proposed by Kluth et al [31]. To make the model applicable for ZnO:Al films on glass substrates, the normalised temperature, which is the ratio substrate temperature (T$_s$) and the melting temperature (T$_m$) is omitted. This is because the melting point of ZnO is very high (1975 °C), making the normalised value very small. Hence, in the modified Thornton model, the substrate temperature is considered instead of the normalised temperature value as shown in Figure 3.6. Another modification from the original Thornton model is the absence of Zone 3 (recrystallisation zone) which appears at very high substrate temperatures. Apart from these changes, the general statement of the Thornton model is maintained, which suggest that reducing the sputtering pressure and increasing the substrate temperature leads to a more compact and dense film.

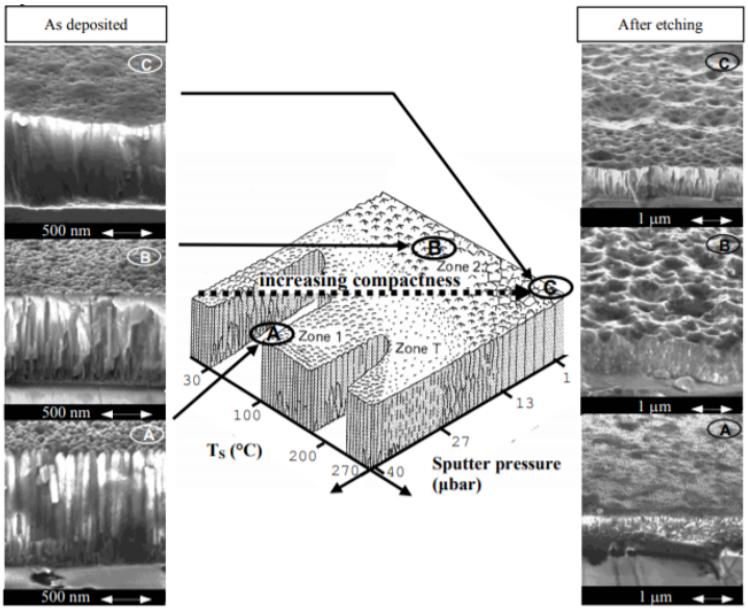

Figure 3.6: Modified Thornton model describing the correlation between sputtering parameters, structural properties and etching behavior of RF sputtered ZnO:Al films on glass substrate [31]

The variations in the surface structure for the ZnO:Al films were demonstrated using three different conditions as shown in Figure 3.6. Here, it can be seen at Sample A that the film compactness is very low due to the deposition conditions. However, we see an improved dense film structure in Sample B and further improvement for Sample C, suggesting a lower sputter pressure and higher substrate temperature provides the ideal growth of the ZnO:Al film. This improvement in compactness of the film helps to improve the electrical properties reflected in hall effect mobility as there are fewer structural defects [31]. Furthermore, on etching, it was observed that the Zone 1 films provide an anisotropic etching process, which produces a crater-like structure, hence, providing small features and affecting the electrical properties. For Zone 2, films with high conductivity and large surface features were observed, suggesting the desired characteristics of the sputtered film. Therefore, this work will focus on optimizing the ZnO:Al film in the back reflector in the HyET stack based on the modified Thornton model.

Furthermore, the effect of sputter pressure and RF power on the crystallite size and the lattice stress is understood. The lattice stress can be introduced in the film in two ways; namely, intrinsic, which is during deposition and caused due to microstructure of the thin film and extrinsic, which can be caused due to post-deposition processes [32]. In Figure 3.7 we can see the effect of chamber pressure increases is not significant to affect the crystallite size. The lattice stress was low for the films deposited with 0.1 Pa; however, the stress was increased for films with sputter pressure greater than 0.2 Pa. For the RF power, the effect on the crystallite size was insignificant, as seen from the Figure 3.8; however, high lattice stress was observed at lower RF power following an inverse relation with the power.

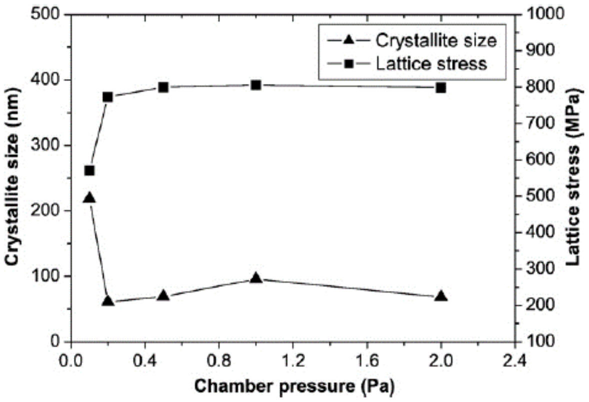

Figure 3.7: Effect of the chamber pressure on the crystallite sizes and lattice stresses of the ZnO:Al films [33]

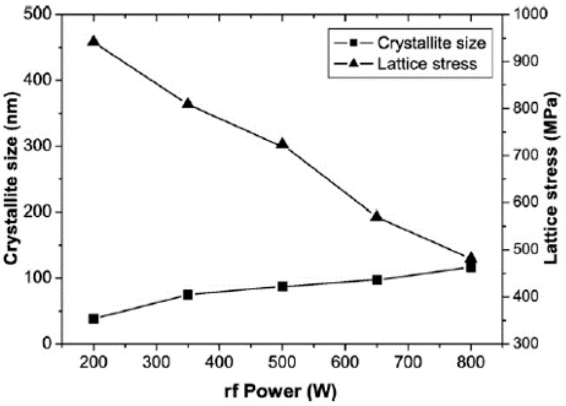

Figure 3.8: Effect of the RF power on the crystallite sizes and lattice stresses of the ZnO:Al films [33]

## Optical properties

The optical properties for the AZO film based on different sputter pressure are shown in Figure 3.9. The average optical transmittance was calculated to be 84% in the visible region for the films sputtered with 1.0 and 3.2 Pa of the sputtering pressure. However, the transmittance dropped for lower pressure to about 83%. Furthermore, the films with pressure lower than 0.2 Pa was opaque to near-infrared light. Moreover, the bandgap for ZnO film is around 3.28-3.30 ev; however, for the film deposited with 0.2 Pa, the bandgap was higher than that of the films deposited at 1.0 and 3.2 Pa. This trend was attributed to the Burstein-Moss effect in literature [34]. Burstein-Moss effect is caused when there is an increase in absorption when doping concentration is increased. In this case, at lower sputter pressure, the effect is caused due to increased free electron concentration due to Al doping [34].

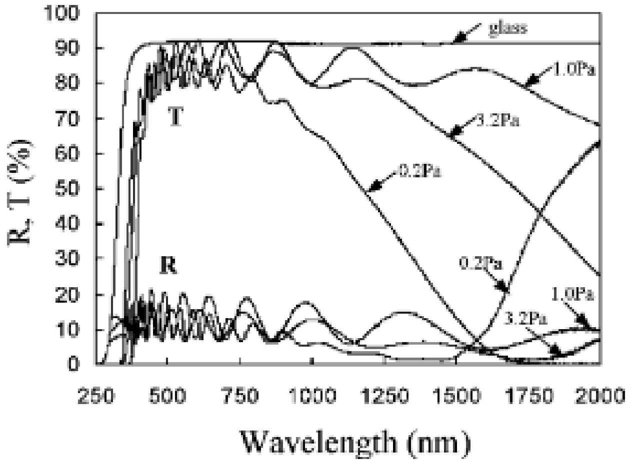

Figure 3.9: Optical transmission (T) and reflection (R) spectra of ZnO:Al film. The films with approx 1$\mu$m thickness were grown at substrate temperature of 2508C, rf power of 100 W and $P_{Ar}$ = 0.2,1.0 and 3.2 Pa, respectively [34]

## Electrical properties

The electrical properties are majorly affected by the substrate temperature. It has been seen in literature that increasing the substrate temperature results in decreases in film resistivity [34]. This corresponds to an increase in carrier concentration and mobility as they follow an inverse relation to resistivity.

However, since the substrate temperature in the HyET Solar tool cannot be changed, substrate temperature's effect on the electrical properties is not discussed further. Although, the effect of sputter pressure and RF power on the electrical properties will be discussed in the results of this work.

### Application in solar cells

As seen from the previous sections, the sputtering pressure and substrate temperature play a vital role in determining the JV characteristics of a solar cell; however, a particular s-shape curve was found in the solar cells with the ZnO:Al back reflector sputtered. As seen in Figure 3.10 the s-shape curve is evident for the cells sputtered at lower sputter pressure of 0.1 Pa. For the cells without the ZnO:Al back reflector, the JV performance improved, while for the sputtering at higher sputter pressure of 25$\mu$bar the JV characteristics even improved as seen in the Figure 3.10. Hence, Advance Semiconductor Analysis (ASA) software stimulated the effect of low sputter pressure on the solar cell with a defective interlayer in the back reflector. Further information about the ASA can be found in Section 3.4.4. It is evident from the figure that the stimulated curve follows a s-shape trend similar to that of a curve with low sputter pressure [35].

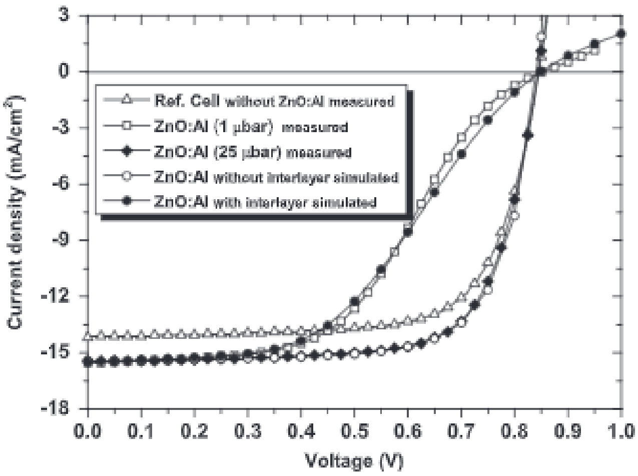

Figure 3.10: Experimental and stimulated JV characteristics of a-Si:H solar cells with and without the ZnO:Al back reflector [35]

Furthermore, it was observed that the possible s-shape curve in the JV curve is due to the creation of a barrier that can prevent the collection of electrons at the back contact. This barrier can be created due to a highly defective layer at the n-a-Si:H/ZnO:Al interface, which can be generated when high energy ZnO:Al ions are sputtered at low chamber pressure (0.1Pa), causing the bombardment of the n-type a-Si:H and creating defects [35]. To conclude, the chamber pressure is one of the most critical parameters that need to be optimized for sputtering the best optical, electrical and morphological ZnO:Al as a back reflector for thin-film a-Si:H based solar cells.

## 3.1.3 Chemical Vapour Deposition (CVD)

The CVD process is one of the most powerful tools for producing semiconductors, including silicon and metal oxides. It works on the principle of dissolution of chemical reactions between gaseous reactants when subjected to plasma or heat [36]. Based on different activation sources, the different types of CVD techniques are described in Figure 3.1. The sequence of steps occurring in the CVD mechanism can be described in the following sequences: (1) transportation of the reactant gases molecules to the surface of the substrate, (2) adsorption of the species on the substrate surface, (3) heterogeneous surface reaction catalyzed by the surface of the substrate, (4) diffusion of the reactant species on the surface of the growth sites, (5) nucleation and the growth of the film on the substrate, and (6) desorption of the gaseous products and transport of the reaction products away from the surface [30]. The main CVD parameters that need to be controlled for an optimized performance are temperature, pressure, total gas flow, and reactant gas concentration.

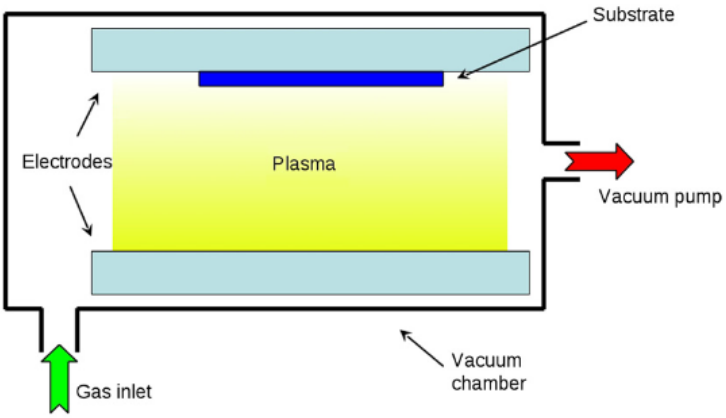

Figure 3.11: Simple schematic diagram of the CVD mechanism [30]

Based on the concept of utilizing the reaction of gaseous precursors to form a solid coating on a heated substrate, CVD main components involve a reaction chamber where the substrate can be heated to the desired temperature for the deposition process. Figure 3.11 shows a simple schematic diagram of the reaction chamber used in the CVD mechanism. The gases required for the coating are fed through the gas inlet under specific pressure conditions to ensure that the gases do not react before reaching the substrate. The vacuum pump removes the waste gases from the reaction chamber. The advantage of CVD is the ability to produce highly pure and dense films at high deposition rates with the ability to coat complex shapes [30]. In literature, as shown in Figure 3.1 many types of CVD mechanisms are possible based on the pressure conditions like Atmospheric pressure CVD (APCVD) or Low-pressure CVD (LPCVD). Depending on the application of plasma, there can be plasma-assisted CVD, Plasma enhanced CVD (PECVD). The plasma enhanced CVD offers a distinct advantage over other thermally activated CVD due to its low-temperature deposition conditions.

The CVD mechanism is used for the deposition of various layers in the HyET solar stack. The TCO in the front contact, which is $SnO_2$:F, is deposited using APCVD, while the absorber layers based on amorphous silicon and microcrystalline silicon are deposited using the PECVD tool. This report focuses on optimizing the deposition conditions of absorber layers; hence, PECVD will be discussed further in detail.

### Plasma enhanced CVD (PECVD)

PECVD is a hybrid coating process where the energized electrons are used to enhance the deposition instead of the thermal energy with the other conventional CVD techniques. It requires a vacuum at a pressure range of <0.1 Torr with low substrate temperatures of around 150 °C. RF-PECVD (radio frequency plasma-enhanced chemical vapour deposition) uses reactant gases in between a grounded electrode (anode) and a RF-energized electrode (cathode) as shown in Figure 3.12. The matchbox helps to develop the power in the RF electrode, while the capacitive coupling between the two electrodes helps to excite the reactant gases into plasma which undergoes a chemical reaction to deposit the desired coating [37]. The RF signal used for the oscillating electrical field between the two conductive electrodes is 13.56 MHz, while for a very High-Frequency Plasma Enhanced CVD (VHF PECVD) it is in the range of 50-80 MHz [12].

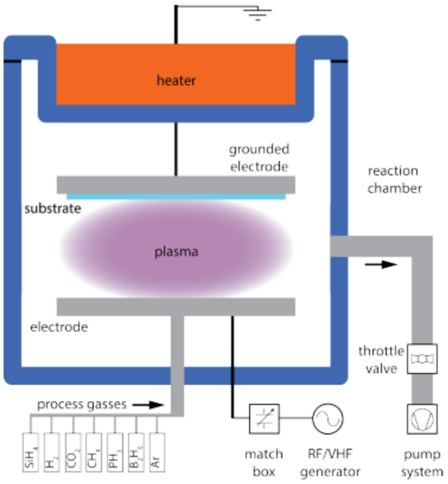

Figure 3.12: Simple schematic diagram of the RF PECVD tool [38]

The RF signal generated provides the energy for the decomposition of the gas which bears the silicon. Silane ($SiH_4$) is used as the silicon bearing gas for deposition of the a-Si:H and nc-Si:H layers. This decomposition of the silane helps to ignite the plasma inside the chamber. The radicals from the decomposition of the silane diffuse to the growing film and undergo surface reactions. In the process of decomposition, the electrons under the influence of an electric field are accelerated and dissociate the gas molecules into atoms and molecules, both positive and negative ions and electrons. The electrons owing to their lower mass, get driven towards the electrodes of the reactor much easier than the other ions. This creates a net electric field between the centre of the plasma and the grounded substrate. Sheaths are known to be the region between the electrodes and the bulk of the plasma. It is the region in which the electric field is present. The positive ions cause ion bombardment on the electrodes while the negative ions are trapped in the centre and eventually released as dust. On the substrate, the silicon relaxation takes place while the hydrogen molecules are released [39].

The best radical for the growth of a-Si:H and nc-Si:H film is considered to be $SiH_4$. Higher silane radicals like ($Si_2H_5$,$Si_3H_8$), low lifetime radicals and reactive radicals ($SiH_2$, SiH) require higher deposition power. The deposition rate increases with a higher power; however, the dust formation is associated with higher deposition powers. Hence, the general approach for nc-Si:H's growth involves using silane-hydrogen mixtures as a source gas under certain pressure, temperature, and power conditions. To get the doped layers like p and n-type suitable gases like boron-yielding gas (e.g. $B_2H_6$) and phosphorus-yielding gas (e.g. $PH_3$) are used respectively [40].

The main properties that can affect the properties of the nc-Si:H, like crystallinity, grain size and defect density, are shown in Figure 3.13. These factors in turn determine the solar cell performance [40].

- Dilution ratio ($S_c$) : The ratio of the flow rate of silane to the sum of flow rate of hydrogen and silane is the dilution rate as shown in Eq 3.1.

  $$S_c(\%) = \frac{\mathrm{Q_{SiH4}}}{\mathrm{Q_{SiH4}} + \mathrm{Q_{H2}}} \cdot 100\% \tag{3.1}$$

  Increasing the dilution ratio decreases the crystallinity into the amorphous phase due to availability of less hydrogen to make nanocrystalline material.

- Deposition power : Increasing the deposition power provides higher deposition rates, however, due to more energy being imparted to the ions the film quality is affected as the defect quantity increases.

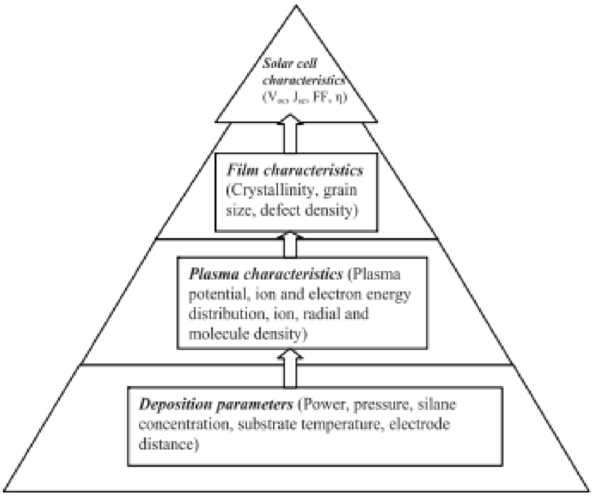

Figure 3.13: Correlation between deposition parameters and the solar cell characteristics [40]

- Deposition pressure : Increasing the pressure reduces the ion energy and hence the ion bombardment on the film is reduced, thus improving the material quality. High pressure also leads to higher growth rates.
- Substrate temperature : Heating of the substrate influences the diffusion growth on the surface. Hence, ideally moderate temperatures provide better material depositions.

### Growth of a-Si:H

The deposition process for a-Si:H consists of three stages, the reactive species being created in the plasma, the reaction of the species on the film surface and the conversion of the surface layers into a-Si:H. The main growth radical for a-Si:H is $SiH_3$ [41]. The $SiH_3$ radicals are physisorbed on H-saturated a-Si:H surface. The radical then hops to the neighbouring Si-H leaving a surface dangling bond (DB) as seen in Figure 3.14. Additionally, instead of forming a DB, the incoming radical can add to a existing surface of DB contributing to the Si-Si growth.

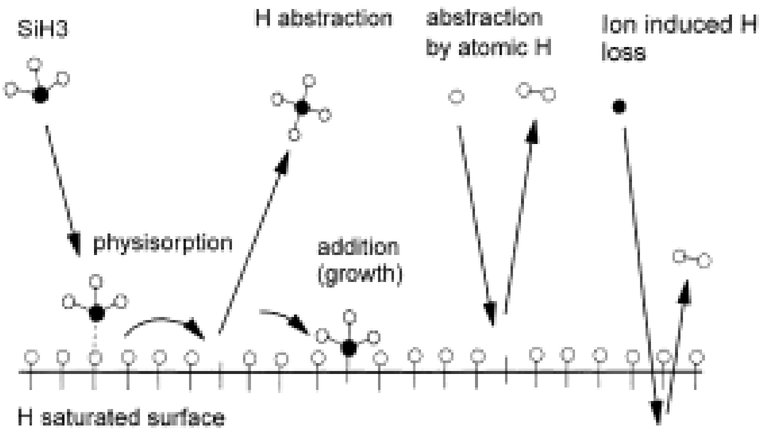

Figure 3.14: Schematic process of $SiH_3$ radicals on a-Si:H surfaces [41]

### Growth of nc-Si:H

Matsuda suggested three models to explain the growth of nc-Si:H, namely, Surface diffusion model, etching model and chemical annealing model. The validation of surface diffusion model is done experimentally. Hence this report discusses briefly the surface diffusion model for the growth of nc-Si:H layers.

Figure 3.15 represents the detailed representation of the surface diffused model. Here, as suggested a sufficient flux density of atomic hydrogen realizes a full coverage of the surface by bonded hydrogen. It also produces local heating due to hydrogen recombination reactions growing on the surface [42]. These events enhance the surface diffusion length of the precursor gases. This leads to film precursors adsorbed on the surface to find energetically favourable sites leading to formation of flat atomic surface. The first growth is the nucleus of $\mu$c-Si, after the nucleus growth the epitaxial crystal growth takes place [42].

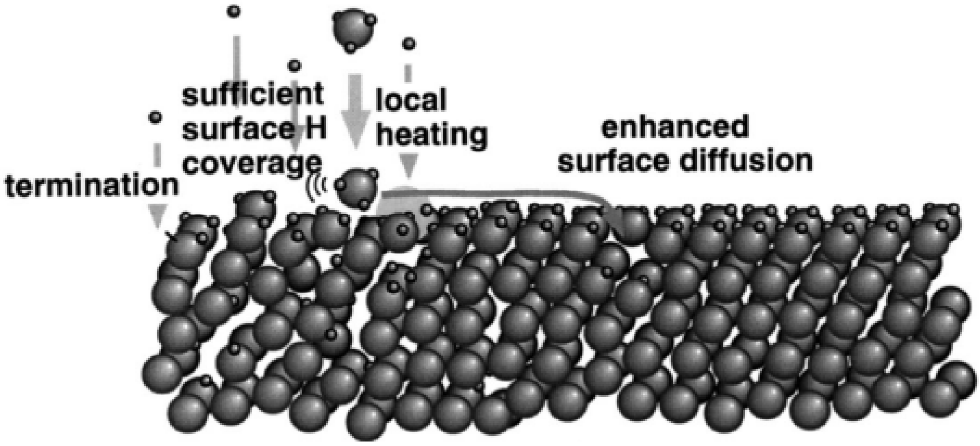

Figure 3.15: Surface diffusion model for $\mu$c-Si:H formation [42]

### PECVD tool at HyET Solar

The PECVD tool at HyET Solar consists of various zones where the intrinsic and doped layers can be deposited. Since it is R2R equipment, various zones deposit various layers depending on the doping and varying process conditions. A roll of aluminium foil/TCO is passed under different zone for the deposition process to occur, as shown in Figure 3.16. Each Z1-Z8 in the figure represents a different zone where intrinsic and doped layers are deposited.

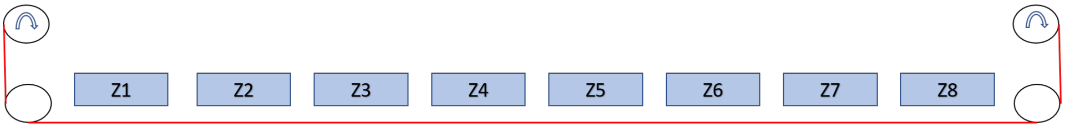

Figure 3.16: Simple schematic diagram of the PECVD tool at HyET Solar (Reproduced from HyET Solar documentation) In blue different zones are shown, in red the roll direction is depicted

Table 3.1 shows the flow rates for various zones. Zone 2 is used to deposit the p-type a-Si:H layer, where Zone 1 is used for flushing the foil with $H_2$. After Zone 1, the roll moves to Zone 2, where the p-a-Si:C is deposited by doping the silane ($SiH_4$) with diborane ($B_2H_6$) and methane ($CH_4$) to develop the amorphous silicon carbide film. Consequently, once the p-layers are deposited, the roll moves from Zone 3 to Zone 7, where the intrinsic layers are deposited with very high dilution ratios to get amorphous material. Five zones are used to deposit the intrinsic i-layers to develop a columnar growth of the amorphous layers. Finally, in the last Zone, n doped layers are deposited to complete the p-i-n junction. Here, lower silane flows with phosphine ($PH_3$) and carbon dioxide ($CO_2$) are used to form the n-a-Si:H layer. The phosphine flow rate is a very sensitive quantity as too low of the flow rate can increase the series resistance of the solar cell and cause a S-shaped curve in the IV characteristics of the solar cell, affecting the performance.

Depending on the type of cell depositions the number passes in the PECVD tool can be adjusted. For a single junction device only pass through the solar cell needs to be done. However, for a tandem

| | ***Layer*** | ***Precursor gases*** |
|---|---|---|
| ***Zone 1*** | p-a-Si:C | $SiH_4$ , $H_2$ |
| ***Zone 2*** | p-a-Si:C | $SiH_4$ , $H_2$ , $CH_4$ , $B_2H_6$ |
| ***Zone 3*** | a-Si:H | $SiH_4$ , $H_2$ |
| ***Zone 4*** | a-Si:H | $SiH_4$ , $H_2$ |
| ***Zone 5*** | a-Si:H | $SiH_4$ , $H_2$ |
| ***Zone 6*** | a-Si:H | $SiH_4$ , $H_2$ |
| ***Zone 7*** | a-Si:H | $SiH_4$ , $H_2$ |
| ***Zone 8*** | n-a-Si:H | $SiH_4$ , $H_2$ , $CO_2$ , $PH_3$ |

Table 3.1: Different precursor gases for a-Si:H based solar cell deposition at HyET Solar (Reproduced from HyET Solar)

device two passes are done, first to deposit the top and consequently the second pass to deposit the bottom cell.

## 3.2 Lab-scale Cells on Foil (CoF) Processing

The traditional lab-scale samples processing route at HyET Solar involves mimicking all the steps involved in the production route as discussed in Section 1.3. The following section will briefly discuss the Cells on Foil (CoF) production route followed at HyET Solar.

- Sampling the roll : The TCO/Absorber layers are deposited on an Al foil using the baseline recipe. After the deposition process, the roll is cut into widths of 15 cm for further processing. Each 15 cm width is marked with a position on foil (PoF), which helps understand the different parameters used for different processes.
- Punching the roll : Each 15 cm PoF is then punched into 10x10 cm samples. For every PoF, two 10x10 cm samples are obtained.
- Laser scribing : After the punching process, the laser scribing is done as discussed in Section 2.4.3. Since it is a CoF, P2 is omitted from the process, while P1 scribe and P3 ink are dispensed.
- Deposition of back contact - The back contact is deposited via RF sputtering for AZO and DC sputtering for Al as discussed in Section 3.1.1.
- Opening the back contact interruptions : The P3 ink which is dispensed is open. The samples are rinsed in isopropanol (IPA) for 10 mins; after the rinsing, the P3 is removed using a cleanroom tissue. The process also removes the back contact on the top of the ink.
- Lamination of the carrier foil : Epoxy glue components are used for laminating the carrier foil on the top of the back contact. The lamination process is carried out in a vacuum process with a force of 18kN at 120 ∘C.
- First etch : The aim of the first etch is to reduce the thickness of Al foil to 20 microns. This is achieved by etching the CoF after lamination in a base at a certain concentration and temperature. The samples are rinsed in acid to clean off any residue base left from the etching process.
- Annealing : Etching can create mechanical stresses in the sample. If the stresses are excessive, they can create cracks in the TCO and break off the TCO layer. Hence, to reduce the samples' mechanical stresses and excessive curvature, the CoF's are annealed at a certain temperature inside an oven.
- Defining the bus bars : Etch resistant tape is used to define the bus bar area and the active area of the solar cell. The bus bar thickness is around 20 microns.
- Final etch : The final etch is done to remove the remaining 20 microns of Al from the active region to expose the cell to light. The final etch follows similar steps to the first etch and uses the same recipe for the etching.

The final CoF representation is shown in Figure 3.17. Here, four-probe measurements can be easily carried out for light and dark JV characteristics. Two probes are placed on the right bus bar, one on the left bus bar and one close to the TCO near the left bus bar.

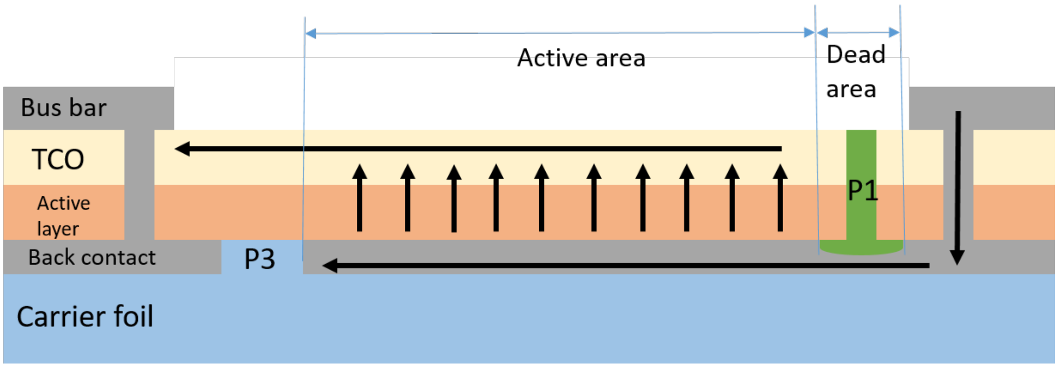

Figure 3.17: Cross section of a CoF under illumination, for a forward bias below Voc [Retrieved from HyET Solar]

## 3.3 Thin film characterization technique

The solar stack consists of many layers that need to be optimized individually to ensure the film's best optical, electrical, and structural properties. The different characterization techniques used in this work for getting feedback on the quality of the thin film are discussed in this section.

### 3.3.1 Spectroscopic Ellipsometer

Spectroscopic ellipsometry is one of the most powerful tools for characterizing a thin film's optical and structural properties. The samples under study are illuminated with a light of known polarization state as shown in the Figure 3.18. The polarized light is incident at a certain angle $\theta_0$ on the sample. This incident angle is close to the Brewster angle of the sample. The light is incident on the plane of incidence and reflected from the plane. The polarised component of light parallel to the plane is called p-polarized, while the perpendicular component is called s-polarized. The amplitudes of the s and p components, after reflection and normalized to the initial values, are represented by r$_p$ and r$_s$. The complex reflectance ratio which is $\rho$ in the Eq 3.2 is parametrized by the amplitude component ($\psi$) and phase difference ($\Delta$).

$$\rho = \frac{r_p}{r_s} = \tan\Psi \cdot e^{i\Delta} \tag{3.2}$$

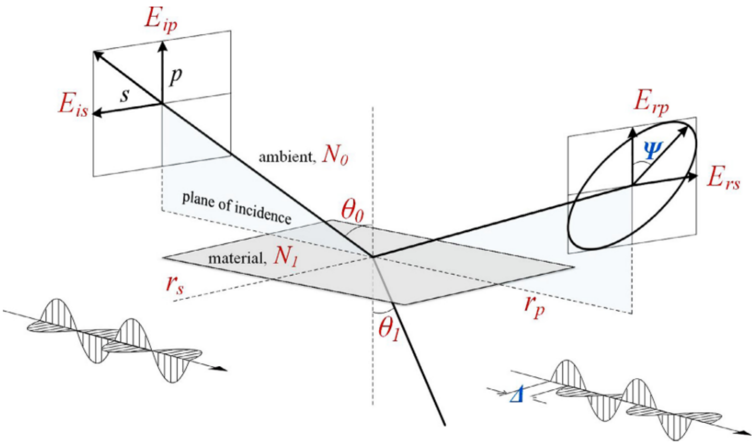

Figure 3.18: Ellipsometer measurement principle and geometry [43]

The equipment used for Spectroscopic Ellipsometer measurement is made from J.A.Woollam Co. The measurement yields the $\psi$ and  values in a complex curve based on the wavelength of the light as shown in Figure 3.19. The curve is fitted using different models to get the optical parameters from the measurement in the completeEASE software. Depending on the type of material and the type of model, different fits are generated. An iterative approach for fitting the curve is used with different oscillator models. The fit with a Mean Square Error (MSE) of less than ten is considered an accurate measurement.

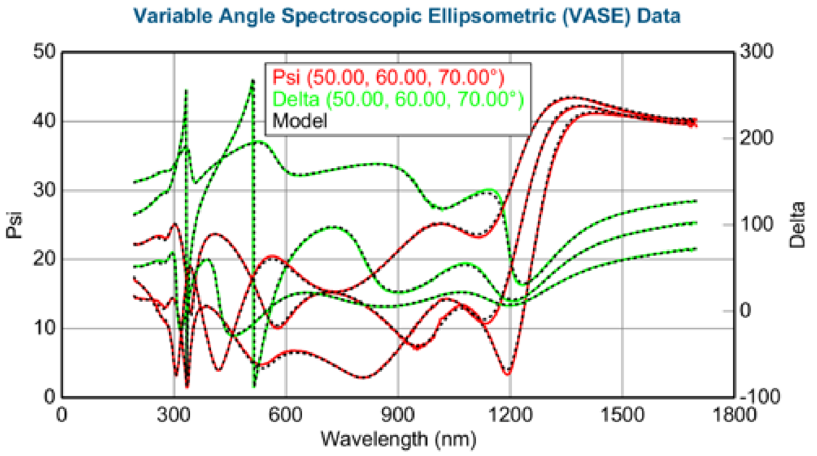

Figure 3.19: Ellipsometer measurement from the completeEASE software

### 3.3.2 Spectrophotometer

A spectrophotometer is a tool used to understand the transmission and reflection characteristics of a thin film. An incident light over different wavelengths is used to measure the reflectance and transmittance over a range of wavelengths. An optical path consisting of mirrors and diffraction gratings is used to generate a monochromatic beam of light. The monochromatic beam passes through the sample and finally reaches to an optical detector. The optical detector generates a signal which is then compared with a reference signal. Depending on the position of the sample in the measurement, the transmittance or reflectance can be calculated accordingly to the reference beam.

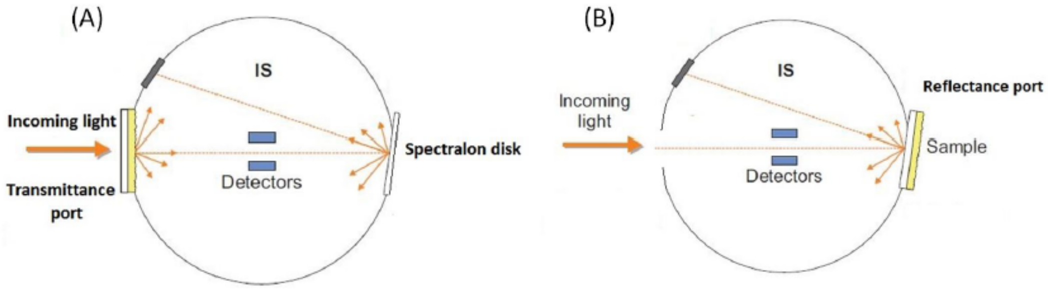

Figure 3.20: (A) Schematic diagram of transmittance in an Integrated Sphere; and (B) Schematic diagram of reflectance in an Integrated Sphere [44]

Figure 3.20 shows a typical schematic diagram of the Cary UV VIS equipment used to measure the transmittance and reflectance measurements. Here, the Integrated Sphere (IS) is coated with a material exhibiting Lambertian behaviour with a high refractive index [44]. The samples are placed in the transmittance port for the transmittance measurement, and the back portion of the IS is covered with a spectralon disk. Likewise, the samples are placed in the reflectance port for the reflectance measurements. For calculating the absorptance, the Eq 3.3 is used where A is the absorptance, T is the transmittance, while R is the reflectance of the sample measured.

$$A = 100 - (R + T) \tag{3.3}$$

### 3.3.3 Hall effect measurement

Hall effect measurement is a tool to understand the electrical properties of the thin film deposited. Here a uniform slab of electrically conducting material is placed in a perpendicular magnetic field through which a uniform current density flows. The Van der Pauw technique was used to measure carrier type, carrier concentration, the resistivity of the material, and the mobility of charge carrier [45]. As shown in Figure 3.21 the current (I) flowing through a sample under a constant perpendicular magnetic field (B), the charge carriers (q) with a velocity (v) undergo Lorentz force as shown in Eq 3.4. This force is experienced in a perpendicular direction to both the current and the magnetic field, resulting in charge carrier deflection in the y-direction as shown in Figure 3.21. The final result from the Hall effect suggests the electrical parameters for the charge carriers, which can be used to understand the film properties based on the deposition conditions.

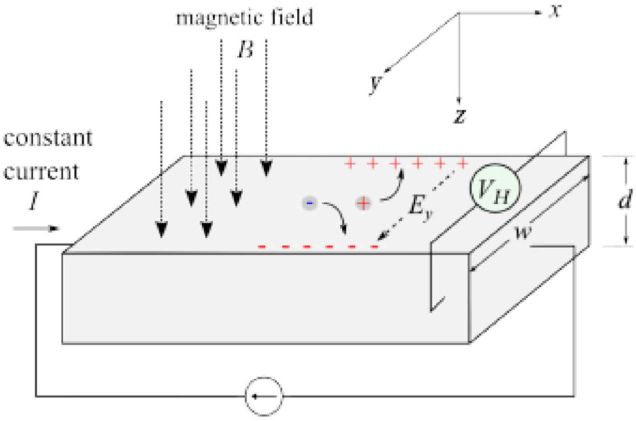

Figure 3.21: Schematic illustrating the Hall effect [45]

$$(F_L) = q \cdot v \times B \tag{3.4}$$

### 3.3.4 Scanning Electron microscope

The Scanning Electron Microscope (SEM) is a microscopic imaging technique used to produce images of the sample under consideration using a focused beam of electrons. The electrons are emitted from a light source to measure features that are smaller than the wavelength of light. The electrons are bounced off the surface producing secondary electrons, which are used to detect by a screen to produce the required image. All the measurements are done under a specific voltage, and the electromagnets help direct the electrons at the required surface. The desired sample is put under vacuum where the user can close up on nanometer and micrometer scale to understand the feature sizes and take images. The cross-section imaging can also be done using a SEM; however, the problem with SEM is that the sample needs to be cut, making it useless post measurement. For the scope of this work, the SEM was used to understand the morphological features of thin-film deposited under certain deposition conditions.

## 3.4 Solar cell characterization techniques

The solar cells processed at HyET Solar were characterized using a different technique to understand the material properties and optimize the production process. The following section discusses the working principle and the parameters for the different characterization techniques briefly.

### 3.4.1 Current-Voltage (IV) characteristics

The I-V curve can help understand the electrical parameters of the solar cell like the peak power (P$_{max}$), the short circuit current density (J$_{sc}$), the open-circuit voltage (V$_{oc}$) and the fill factor (FF). The measurements need to be performed under standard test conditions (STC). The STC conditions mean the spectrum should resemble AM1.5G, total irradiance on the solar cell to be 1000 W/m$^2$ and the temperature of the solar cell at measurement to be 25 °C.

- Short circuit current density : This parameter defines the total current that flows through the circuit under short circuit conditions. It depends upon the photon flux incident on the solar cell. Hence, the area of the solar cell becomes an important aspect. To remove the dependency on the area of the current densities are used. The maximum current in a solar cell can be optimized by better light management in the solar cell. Other important factors affecting the current generation are material parameters, surface recombination or diffusion length of the minority carriers.

- Open circuit voltage : Under the condition of open circuit, i.e. when no current flows through the circuit, the maximum voltage the solar cell can deliver is the open-circuit voltage. V$_{o}c$ depends on the saturation current density J$_0$ which depends on the recombination occurring in the solar cell. Therefore, V$_{oc}$ is the amount of recombination occurring in the solar cell. Furthermore, V$_{oc}$ can also refelct the bandgap of the material used.

- Fill factor : The FF of the solar cell is the ratio of maximum power (MPP) generated by the solar and the product of open-circuit voltage and the short circuit current density as shown in the Eq 3.5. The fill factor signals the recombination occurring in the solar cell. The ideality factor is another parameter that can affect the solar cell FF.

$$FF = \frac{J_{\mathrm{mpp}} V_{\mathrm{mpp}}}{J_{\mathrm{sc}} V_{oc}} \tag{3.5}$$

- Power Conversion efficiency : Based on the parameters discussed before we can calculate the conversion efficiency of the solar cell which is the ratio of maximum generated power with the incident power as shown in the Eq 3.6.

$$\eta = \frac{P_{\mathrm{max}}}{I_{\mathrm{in}}} = \frac{J_{\mathrm{MPP}} V_{\mathrm{MPP}}}{I_{\mathrm{in}}} = \frac{J_{\mathrm{sc}} V_{\mathrm{oc}} FF}{I_{\mathrm{in}}} \tag{3.6}$$

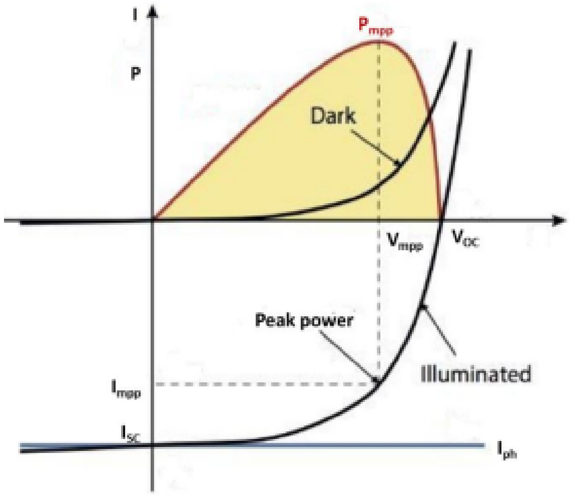

Figure 3.22: Dark and illuminated IV characteristics under AM1.5G spectrum using a solar simulator [12]

Figure 3.22 shows the typical current-voltage characteristics of a solar cell. Based on the IV curve, we can calculate all the parameters as discussed before. However, two crucial parameters can be calculated using the IV curve, which is series resistance (R$_{oc}$) and shunt resistance (R$_{sc}$). The R$_{p}$ can be calculated by getting the slope at the V$_{oc}$ under forward bias. The R$_{s}h$ can be calculated using the dark IV curve under the reverse bias region.

### 3.4.2 External Quantum Efficiency measurement

The external quantum efficiency (EQE) is the measurement that determines the ratio of the total number of electron-hole pairs that can be created in the absorber layer, which can be collected successfully to the fraction of photons incident on the solar cell [12]. The EQE measurement depends on the wavelength of the light incident and follows the Eq 3.7. Here, q is the elementary charge, $q\Psi_{\mathrm{ph},\lambda}$ is the spectral photon flow incident on the solar cell and $I_{\mathrm{ph}}(\lambda)$ is the photocurrent generated through the solar cell.

$$\mathrm{EQE}(\lambda) = \frac{I_{\mathrm{ph}}(\lambda)}{q\Psi_{\mathrm{ph},\lambda}} \tag{3.7}$$

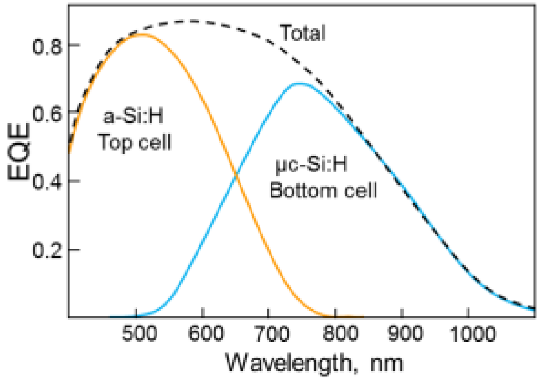

Figure 3.23: Typical EQE measurement for a micromorph solar cell [46]

Figure 3.23 shows a typical EQE measurement done for a micromorph (amorphous silicon/ microcrystalline silicon) solar cell. Here, the area under the curve can be used to calculate the J$_{sc}$. Moreover, the current of the lower cell in a tandem device acts as the current limiting influencing the J$_{sc}$. Hence, depending on the solar cell design and architecture, the bottom or the top cell can be the current limiting ones. Determining the J$_{sc}$ using the EQE measurement is advantageous as the measurement is independent of the spectral shape of the light source used in contrast to that of the IV measurement [12]. The shape of the EQE curve can suggest the optical and the electrical losses like parasitic absorption or recombination losses, respectively, occurring in the solar cell. The EQE curve, as suggested in Figure 3.23 can help to distinguish the current generation in different junctions in tandem and triple-junction solar cells. Here, the response can suggest the current limiting cell amongst the different junctions. In Figure 3.23 we can see that the short wavelengths up to 700 nm are absorbed in the top cell while the larger wavelengths are absorbed in the bottom cell. This measurement can help to optimize the cell architecture for better performance of the solar cell.

The EQE measurement is done using a spectral response setup [12]. The measurement is done using a xenon gas discharge lamp with a broad spectrum covering all the wavelengths. With the help of filters and monochromators, as shown in Figure 3.24 a narrow wavelength of photons energies can be incident on the solar cell. These different wavelengths can help bias a particular junction in the cell enabling the current generation measurement in a junction or a tandem cell. Another critical aspect of the measurement is the bias voltage which is a reverse bias voltage influencing the photocurrent density.

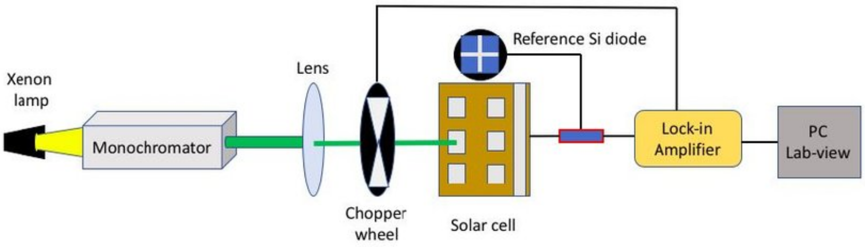

Figure 3.24: Schematic representation of EQE setup [44]

### 3.4.3 GenPro 4 for optical simulations

Apart from the measurements technique discussed in the previous sections, this work also focuses on the optical modelling of the solar cell stack for calculating the absorption, reflection, and eventually the photocurrent generation. GenPro4, a simulation tool developed by TU Delft, was used to optically stimulate the effect of different thin film properties on solar cell performance. The software uses MATLAB code for creating an environment where different layers and coatings can be used to develop a solar cell stack. The software uses wave and ray optics for stimulating the model. Various texturing features can also be implemented to ensure light trapping and other effects of light interaction between different layers.

The output from GenPro4 is absorptance against wavelength, which suggest all the absorption in different solar cell layers in the stack in terms of the photogenerated current density. The absorption in the intrinsic layers of the solar cell is of priority to improve the solar cell performance; however, the absorption in the other layers illustrate the parasitic absorption losses which need to be optimized. The current generated in the i-layer can be optimized by playing with different layer thicknesses and material properties. The GenPro4 provides vital information for the optical modelling; however, it is not the complete picture of the solar cell since GenPro4 does not account for electrical losses like recombination. Therefore, for a more accurate representation of the solar cell performance, GenPro4 is used with ASA (Advanced Semiconductor Analysis), a software developed by TU Delft. However, for this work, the optical simulations are the focus.

### 3.4.4 Advance Semiconductor Analysis (ASA) for electrical simulations

The Advance Semiconductor Analysis is a program designed by TU Delft for electrical simulations of amorphous and crystalline semiconductors. The ASA program solves the basic semiconductor equations like Poisson equation and two continuity equations for electrons and holes. Using the various advance physics model and material opto-electronic properties, 1-dimensional simulation of solar cells can be carried out.

Here in the scope of this work the ASA Software is used with to model the hydrogenated nanocrystalline silicon based solar devices. The FlamO1 which is Modulated Surface Texturing (MST) is used for the enhanced light trapping in the solar cells [47]. Hence, using the optical and electrical properties of various layers in the semiconductor device, the performance of the structure can be evaluated. The outputs from the ASA model can simulate the various electrical measurement parameters like EQE, JV and others. Using the results from ASA a case study has been developed to understand the PECVD tool at HyET Solar.

# Chapter 4

# Back contact sputtering process optimization

## 4.1 Introduction

The back contact sputtering process can introduce some of the defects causing lower shunt resistance or high open-circuit resistance as discussed in Sections 2.3 and 2.4. To understand these effects, an experiment was conducted where the aluminium-induced degradation effects were studied. The experiment aimed to understand the effect of back contact sputtering on the shunt resistance of the cell. A decrease in shunt resistance would increase the leakage current across the cell and degrade the performance. The back contact consists of a stack of 70 nm of aluminium-doped zinc oxide (AZO) layer and 300 nm of the aluminium layer. AZO, which is a TCO, provides enhanced light trapping while being conductive. Moreover, it acts as a diffusion barrier for aluminium. The role of the barrier is to prevent the p-i-p shunt model as a small incursion of Al into the absorber layers reducing the minority carrier lifetime. Hence, to understand the current configuration of the AZO layer, the experiment consisted of sputtering 4 by 4 mm diodes of silicon with back contact of two types of configurations.

The first stack consists of back contact with Al stack while the second stack comprise of just AZO/Al as the back contact as shown in Figure 4.1 and 4.2 . The diodes after sputtering are measured on dark JV to understand the leakage current across the solar cell. To understand the Al diffusion across the silicon layers, the diodes are annealed at 170°C for 20 mins. After the annealing, the diodes are again measured on the dark JV to understand the effect of annealing on the shunt resistance.

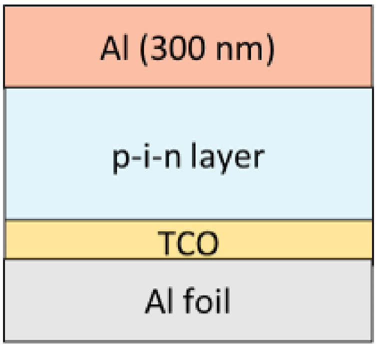

Figure 4.1: Single junction a-Si cell with Al as back contact

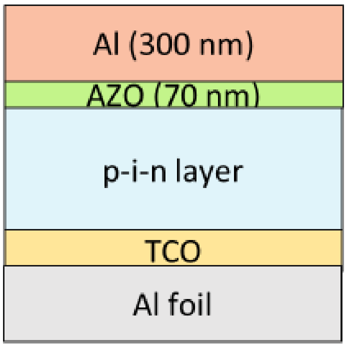

Figure 4.2: Single junction a-Si cell with AZO/Al as back contact

According to the shunt literature, as discussed in Section 2.3, annealing would enhance the Al diffusion into the n-type silicon layer, counter doping it to p-type. However, it is expected that the AZO interface should be thick enough to prevent the diffusion of Al. The results of the experiment are shown in Figure 4.3 to 4.6, where the ohmic shunt resistance ($R_p$) and non-ohmic shunt resistance

($R_{ppp}$) for both the types of stacks before and after annealing are plotted. Here, it can be observed that the diodes with AZO/Al as back contact have higher ohmic and non-ohmic shunt resistance when compared with diodes with just Al. Moreover, the spread in the shunt resistance observed is less for samples with AZO/Al as the back contact. The anomalies in the graph are for the diodes with wrong measurements due to bad contact. There is a decrease in the shunt resistance after annealing for both the configurations of the back contacts. This is expected for diodes with Al as back contact as the annealing process would enhance the diffusion; however, the marginal decrease in the shunt resistance was not expected for the AZO/Al configuration.

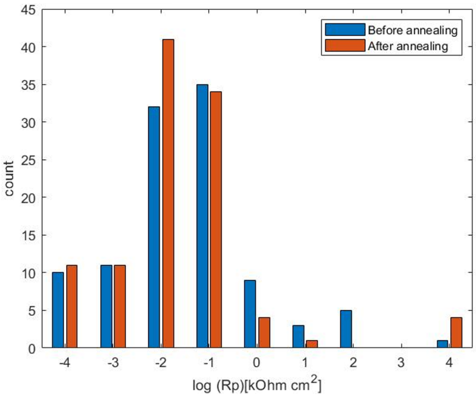

Figure 4.3: Comparison of $R_p$ for before and after annealing with Al as back contact

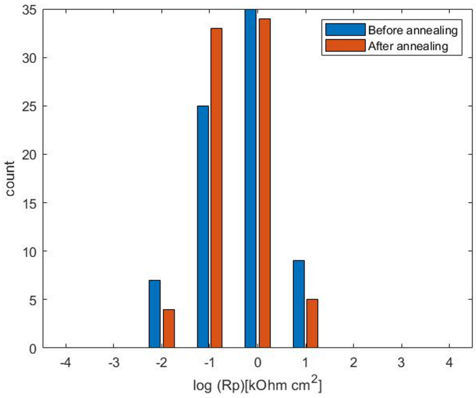

Figure 4.4: Comparison of $R_p$ for before and after annealing with AZO/Al as back contact

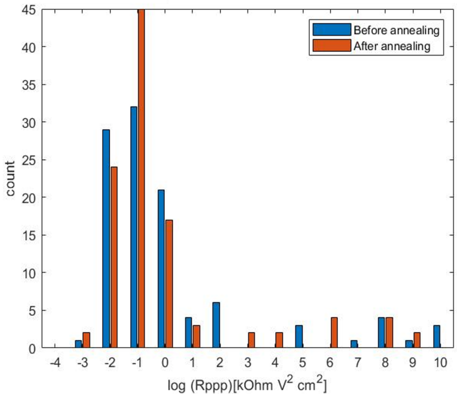

Figure 4.5: Comparison of $R_{ppp}$ for before and after annealing with Al as back contact

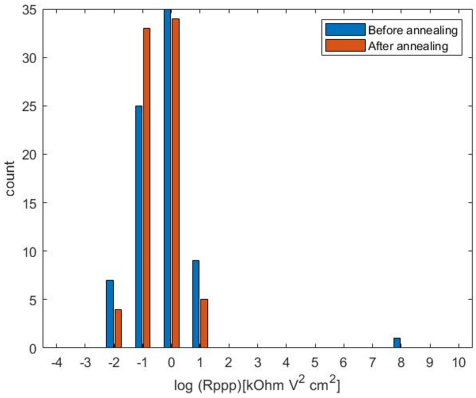

Figure 4.6: Comparison of $R_{ppp}$ for before and after annealing with AZO/Al as back contact

The trend as suggested in Figure 4.3 and 4.4 can be attributed to the fact that the back contact sputtering deposition tool at HyET Solar, Arnhem, has been conditioned to many changes over the years. Hence, the deposition conditions for the RF sputtering might not be optimum for the best electrical and optical performance resulting in the degradation of the performance of solar cells fabricated. Furthermore, the standard thickness of 70 nm of the AZO layer might not be achieved due to changes in the equipment. Therefore, to optimize the back contact sputtering deposition at HyET Solar, a two-level two-factor screening design of experiment (DoE) was conducted.

## 4.2 Design of Experiment

The sputtering deposition conditions can depend on various factors as discussed in Section 3.1.1, however, the sputtering tool at HyET Solar manufactured by Leybold, can be optimized based on pressure

| | |
|---|---|
| **Target** | ZnO +2% at Al2O3 |
| **Base pressure** | 1e-5 Pa |
| **Substrate to target distance** | ~5.5 cm |
| **Substrate temperature** | RT |
| **Sputtering time** | 21.9 mins |
| **Substrate rotational speed** | 11 s/round |
| **Ar gas flow** | 40 sccm |
| **RF power** | 407 W |

Table 4.1: Base conditions for back contact sputtering at HyET Solar

| | **RF Power (W)** | **Ar flow (sccm)** |
|---|---|---|
| **Setting 1** | 407 | 40 |
| **Setting 2** | 407 | 4 |
| **Setting 3** | 507 | 4 |
| **Setting 4** | 507 | 40 |
| **Setting 5** | 457 | 22 |

Table 4.2: Design of experiment for 2 level 2 factor screening

of the gas in chamber and the power of the generator. Since the aim of the experiment is to optimize the sputtering conditions for AZO layer, the RF Power and the flow rate of Ar in the chamber the two factors which need to be optimized to obtain the thin film with desired properties.

The base conditions for sputtering at HyET Solar are discussed in Table 4.1. According to the literature as discussed in Section 3.1.1, a higher RF power and a lower chamber pressure results in a dense and compact film deposition. This is due to the fact a higher power would impart more kinetic energy to the atoms resulting in more surface mobility leading to a denser film. The lower chamber pressure would ensure less loss of kinetic energy of the AZO atoms providing larger crystallite growth with less voids. The table 4.2 shows the different settings for the RF power and Ar flow rate used in the design of experiment. Here, all the settings are chosen to revolve around the center point. The minimum Ar flow rate possible which can ignite the plasma is chosen as the lower setting in the design of experiment. Moreover, Setting 1 is the baseline setting which is the historic setting used at HyET Solar.

Based on the design of experiment different samples are prepared depending on the type of characterization techniques. The design of experiment settings is characterized optically and electrically. The following section discusses the results obtained for the best deposition condition for sputtering the back contact.

## 4.3 Results

### 4.3.1 Optical characterization

The AZO thin film sputtered for the different deposition conditions are measured on spectroscopic ellipsometer and spectrophotometer. The transmission and reflection parameters generating the data for absorption, the refractive indexes are considered as the parameters to characterize the films optically.

#### 1. Spectroscopic Ellipsometer

The spectroscopic ellipsometer is used as a characterization technique first to understand the thickness of AZO film sputtered in the back contact deposition technique at HyET Solar. Additionally, the results from the measurement are used to analyze the refractive index values (n and k) of the thin film. The AZO film was sputtered on glass samples, which were rinsed in IPA for 10 mins before the deposition. The glass samples were taped from behind to provide the required reflection conditions for the measurements. The principle of the measurement is to understand the change in the polarisation of light after being reflected form the AZO surface using the amplitude ratio of two perpendicular

| | ***RF Power densities (W/cm$^2$)*** | ***Corresponding sputter pressure (Pa)*** | ***Thickness (nm)*** | ***Deposition rate (nm/min)*** |
|---|---|---|---|---|
| ***Setting 1*** | 1.30 | 5.8 | 87.14 | 3.98 |
| ***Setting 2*** | 1.30 | 2.1 | 107.71 | 4.92 |
| ***Setting 3*** | 1.61 | 2.1 | 146.93 | 6.71 |
| ***Setting 4*** | 1.61 | 5.8 | 121.86 | 5.56 |
| ***Setting 5*** | 1.46 | 4.9 | 116.06 | 5.30 |

Table 4.3: Results from Spectroscopic Ellipsometer measurement

polarized beams as discussed in Section 3.3.1. The $\Psi$ and $\Delta$ values observed were then fitted using various oscillator models. Since AZO is a transparent conductive oxide, it becomes important to fit the data with Gen-Osc models available. The imaginary part of the complex dielectric function was fitted using a combination of oscillator models. First, the Tauc-Lorentz oscillator is used to fit the absorption in the UV range. The Drude oscillator is used to fit the absorption caused by the conductivity. Finally, the Gaussian oscillator is used to model the real part of material.

Based on the results of ellipsometer measurements the deposition rates was calculated as shown in table 4.3. The thickness parameter from the fitted data is used with the sputtering time to understand the deposition rates. Using the deposition rates a next batch of the samples for the DoE was deposited. The results from the Ellipsometer measurement suggested that the thickness of the new deposition AZO film for all the settings were in the range of 70 nm. Finally the results for the optical characterization are based on these measurements.

The obtained values for the refractive index from the ellipsometer measurement are plotted in Figure 4.7 and 4.8. Here, the average value of n and k in the visible region was highest and lowest respectively for Setting 1 as shown in Table 4.4. For Setting 4 the highest k value and lowest n value were observed. The higher RF power and higher sputter pressure corresponds to higher absorption characteristics in the AZO film deposited. Hence suggesting the film deposited under lower power condition and lower sputter pressure condition seems to provide the best optical properties. Moreover, the values from the ellipsometer measurements were further used in GenPro4 to stimulate the effect of current absorption in the absorber layers. The code used for the simulation is shown in Appendix A.

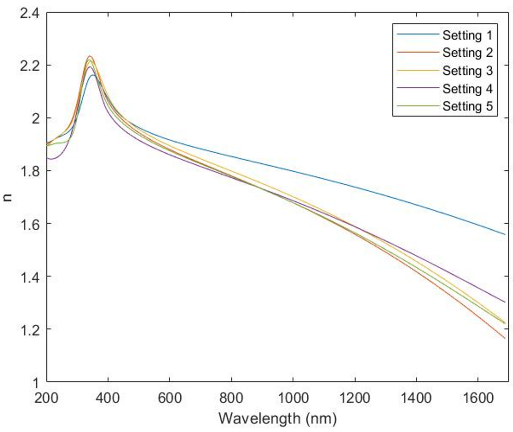

Figure 4.7: Refractive index n value from Spectroscopic Ellipsometer measurement for DoE

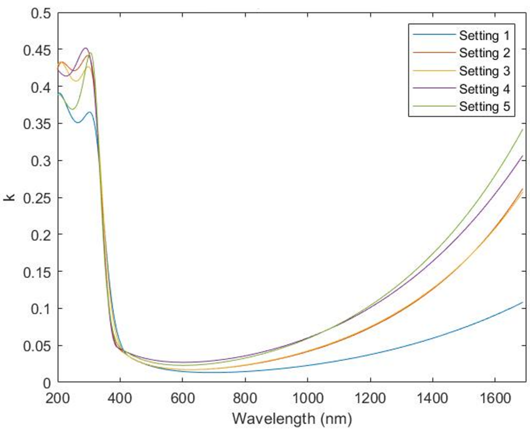

Figure 4.8: Refractive index k value from Spectroscopic Ellipsometer measurement for DoE

| | Average n (in the visible region) | Average k (in the visible region) |
|---|---|---|
| **Setting 1** | 1.9455 | 0.0228 |
| **Setting 2** | 1.9142 | 0.0238 |
| **Setting 3** | 1.9293 | 0.0245 |
| **Setting 4** | 1.8903 | 0.0319 |
| **Setting 5** | 1.9069 | 0.0292 |

Table 4.4: Results from Spectroscopic Ellipsometer measurement after optimizing the thickness of the AZO layer

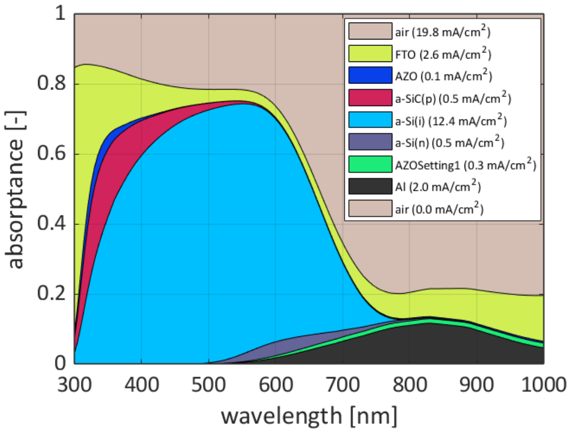

Figure 4.9: GenPro4 stimulation results for Setting 1

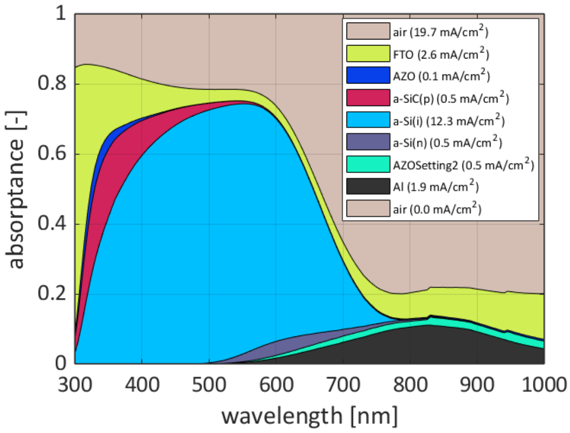

Figure 4.10: GenPro4 stimulation results for Setting 2

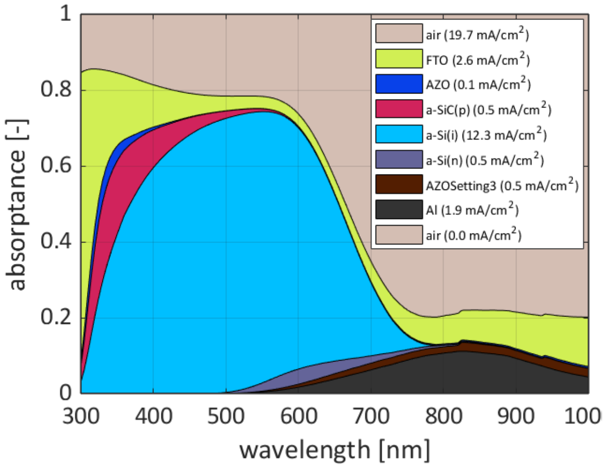

Figure 4.11: GenPro4 stimulation results for Setting 3

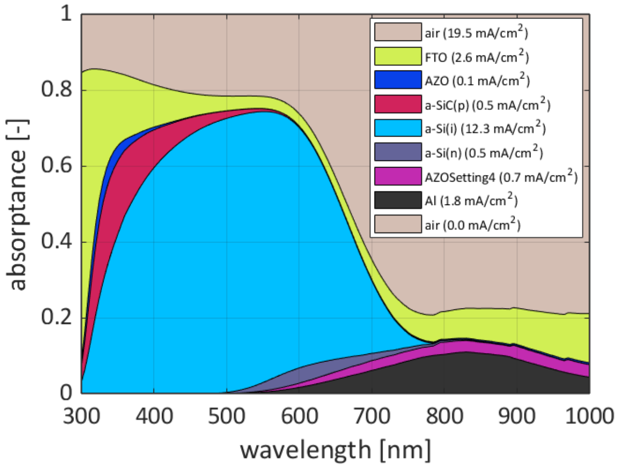

Figure 4.12: GenPro4 stimulation results for Setting 4

The absorptance results from GenPro4 stimulation are shown in figure 4.9,4.10,4.11,4.12 and 4.13. Here in the Figure 4.13 it can be observed that in Setting 5 the absorption in AZO layer in the back contact increases by 0.3 mA/cm$^2$. This increase in absorption in the back contact layer results in decrease in the current generation in the absorber layers. It can be observed that Setting 1 offers higher current absorption in the intrinsic layers which is higher by 0.1 mA/cm$^2$ when compared to the other settings. The Setting 2 and Setting 3 show similar absorption results for the AZO layer suggesting that the RF power does not affect the optical properties and hence, not affecting the absorption in the AZO layer. However, when we increase the sputter pressure to the highest in Setting 4 with the highest RF power we can observe an increase in the absorption in the AZO layer to 0.7 mA/cm$^2$. This trend is also seen in Setting 5 where the absorption increases to 0.6 mA/cm$^2$. To conclude, the Ellipsometer measurements suggest that lower power is beneficial to improve the optical properties of the thin film deposited. However, a higher sputtering pressure provides better reflection into the absorber layers while improving the current generated in the intrinsic layer by 0.1 mA/cm$^2$.

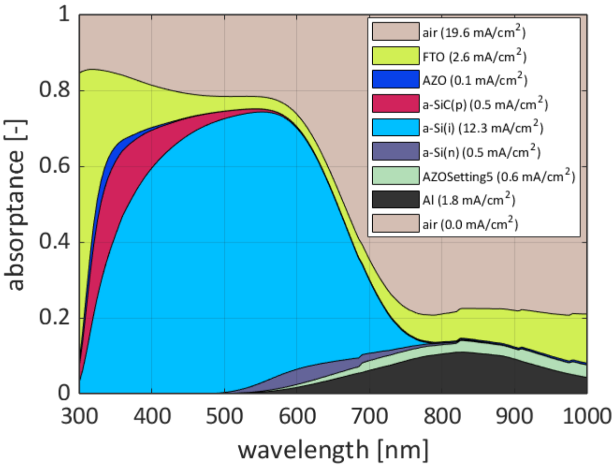

Figure 4.13: GenPro4 stimulation results for Setting 5

## 2. Spectrophotometer

The spectrophotometer measurements are used to understand the transmission and reflection properties of the different AZO film deposited in the DoE. The absorption in different films are calculated using the transmission and reflection data from the spectrophotometer. The absorption data is plotted in the Figure 4.14. The absorptance in the film is calculated using the Eq 3.3 as discussed in Section 3.3.2. In the Figure 4.14 it can be seen that the lower sputter pressure settings have very low absorptance characteristics.

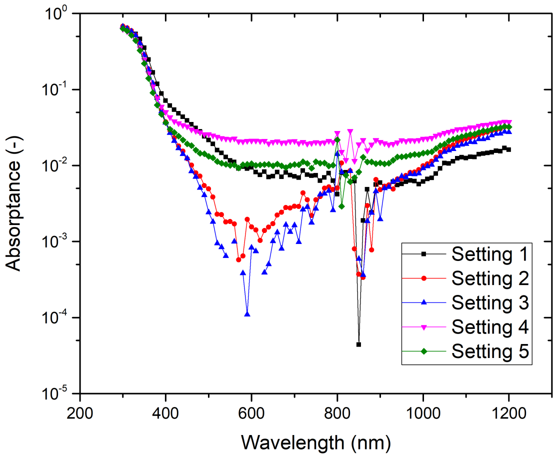

Figure 4.14: Absorption results from Spectrophotometer measurement

The absorptance values were used to calculate the photocurrent density lost in the film due to the absorption of light. The photon flux and the absorption values were used to calculate the J$_{phloss}$. Table 4.5 shows the photocurrent density loss (J$_{phloss}$) in mA/cm$^2$ for the different sputtering conditions. Here, it can be observed that the RF Power does not influence the absorption characteristics in the film, as the Setting 2 and Setting 3 with a difference of 100 W in the power do not show major difference in the J$_{phloss}$. However, the Ar flow rates play a major influence on the transmission and reflectance characteristics of the film. A lower Ar flow rate helps to decrease the absorption in the AZO film as seen from the Table 4.5. The highest losses in the AZO films were observed for the Settings with the highest Ar flow rate. This means a higher flow rate would translate to higher sputtering pressure which results in more collisions in the AZO atoms leading to a lower kinetic energy. This lower kinetic energy would mean lower mobility for the atoms which results in smaller crystallite sizes in the film growth. The film grown with lower crystallite sizes would have more voids and be more porus which can reduce the transmission across the film.

| | **Power (W)** | **Ar Flow rate (sccm)** | **Jph_loss (mA/cm2) in 300-1200 nm** |
|---|---|---|---|
| ***Setting 1*** | 407 | 40 | 0.890 |
| ***Setting 2*** | 407 | 4 | 0.642 |
| ***Setting 3*** | 507 | 4 | 0.588 |
| ***Setting 4*** | 507 | 40 | 1.319 |
| ***Setting 5*** | 457 | 22 | 0.870 |

Table 4.5: Results from Photocurrent density loss (J$_{ph_loss}$) due to absorption in the AZO film deposited under the different sputtering conditions

To conclude, the optical characterization of the AZO film was done using spectroscopic ellipsometer and spectrophotometer. The ellipsometer measurements were used to stimulate the current absorption in the intrinsic layer. The results from both GenPro4 and the spectrophotometer suggest that at low sputter pressure the influence of RF power becomes negligible. The results from the stimulation suggests that a lower RF power and higher sputter pressure provides the best reflection in the intrinsic layer from the AZO layer. However, the film absorptance when calculated from the spectrophotometer measurements suggest lower sputter pressure is preferred to avoid more parasitic absorption in the AZO layer. This difference in the results can be attributed to the fact under a solar cell structure as stimulated in GenPro4, we can observe different performance due to the presence of consequent layers. The transmission and reflection measurement might suggest better properties on glass under certain conditions, however, that might not be the case when the film is placed in a solar cell stack.

### 4.3.2 Electrical characterization

Apart from optical properties of the TCO, electrical properties are another important aspect of the films. The mobility of free electrons and the resistivity are important parameters that can define the electrical performance of the thin film. The following section discusses the electrical characterization based on Hall effect and dark JV measurement.

#### 1. Hall effect measurement

To understand the electrical characterization of the different settings, hall effect measurement was done. The objective of the measurement was to understand the optimum electrical parameters for the deposition conditions. The films were analyzed on the mobility, the resistivity and bulk concentration. The relation between conductivity and the mobility of the electrons is shown in Eq 4.1, where , n is the number of electrons per unit volume, e is the elementary charge and $\mu$ is the mobility. The conductivity is directly proportional to the mobility of the electrons inside the film. Since resistivity is the measure of resistance to flow of electrons, the mobility and the resistivity are inversely proportional to each other.

$$\sigma = ne\mu_e \tag{4.1}$$

| **Ar flow rate (sccm)** | **Sputter pressure (mbar)** |
|---|---|
| 4 | 0,021 |
| 22 | 0,049 |
| 40 | 0,058 |

Table 4.6: Sputter pressure based on the flow rates of Argon

| | Bulk concentration (cm-3) | Sheet concentration (cm-3) | Resistivity (ohm cm) | Conductivity ((ohm cm)-1) | Mobility (cm2/Vs) |
|---|---|---|---|---|---|
| ***Setting 1*** | 2.54E+19 | 1.77E+14 | 8.78E-02 | 1.14E+01 | 2.81E+00 |
| ***Setting 2*** | 1.55E+20 | 1.08E+15 | 2.43E-03 | 4.11E+02 | 1.66E+01 |
| ***Setting 3*** | 1.36E+20 | 9.54E+14 | 3.44E-03 | 2.90E+02 | 1.33E+01 |
| ***Setting 4*** | 3.58E+19 | 2.51E+14 | 3.49E-02 | 2.86E+01 | 4.99E+00 |
| ***Setting 5*** | 1.26E+20 | 8.80E+14 | 8.21E-03 | 1.22E+02 | 6.05E+00 |

Table 4.7: Results from Hall effect measurement showing the bulk concentration, sheet concentration, resistivity, conductivity and mobility

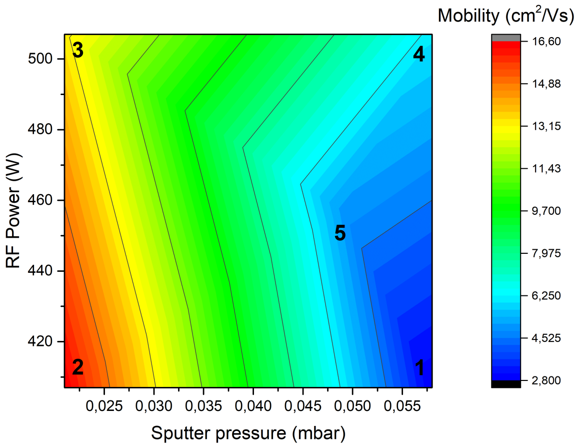

Figure 4.15: Heat map for mobility of electrons under different deposition conditions

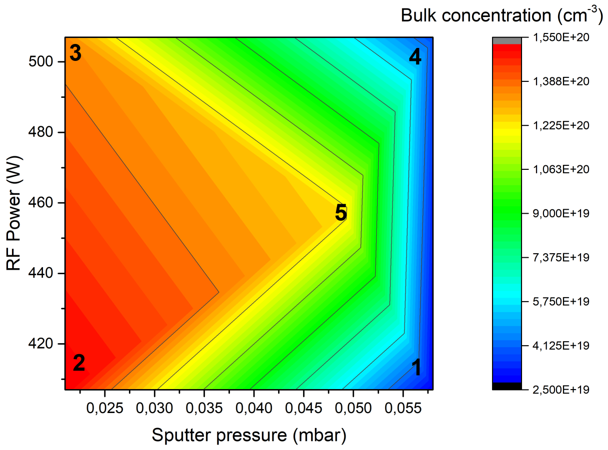

Figure 4.16: Heat map for bulk concentration of electrons under different deposition conditions

Table 4.6 represents the flow rate used in the design of experiment in terms of the chamber pressure for sputtering. Table 4.7 shows the results observed from the Hall effect measurement. To provide a better picture into the results heat map for mobility and bulk concentration against the effect of the sputter pressure and RF power is plotted. It can be seen from Figure 4.15 the lower sputter pressure and lower RF power provides the highest mobility of electrons. The Setting 1 which is the baseline setting has the highest sputter pressure offers the lowest mobility. While Setting 2 with the lowest RF power and lowest Ar flow rate offers the best mobility. Hence, ideally it is justified to go to a lower sputter pressure and power to improve on the electrical properties of the thin film. Similar trend can be observed for Figure 4.16 where a lower sputter pressure offered the best bulk concentration while a higher pressure which is for the baseline setting offers the lowest value.

### 2. Dark JV measurement

The settings as discussed in Table 4.2 was used to fabricate 4x4 mm diodes with back contacts under different conditions. These diodes were then measured on dark JV measurement to understand the effect of sputtering on the shunt resistance. Here, the stack consisted of Al/TCO/a-Si:H/Back contact layers. The deposition rates were used from the calculations done in the Ellipsometer measurement as shown in the Table 4.3.

The Figure 4.17, 4.18, 4.19, 4.20 and 4.21 show the results of the shunt resistance measured under dark conditions. Here, the ohmic component of the shunt resistance (R$_p$) is plotted in a logarithmic scale. The non-ohmic components (R$_{ppp}$) are shown in the Appendix B. As discussed before, a higher shunt resistance is ideally better for a solar cell. This is due to the fact that a higher shunt resistance offers more resistance to leakage current in a solar cell. However, since the absorber layers in the stack consists of single junction solar cell, we expect lower shunt resistance in general. The thickness of the stack can influence the leakage current, as more defects are found in thin material.

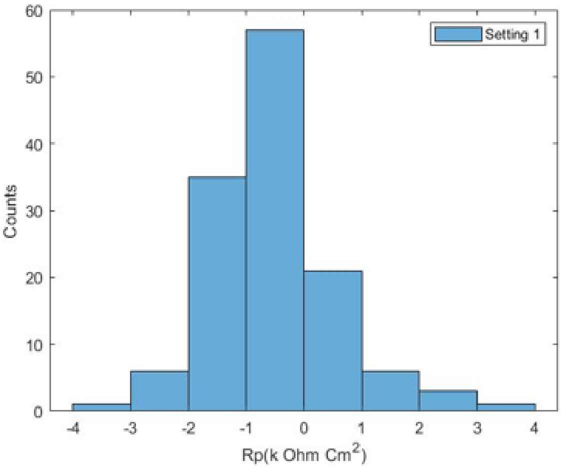

Figure 4.17: Dark JV measurements for diodes for Setting 1

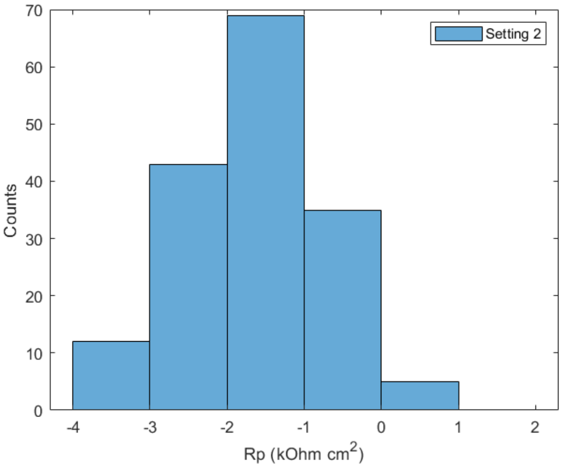

Figure 4.18: Dark JV measurements for diodes for Setting 2

It can be observed from the Figure 4.17 the baseline conditions offers a very large spread in the shunt resistance. Although, there are few diodes with very high R$_p$, however, the majority of the diodes have very low R$_p$ in the range of 0.1 to 0. This suggest that most of the diodes are shunted. When Figure 4.17 and 4.18 are compared it can be seen that a lower sputtering pressure does not effect the shunt resistance as we do not see any improvement in the R$_p$. However, when we increase the RF power, we observe more diodes with higher R$_p$ in the range between 1 and 10 as seen in the Figure 4.20. Setting 4 in comparison with Setting 3 shown in Figure 4.19 suggest that a higher RF power does not cause ion bombardment on the film and create the defects that can introduce shunting effects. For Setting 5 as seen in Figure 4.21 follows a similar trend as seen in Setting 1, suggesting the RF power is not high enough to create any difference. To conclude, a higher RF power and higher sputter pressure provided the best results for diodes when compared on the shunt resistance measurement.

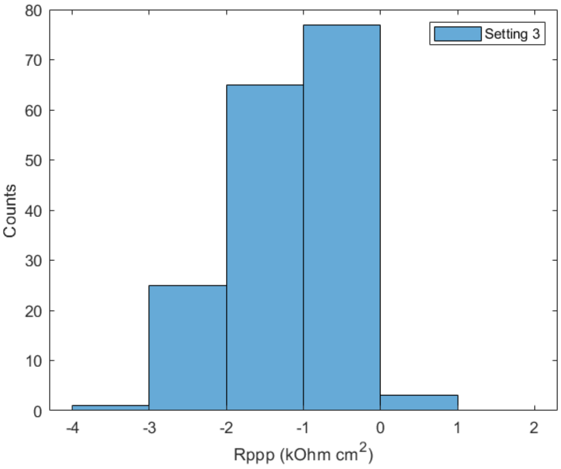

Figure 4.19: Dark JV measurements for diodes for Setting 3

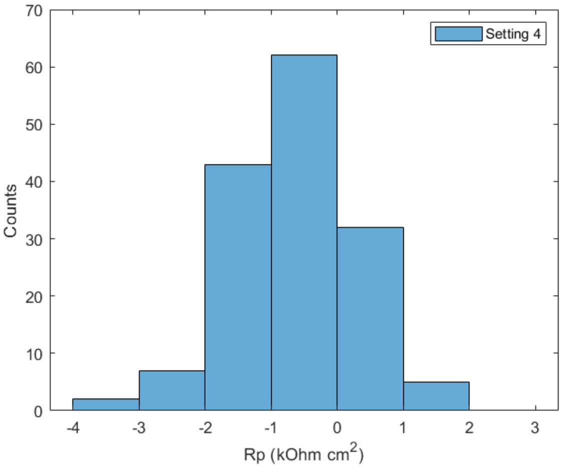

Figure 4.20: Dark JV measurements for diodes for Setting 4

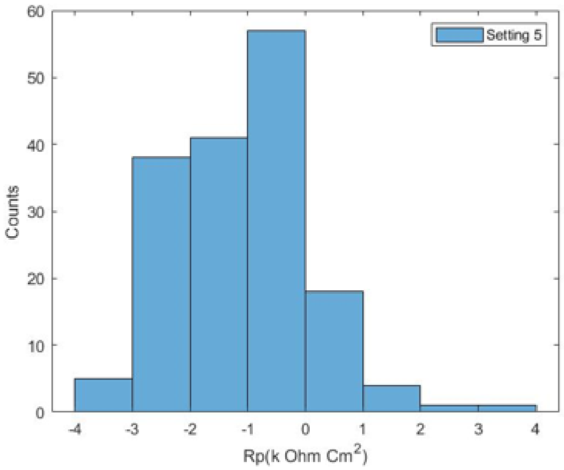

Figure 4.21: Dark JV measurements for diodes for Setting 5

## 4.4 Conclusion and recommendation

The back contact sputtering process has been studied at HyET Solar. The process has been considered as one of the potential causes of low performance of the lab samples produced at HyET Solar. To understand the effect of AZO film on the shunt resistance an experiment was conducted. It was concluded that the film thickness needs to be optimized as over the years the sputtering tool at HyET Solar has been subject to changes. To understand the film quality, optical and electrical characterizations were done. Finally, the sputtering time to deposit 70 nm thickness of AZO was updated. The selection of the optimal deposition conditions based on electrical and optical criteria is not as straightforward. The results from Hall effect suggested lower sputter pressure is preferred, however, this was not the case for the optical properties. The experiment was concluded based on GenPro4 results which suggested an increase in intrinsic layer absorption when AZO is deposited at baseline setting (Setting 1).

Furthermore, a recommendation will be to process CoF's or SuperCoF's based on different setting to understand the effect of sputtering on the device performance. The measurement would give feedback on the R$_{oc}$ and R$_{sc}$ component of the solar cell. This could not be done in the current scope of work due to unavailability of stable p-i-n stack that could be have been processed.

Another recommendation would be to cross-section TEM or SEM images to understand the morphological features of the AZO layer deposited. However, this becomes a difficult measurement due to the laminate carrier foil which can interfere with the measurement.

# Chapter 5

# Development of SuperCoF processing route for lab scale thin-film solar cells

## 5.1 Background

The current processing of lab scale samples at HyET Solar as described in Section 3.2 has witnessed problems of low performance and slow learning cycles due to the unavailability of the laser scribing tool. The monolithic series interconnection process can induce factors which can influence the performance in lab samples. Hence, to understand the absorber layer quality and to have faster learning cycles a new method of fabricating lab scale flexible thin film solar cells called ”SuperCoF” (Super Cells on Foil) is developed. The major challenge in the development of SuperCoF is to separate solar cells from the adjacent cell while having bus bars enabling the current measurement across the cell. Before processing of lab scale solar cells, a stack of aluminum/TCO/absorber layers is used as shown in Figure 5.1. Here the absorber layers can be a-Si:H, a-Si:H/$\mu$c-Si:H or a-Si:H/$\mu$c-Si:H/$\mu$c-Si:H based. After the absorber layers are deposited, the SuperCoF configuration can be processed. The following section will discuss the background behind the concept of SuperCoF.

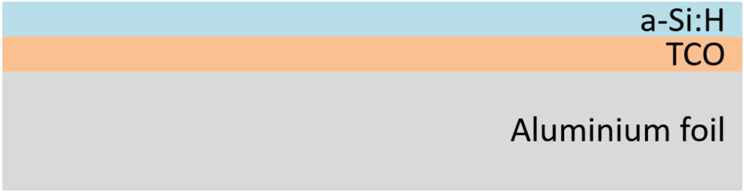

Figure 5.1: Basic stack used of processing of SuperCoF consisting of Al foil/TCO/Absorber layers

### 5.1.1 Back contact sputtering

On a stack of aluminum/TCO/absorber layers the back contact is sputtered. The back contact should be deposited in such a way that it can be contacted after the fabrication process to be able to measure the voltage and current characteristics as shown in the Figure 5.2. The contact to the back contact is to be done through a pin probe or crocodile probe. Furthermore, the back contact area should be optimized as small areas can cause problems of shunting Hence, different configurations of the back contact area needs to tested. The back contact is sputtered using polymer masks.

Figure 5.2: Back contact sputtering step for SuperCoF processing

The initial mask developed for the back contact sputtering is shown in Figure 5.3. Here, a back contact area of 7 $cm^2$ was used to understand the lamination and etching strategy for the SuperCoF processing. The sputtered back contact area is shown in red while the aluminum stack used is shown in grey.

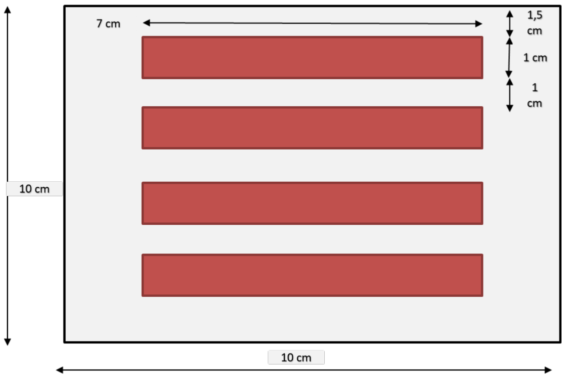

Figure 5.3: Initial mask design developed for the back contact sputtering for SuperCoF processing

### 5.1.2 Lamination of carrier foil

After the back contact is sputtered the next step is to laminate the carrier foil. The lamination of the foil is to transfer the mechanical stresses from the FTO to the carrier foil. The lamination needs to ensure that the sputtered back contact can be contacted after the lamination. This step is the most critical phase in the development of SuperCoF since the lamination can limit the ability to contact the front and back side of the solar cell stack. Hence, the initial idea of laminating the lab samples was laminating of back contact partially. This would enable direct contact on the back contact areas where there is no lamination foil.

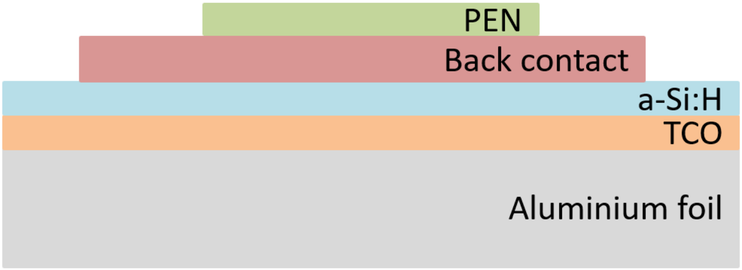

Figure 5.4: Lamination step for SuperCoF processing

The initial lamination strategy is shown in Figure 5.5 depicts the lamination foil in green. As suggested in the figure the back contact is not fully covered with the lamination foil. This helps to contact

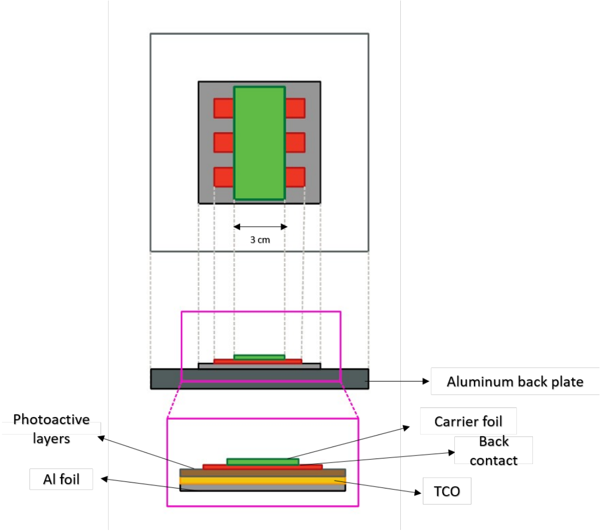

Figure 5.5: Initial lamination strategy used for processing of SuperCoF shown in top and front view. Cross-section zoomed to show the various layers in the stack

the back contact even after the lamination process.

To understand the back contact conductivity across the solar cell a measurement using a multimeter was investigated. Figure 5.6 shows the simple experiment conducted to understand the conductivity of the back contact after the lamination process. With a resistance measurement of 0.1 Ω it was concluded that the back contact is conductive throughout even after the lamination process suggesting the validation of the approach of SuperCoF.

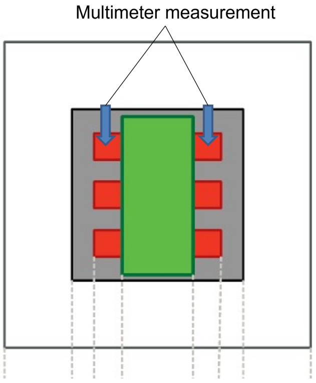

Figure 5.6: Multimeter measurement to understand the conductivity of the back contact in the initial phase of development of SuperCoF

### 5.1.3 First etching process

The first etching process aims to reduce the thickness of the aluminum foil to 20 microns. The etching in done in a base bath with subsequent cleaning processes carried out in acid bath. Since the whole stack is not laminated, the back contact has the risk of being etched away due to the attack of the etchants.

The Figure 5.7 shows the front side of the SuperCoF with the etching tapes to protect the regions without the lamination foil. The lamination foil acts as a protecting layer to the etching mechanism, however, since this SuperCoF configuration does not have a complete lamination foil across the aluminum foil the etchant can etch away the back contact, silicon layers and the FTO. Hence, the strategy of etching needs to protect the solar cell stack from the attack of etchants. Further in this report, we

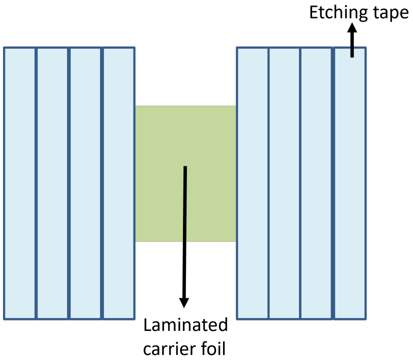

Figure 5.7: Front side of solar cell covered with the etching tape

discuss the 2 strategies for etching process for the SuperCoF processing.

### 5.1.4 Annealing process

The annealing process for the SuperCoF is a heat treatment for the solar cells for a certain duration of time at a desired temperature. The annealing process transfers the stresses from the FTO to the carrier foil. This helps to prevent the breakage of TCO layer under the final etching procedure.

### 5.1.5 Final etching process

The final etching process is the last step in processing of the SuperCoF. The final active region is defined with the use of etching tapes. Figure 5.8 shows the final output from the SuperCoF processing. To contact the cell, one of the probes can contact directly the back contact and the other probe can be placed on the aluminum foil. This placement of the probes helps in the current movement across the cell as shown by the black lines in the Figure 5.8.

To conclude, the Section 5.1 discussed the initial concept of processing of solar cells without the monolithic interconnection process. The main concepts is to develop optimized back contact area that can be contacted using a measurement system. Moreover, understanding the lamination process to be able to transfer the stresses. Finally, understanding the etching process to make sure the etchant does not attack the solar cell stack.

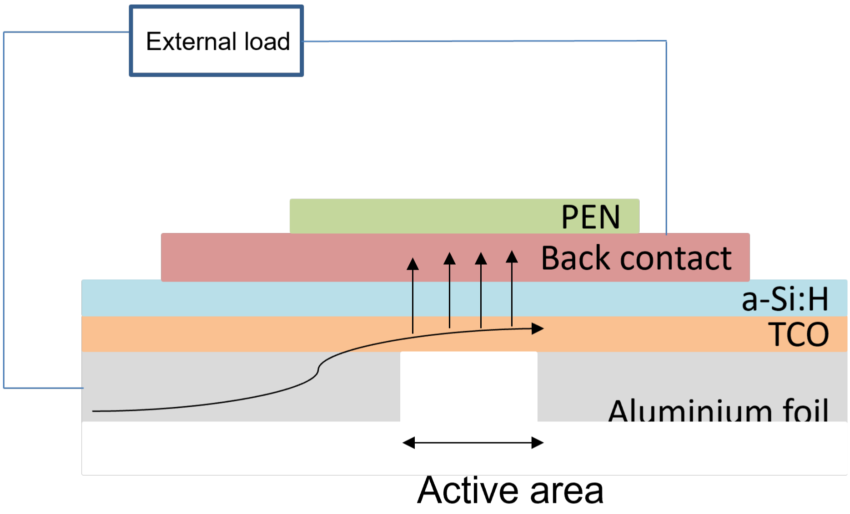

Figure 5.8: Final SuperCoF cell in its initial development stage

In further sections the initial concept discussed in Section 5.1 will be validated. Furthermore, different approaches developed for the processing the SuperCoF will be investigated. Finally, the results from the fabrication of triple junctions solar cells are discussed.

## 5.2 Approach 1

The first approach for fabricating of SuperCoF is to **"Creating contact through the carrier foil"**. This approach is based on contacting the back contact through an external layer like a copper tape. The carrier foil needs to be either cut after the lamination to contact the copper tape or the tape needs to be protruding out of the stack. The former has a problem of etching as the etchant can seep in the carrier foil, damaging the back contact and the other layers. Although, the incision step for contacting the back contact through the carrier foil was the initial approach for the contact through the carrier foil, however, due its problems of delamination and etchant attack the approach was modified. The modified approach will be discussed in the following section, explaining all the steps undertaken for the development of SuperCoF. Moreover, at every step of the process a dark JV measurement is conducted to understand the effect of processing on the shunt resistance.

**Step 1**

The first step as already discussed in Section 5.1 is to sputter the back contact on the the Al foil/TCO/a-Si:H stack as shown in the Figure 5.9. The back contact sputtered is in a shape of rectangle with fingers to enable the contacting the copper tape. The final optimized back contact shape is shown in Figure 5.11. The shape consists of a finger with an area of 0.15 $mm^2$ which is used to contact the copper tape. The active area is 0.72 $mm^2$. Each 10x10 cm of the solar stack would consist of 20 solar cells. Furthermore, the Figure 5.10 shows the dark JV curve for the cell after sputtering. This helps to identify if the back contact was sputtered properly on the solar stack.

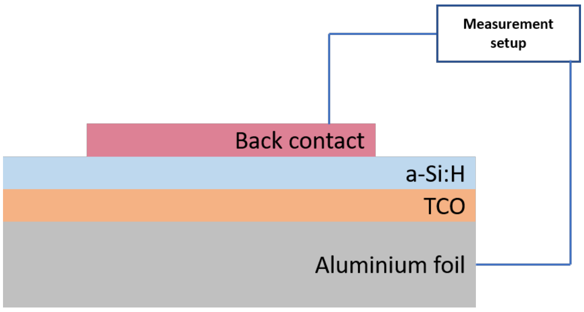

Figure 5.9: Schematic representation of Approach 1 SuperCoF after sputtering

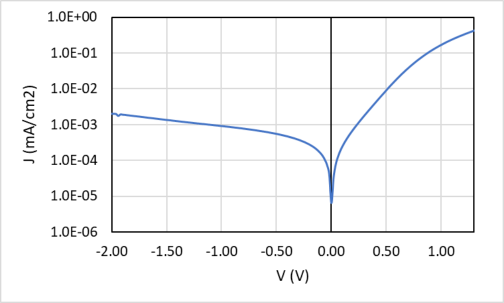

Figure 5.10: Dark JV measurements for Approach 1 SuperCoF after sputtering

The final design for the back contact area sputtered for this Approach is shown in the Figure 5.11.

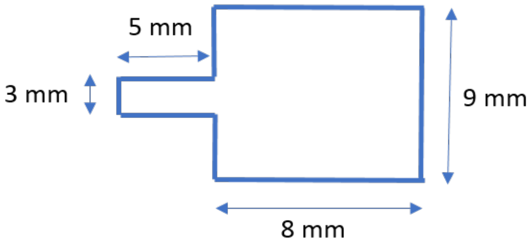

Figure 5.11: Back contact shape sputtered for SuperCoF for Approach 1

**Step 2**

The second step consists of placing the copper tape on the finger developed on the back contact. The

10x10 cm stack is divided into two parts to ensure all the cells can be connected using the copper tape. A plastic interleaf is placed under the copper tape to prevent copper tape from touching the Al foil. This is done to prevent short circuiting. The carrier foil is then laminated using a certain recipe of epoxy components. Since, the copper tape has thickness of around 80 microns, the lamination process needs precise application of the glue. If the glue is not used in appropriate quantity then the air bubbles can be formed in the lamination process which can decrease the shunt resistance. Moreover, delamination can also occur which can destroy the solar cell during the etching process.

The solar cell was contacted for a dark JV measurement as shown in Figure 5.12. The results from the measurement are shown in Figure 5.13 where it can be seen that the shunt resistance decreases after the lamination process. This is due air bubbles in the lamination process affecting the shunt resistance.

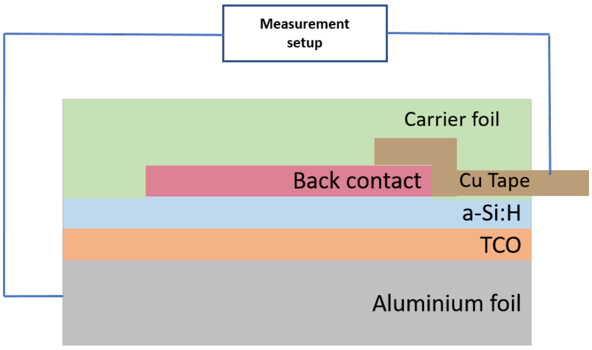

Figure 5.12: Schematic representation of Approach 1 SuperCoF after lamination

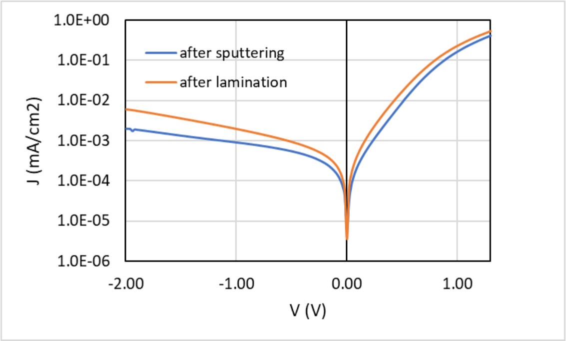

Figure 5.13: Dark JV measurements for Approach 1 SuperCoF after lamination

**Step 3**

After the cells are laminated, the next steps involves etching the solar cell to etch the Al foil. The Al foil after the first etch should have a thickness of 20 microns. The Figure 5.14 shows the SuperCoF stack after the first etching process. Similar to the previous steps a dark JV measurement was done. Figure 5.15 shows the results of the dark JV measurement after the first etch where the shunt resistance decreases marginally in comparison to after the lamination step.

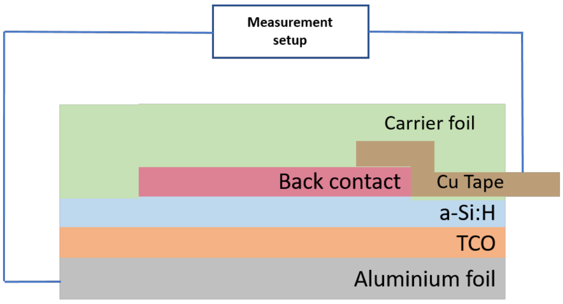

Figure 5.14: Schematic representation of Approach 1 SuperCoF after first etching process

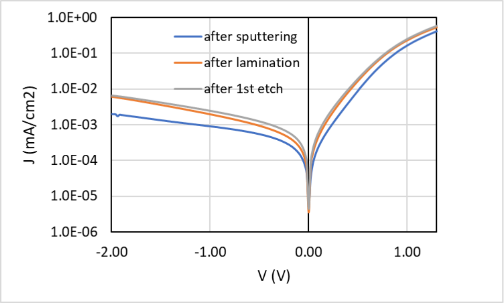

Figure 5.15: Dark JV measurements for Approach 1 SuperCoF after first etching process

**Step 4**

The annealing process is carried out next to remove residual stresses from the Al foil. The Figure 5.16 represents the dark JV measurement after the annealing process. Here, we don't see any affect on annealing on the shunt resistance of the SuperCoF.

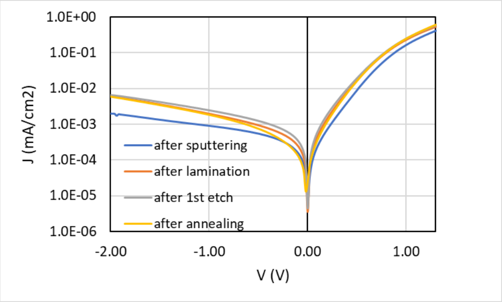

Figure 5.16: Dark JV measurements for Approach 1 SuperCoF after annealing process

**Step 5**

The final step in the SuperCoF process involves removing the last 20 microns from the Al foil to expose the active region of the solar cell. The active region is formed under the back contact area as shown in the Figure 5.17. Two busbars are left on the front side of the SuperCoF for contact. However, since the copper tape is thick, it can cause wrinkles after the etching process due to the shrinkage of copper tape. This can induce defects and affect the performance of the solar cell. Figure 5.18 shows the dark JV measurement after the final etch suggesting the cell survived the final etch and does not show a reduced performance.

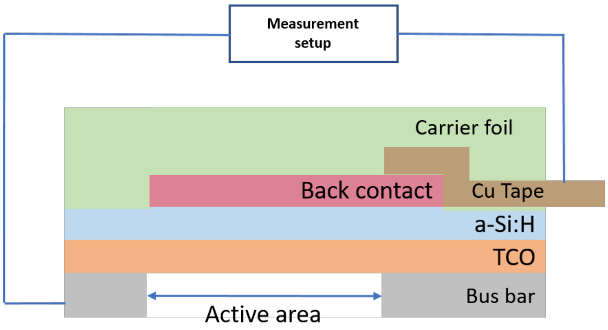

Figure 5.17: Schematic representation of Approach 1 SuperCoF after final etching process with the active region

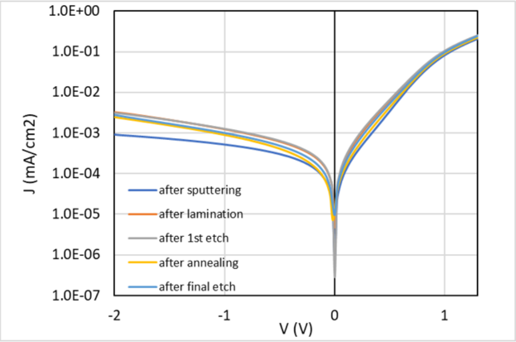

Figure 5.18: Dark JV measurements for Approach 1 SuperCoF after final etching process

## 5.3 Approach 2

The second approach for the SuperCoF processing involved **”Partial lamination and direct placement of probes on back contact”**. The following section discusses the Approach 2 process briefly.

**Step 1**

The sputtering process follows similar steps as discussed in the previous sections. The masks developed for this concept initially involved sputtering back contact in the shape as shown in Figure 5.21. Two fingers were included in the design to contact the probes for the measurement. To avoid losses in the solar cell, thin fingers were sputtered as shown in the figure. A total area of 5.6 cm$^2$ of back contact is sputtered. The Figure 5.20 shows the dark JV measurement for the cell after sputtering. Here, it can be observed that the shunt resistance is lower in comparison to Approach 1 which can be attributed to the fact that a larger area can cause more leakage current.

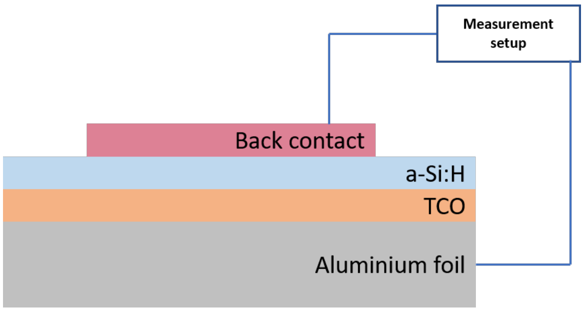

Figure 5.19: Schematic representation of Approach 2 SuperCoF after sputtering

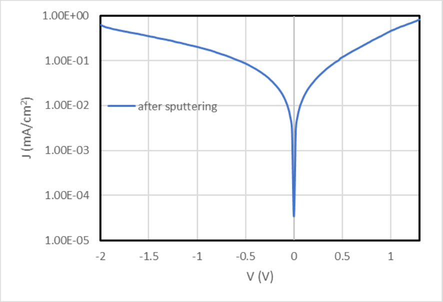

Figure 5.20: Dark JV measurements for Approach 1 SuperCoF after sputtering

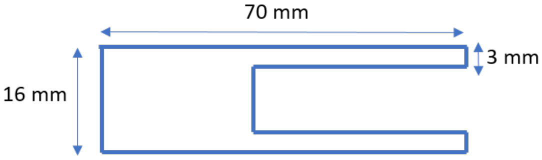

Figure 5.21: Back contact shape sputtered for SuperCoF for Approach 2

**Step 2**

The lamination strategy for this approach is more complicated since the direct contact on the back contact area requires the solar cell to be open to the atmosphere. Figure 5.22 shows the schematic diagram for the solar cell stack for Approach 2 which consists of half lamination across the back contact area. The remaining half of the cell is covered with an etching tape before the lamination process. Since, the lamination process uses high pressure and force, the etching tape acts a psuedo carrier foil during the etching process. This is essential as the etchant should not attack the solar cell area which is usually protected by the carrier foil. Figure 5.23 shows the dark JV measurement suggesting improved shunt resistance which can due to the fact the solar cell area is directly pressed under the thin etching tape.

Furthermore, as seen in Figure 5.22 to get the dark JV measurement, the etching tapes need to be cut. This creates a problem as the etchant can attack the back contact through the cut off area. This is seen as a major drawback of this approach since step by step measurement of shunt resistance at each process gives valuable feedback on the processing of the solar cell in the lab route.

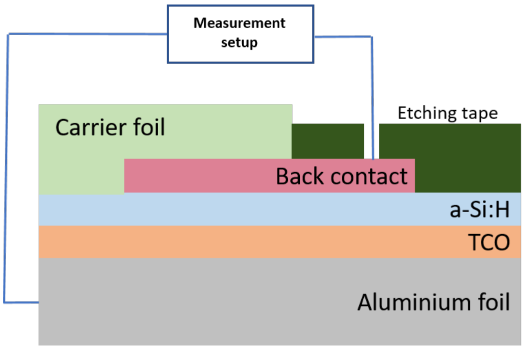

Figure 5.22: Schematic representation of Approach 2 SuperCoF after lamination

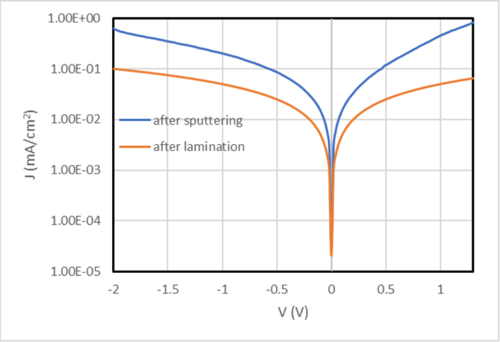

Figure 5.23: Dark JV measurements for Approach 1 SuperCoF after lamination

**Step 3**

As already discussed in the previous step the etchant can attack the back contact area. Hence an etching tape was used to cover the back contact area during the lamination. These steps make the approach a bit complex as any problems during the delamination can result in etching of the back contact. Since there is no lamination foil under half area of the cell, only one half of the stack is etched. The remaining half is covered with the etching tape. Figure 5.25 represents the dark JV curve after the first etch process. Here, it can be observed the shunt resistance remains almost the same after the process.

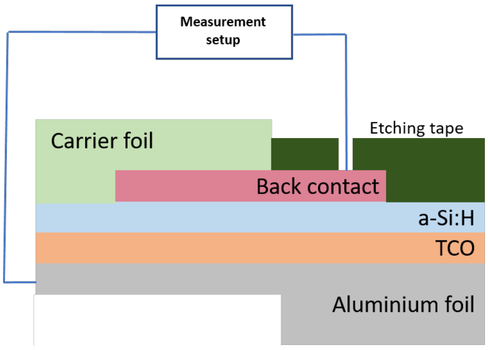

Figure 5.24: Schematic representation of Approach 2 SuperCoF after first etching process

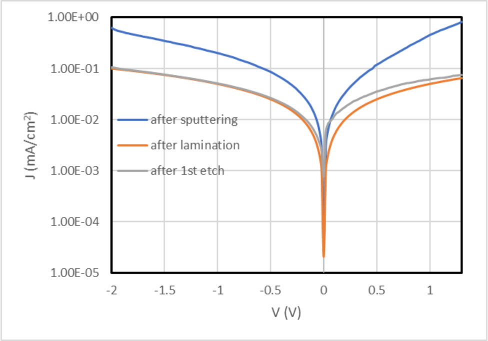

Figure 5.25: Dark JV measurements for Approach 2 SuperCoF after first etching process

**Step 4**

The annealing process is carried out similarly to the process discussed in the previous sections. The figure 5.26 represents the dark JV curve after the annealing process. Here the shunt resistance is observed to be improved after the annealing process quite significantly. However, this is not a true representation of the measurement and can be due to excessive force used in contacting during the measurement.

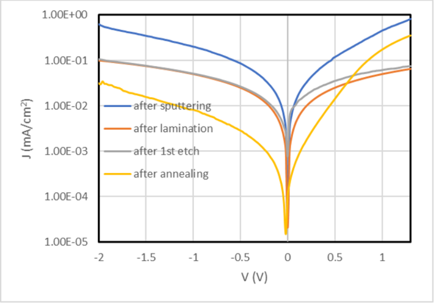

Figure 5.26: Dark JV measurements for Approach 2 SuperCoF after annealing process

**Step 5**

The final etching process involves exposing the active area of 1 cm$^2$ by covering the remaining part of the solar stack with an etch resistant tape. The bus bar is exposed after the etching process which can be used to contact the probes for JV measurement. The other probe can be placed directly on the back contact. During the etching process the etching tape placed on the back contact is kept, however after the etching process, the etching tape can be removed. This process is not so straightforward since the removal of the tape can remove the back contact as well. Hence, this leads to another drawback of this approach. Finally, the Figure 5.28 represents the dark JV measurement done after the final etching process suggesting an increase in the shunt resistance.

## 5.4 Comparison of the SuperCoF approaches

The pros and cons of two approaches were compared to understand the better approach for the fabrication of SuperCoF. The main objective of SuperCoF was to improve the learning cycles of the silicon deposition by eliminating the laser scribing process used in the lab sample fabrication. Although, this objective is fulfilled by both approaches, however, Approach 1 is advantageous over the Approach 2

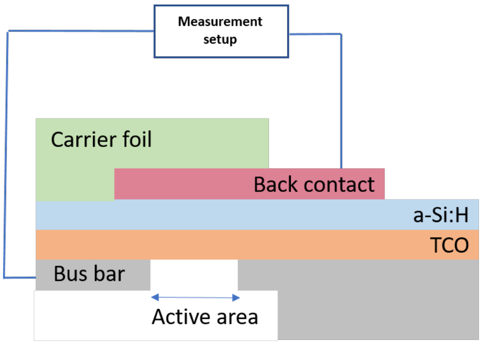

Figure 5.27: Schematic representation of Approach 2 SuperCoF after final etching process with the active region

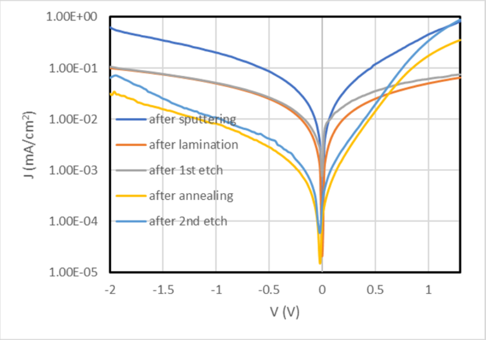

Figure 5.28: Dark JV measurements for Approach 2 SuperCoF after final etching process

sue to the ease of measuring the dark JV step by step. The Approach 2 can measure the dark JV at each step but involves a complex process of cutting through the etching tape which can result in damaging the solar cell while etching. Moreover, the Approach 2 leaves the back contact exposed to the atmosphere which can effect the performance of the cell by introducing defects. Furthermore, the Approach 2 requires a lot of etching tape which creates a problem of wastage.

On the other hand, the advantage of Approach 2 is the speed of the process, since the copper taping is a tedious process. Multiple cells can be laminated simultaneously. Moreover, the active area is well defined under the Approach 2 which in comparison to Approach 1 requires manual positioning of the tapes to define the active area. Despite these advantages, Approach 2 turns out to be more complex process than Approach 1. Moreover, Approach 1 can produce 20 cells per 10x10 cm substrate which enable good statistics and faster learning cycles. Based on the points discussed the final approach for the SuperCoF fabrication was Approach 1. All the results concerning the SuperCoF fabrication discussed further in this work will be based on the Approach 1.

## 5.5 SuperCoF approach - Processing of Triple junctions solar cells

The Approach 1 developed for the fabrication of lab samples was used to process triple junction based on amorphous silicon/microcrystalline silicon/ microcrystalline silicon solar cell. The deposition of the TCO was done on Flam01 texturing on Al foil at HyET Solar. The Flam01 texturing ensures enhanced reflection in the solar cell which promotes the current densities. The triple junction thickness are mentioned in the Figure 5.29. The thickness are based on current matching for all the cells. The bottom cell is the current limiting one in this configuration. All the layers except the back contact are deposited in TU Delft.

Two series of triple junction based on different back contact stacks were processed. The first series was with the traditional AZO/Al back contact, while the second series was deposited using silver (Ag) based ZAZAl configuration. The ZAZAl configuration consists of AZO/Ag/AZO/Al layers.

### 5.5.1 AZO/Al back contact

The first series of triple junction had 70 nm of AZO and 300 nm of Al for the back contact. The samples processed as SuperCoF with **Approach 1** faced various issues while processing. The samples had problems with lamination as the thickness of copper tape interferes with the lamination process. The process require certain amount of glue to overcome the copper tape thickness. If the glue quantity is not appropriate then the carrier foil might not get laminated properly which can create problems during etching. Figure 5.30 and 5.31 shows a typical front side and back side respectively of bad processing of the triple junction SuperCoF due to lamination issues.

A second batch of SuperCoF for triple junctions were processed with improved lab line processes. This time the delamination problems were addressed with using adequate quantities of the epoxy com-

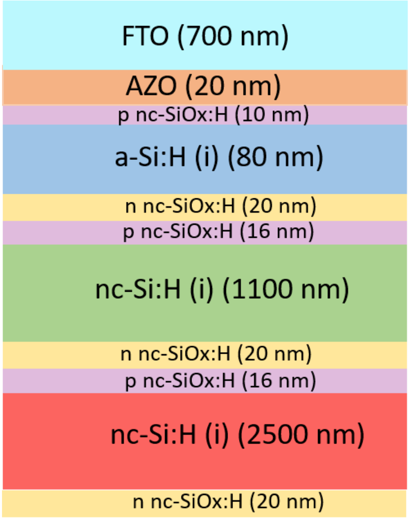

Figure 5.29: Triple junction stack used for processing to SuperCoF deposited at TU Delft

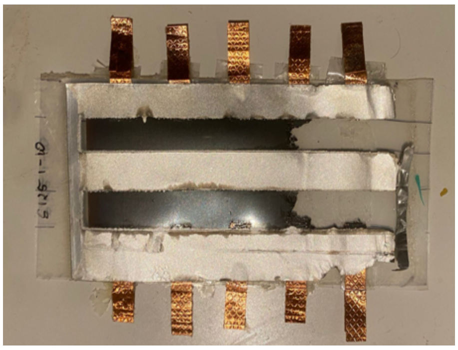

Figure 5.30: SuperCoF front side damaged due to delamination

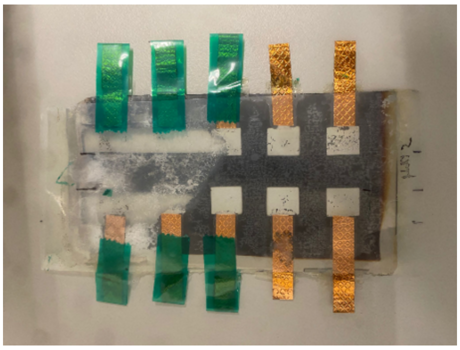

Figure 5.31: SuperCoF back side damaged due to delamination

ponents. However, even with improved lamination process the yield of the samples was still quite low. This was attributed to the problems in the etching line where the thermocouple was malfunctioning resulting in a lower temperature of the base. Another reason for the shunting of the solar cells could be due to the fact that the top cell processed in the triple junction series is too thin. This could create shunting across the top cell, generating only the response of the middle and the bottom cell. The final samples from SuperCoF are shown in the Figure 5.32 and 5.33.

### 5.5.2 ZAZAl back contact

The second series comprised of the ZAZAl back contact which has 70 nm of AZO, 400 nm of Ag, 70 nm of AZO and 300 nm of Al. The Ag is expected to be a better reflector than Al and hence would help to enhance the current densities in the bottom cell. This is especially important as the bottom cell is the current limiting. A TCO layer is provided in between Ag and Al to prevent diffusion of Al into the Ag layer. Finally, the Al layer ensures that the carrier foil can be laminated.

### 5.5.3 Results

The JV parameters from the Wacom measurement done in TU Delft are plotted in the Figure 5.35, 5.36 and 5.34. The figures compare the V$_{oc}$, FF and J$_{sc}$ for back contacts with AZO/Al and ZAZAl. The series resistance observed for the back contact with ZAZAl was lower which can be attributed to

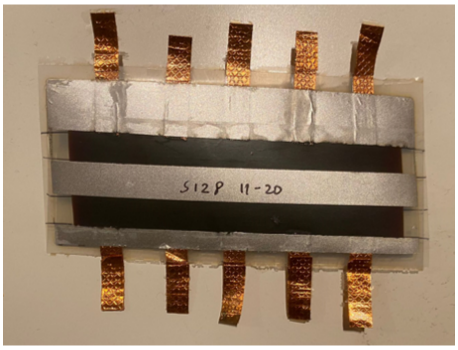

Figure 5.32: Final SuperCoF front side

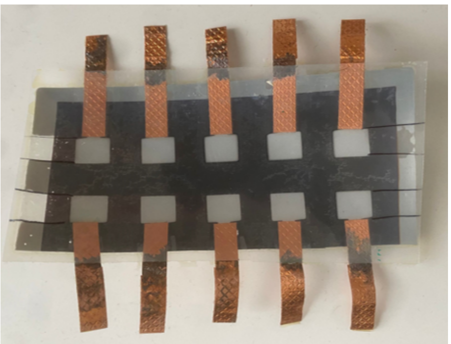

Figure 5.33: Final SuperCoF back side

lower sheet resistance of Ag. Furthermore, the J$_{sc}$ was seen to be improving with the silver based back contact due to more reflection in the solar cell. The J$_{ph}$ for the bottom cell can be improved with a silver back contact. This improves the J$_{sc}$ as the bottom cell is the current limiting one.

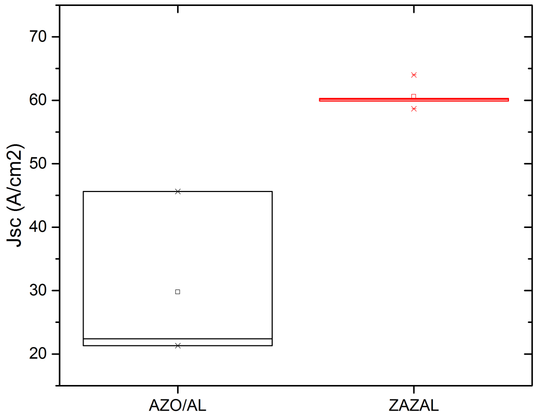

Figure 5.34: Comparison of the J$_{sc}$ of AZO/AL and ZAZAl series

However, the J$_{ph}$ enhancement in the solar cell is subjected to the current matching condition. The current matching for the triple junction is done with Al as the back reflector. Hence, because of the mismatched currents we find a lower V$_{oc}$ values in the ZAZAl configuration. This can be justified by the fact that open circuit voltage directly depends on the ratio of J$_{ph}$ and J$_0$ on a logarithmic scale. Therefore, if the J$_{ph}$ are not matched then the expected V$_{oc}$ are smaller as observed in the case of ZAZAl. The lower FF can be attributed to the fact that V$_{oc}$ and J$_{sc}$ differ from each other.

To conclude, the triple junctions processed as SuperCoF showed preliminary results. These were the first stack of triple junctions processed on Al substrate. However, still the process of processing triple junctions for SuperCoF needs to be optimized as there was low yield.

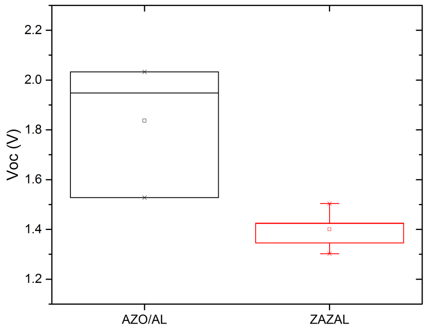

Figure 5.35: Comparison of the V$_{oc}$ of AZO/AL and ZAZAl series

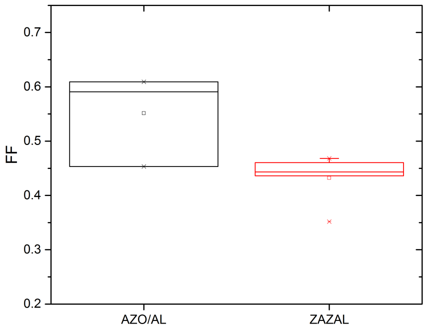

Figure 5.36: Comparison of the FF of AZO/AL and ZAZAl series

## 5.6 Conclusion

Overall, the problem of bottleneck in the lab processing has been solved with the implementation of the SuperCoF. Two approaches were developed for the processing which can yield cells without laser scribing. The approach with contacting the back contact with the copper tape is selected as the final procedure. Although, this approach is tedious but it provides the dark JV measurement step-by-step which can help in improving the lab processing. Overall, the SuperCoF is now the new work horse for HyET Solar which can provide faster learning cycles and better feedback on the silicon layers. The process is currently being used in HyET Solar regularly for fabricating the tandem solar cells. Furthermore, two batches of triple junctions with different back contacts were processed. However, the low yield in the results were attributed to problems in the lab processing line.

# Chapter 6

# Optimization of the PECVD tool at HyET Solar

The PECVD tool at HyET Solar is used to deposit the tandem solar cell in a micromorph configuration. The top cell recipe is standardized at HyET Solar. However, the bottom cell deposition based on the nanocrystalline silicon needed to be optimized. Hence, a series of experiments were conducted to ensure the optimum growth of microcrystalline silicon. This chapter will focus on the analysis of the micromorph cell on the HyET substrate.

## 6.1 Background

The PECVD tool at HyET Solar as discussed in Section 3.1.3 consists of various zones. The zones are used with different Silane dilution ratios to deposit amorphous and nanocrystalline materials. However, the recent micromorph solar cell depositions were not successful and the material was considered to be too amorphous. The ASA (advance semiconductor analysis) software was used to simulate a nanocrystalline silicon single junction solar cell with the different layers as shown in the Figure 6.1. The intrinsic layer which consists of 2000 nm of nc-Si:H was modified to different case studies. Firstly, the base case with 2000 nm of nc-Si:H was simulated. This case would act as the reference case for the study. The different cases simulated is based on the presence of different zones in the PECVD tool at HyET Solar. However, in this study for the ease simulation instead of micromorph stack a single junction nc-Si:H is used.

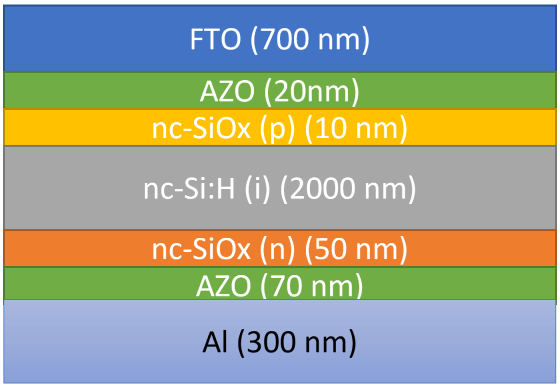

Figure 6.1: Base case stack of the single junction solar cell based on nanocrystalline silicon intrinsic layer]

To demonstrate the performance of the nc-Si:H based solar cell on a realistic condition, Flam01 texturing was used in the ASA model. The modulated surface texturing (MST) Flam01 morphology at TU Delft provides two functions: enhancement of the light trapping and promoting the microcrystalline growth. The Flam01 texturing simulated in GenPro4 is shown in Figure 6.2. Here the surface features are characterized by microtextures with smooth U shape. A smooth texturing helps to enhance efficient light trapping in the longer wavelengths of the red/infrared region of the spectrum. For reaching higher depositions rates for nanocrystalline silicon Flam01 is useful as it helps to provide a defect free deposition. Finally, the efficient light trapping due to Flam01 helps to promote the short circuit current densities without affecting the FF and V$_{oc}$.

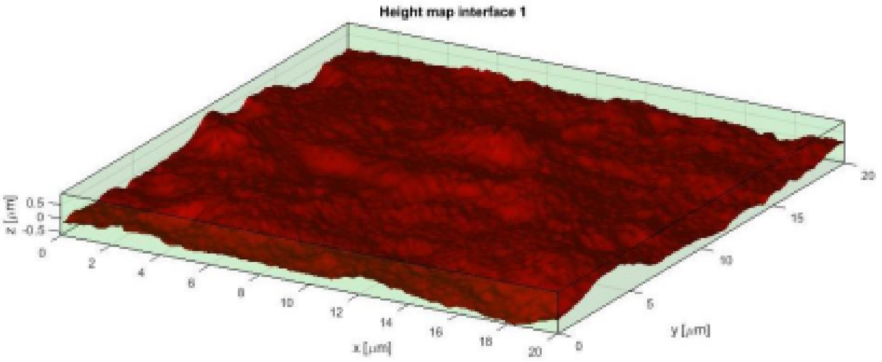

Figure 6.2: 3D representation of Flam01 texturing simulated in GenPro4

The band diagram for the base case with 2000 nm of nanocrystalline material is shown in the Figure 6.3. Here the Evac is vacuum energy level about which the other bandgaps are aligned. Ec and Ev are the conduction and the valence band edge energy levels. The slope in the band edges suggest a presence of electric field. Efn and Efp are the fermi levels of the n-doped and the p-doped layers which shift according to the doping concentration. The activation energy of the acceptor layer is taken to be 0.2 while the activation energy for the donor layer is taken to be 0.1 for all the cases.

For the base case the JV parameters calculated were as follows; V$_{oc}$ = 0.56, J$_{sc}$ = 23.4 and FF = 0.71. This is typically what is expected from a nanocrystalline silicon based solar cell. The higher current densities are due to efficient light trapping due to Flam01 texturing. Moreover, the V$_{oc}$ of nc-Si:H is in the typical range of 0.5 V as expected. Hence, the reference model developed seems to show the expected results. Furthermore, it can be observed from the Figure 6.3 that a smooth conduction and valence band is observed for nc-Si:H with a bandgap of around 1.1 ev. Figure 6.4 show the photogenerated carriers for i-nc-Si:H on a logarithmic scale against the position in the solar cell. It is observed that the photogenerated carriers follow a smooth curve with a peak observed in the initial part of the intrinsic layer.

The absorption profile in simulation is calculated using the Lambert Beer absorption formula which explains the impact of absorption coefficient $\alpha(\lambda)$ on photon flux density after passing a certain distance in the film as shown in Eq 6.1. Here, $\Phi^0(\lambda)$ is the incident photon flux density.

$$\Phi(x,\lambda) = \Phi^0(\lambda)\exp(-\alpha(\lambda)x) \tag{6.1}$$

The spectral generation rate $g_{sp}$ explains the number of electron hole pairs generated at a certain depth x in the film per second per unit volume per unit is wavelength is calculated using the Eq 6.2. Here $\eta_g$ is the generation quantum efficiency.

$$g_{sp}(x,\lambda) = \eta_g \Phi^0(\lambda)\alpha(\lambda)e^{-\alpha(\lambda)x} \tag{6.2}$$

Finally, the optical generation rate $G_{\text{opt}}(x)$ is calculated from the spectral generation rate by integrating over the desired wavelength spectrum as shown in Eq 6.3.

$$G_{\text{opt}}(x) = \int_{\lambda_1}^{\lambda_2} g_{\text{sp}}(x,\lambda)d\lambda \tag{6.3}$$

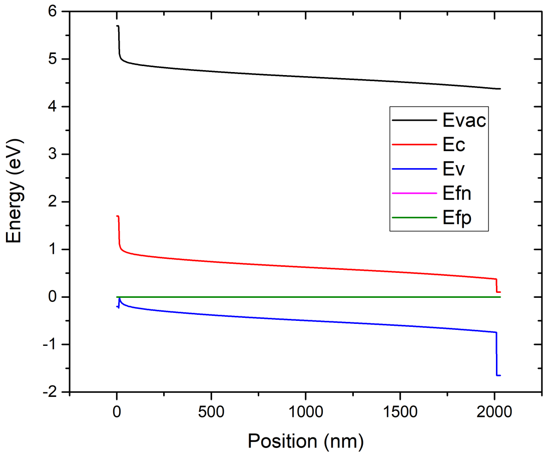

Figure 6.3: Band diagram for single junction nanocrystalline silicon solar cell (Base Case)

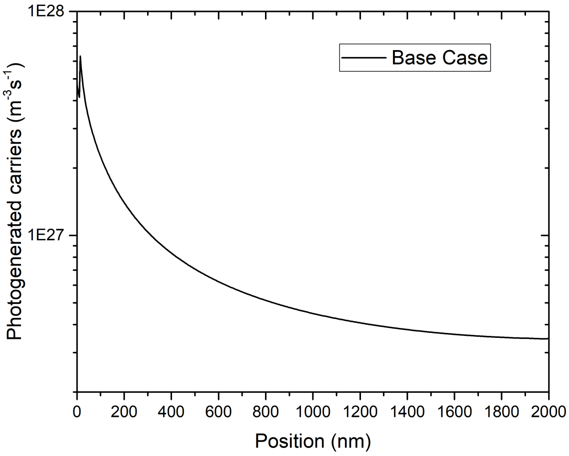

Figure 6.4: Photogenerated carriers for single junction nanocrystalline silicon solar cell (Base Case)

Moreover, the Figure 6.5 shows the total recombination occurring inside the absorber layer for the base case. It can be observed that the recombination at the p doped and the n doped side of the cell is more in comparison to the intrinsic layer due to presence of the dopants.

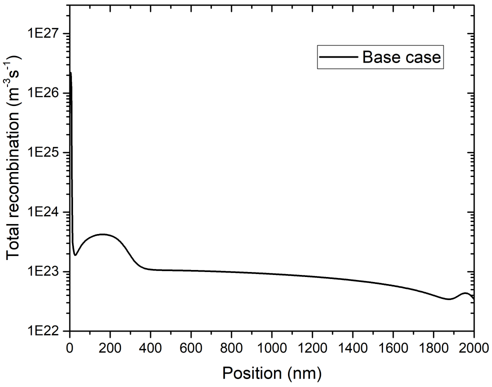

Figure 6.5: Total recombination occurring in the intrinsic layer for the base case

The different cases used for this study are shown in the Table 6.1. Here each layer represents a thickness of 650 nm. The base case is the reference case with 2000 nm of intrinsic layer thickness. Case 1, Case 2 and Case 3 is simulated to understand the effect of amorphous material in a nanocrystalline material layer. While Case 4, Case 5 and Case 6 are made to understand the effect of nanocrystalline layer in a amorphous material.

| | ***Base case*** | ***Case 1*** | ***Case 2*** | ***Case 3*** | ***Case 4*** | ***Case 5*** | ***Case 6*** |
|---|---|---|---|---|---|---|---|
| Layer 1 | nc-Si:H | a-Si:H | nc-Si:H | nc-Si:H | a-Si:H | a-Si:H | nc-Si:H |
| Layer 2 | nc-Si:H | nc-Si:H | a-Si:H | nc-Si:H | a-Si:H | nc-Si:H | a-Si:H |
| Layer 3 | nc-Si:H | nc-Si:H | nc-Si:H | a-Si:H | nc-Si:H | a-Si:H | a-Si:H |

Table 6.1: Different cell configurations for the ASA study

### 6.1.1 Case 1

The first simulation done for Case 1 is based on introducing nc-Si:H material growth on a-Si:H layer. This means the first layer to be deposited is amorphous while the subsequent layers growing on top of the amorphous layer would be nanocrystalline silicon. The band diagram for the Case 1 is shown in Figure 6.6. Here, a barrier in the valence band can be seen at position after 650 nm which is due to a presence of nc-Si:H based material. Since, the bandgaps for a-Si:H and nc-Si:H are different a barrier is observed. This prevents the movement of the holes across the conduction band in the positions higher than 650 nm.

This effect of barrier as discussed can be seen in the performance of the solar cell in terms of the JV parameters as shown in Table 6.2. The lower short current densities observed in the case is typical that for amorphous silicon based solar cells. This suggests that even though we have nanocrystalline material in the stack, the amorphous material acts as barrier to the nc-Si:H, absorbing all the light in the initial thickness. Hence, the deposition of a-Si:H layer dominates the solar cell performance regardless of the fact that there is 1300 nm of nc-Si:H. The V$_{ov}$ observed is also similar to the V$_{oc}$ of a a-Si:H solar cell. Therefore, the first layer deposition in the nanocrystalline silicon solar cell becomes the base layer for the further growth of material influencing the properties of the solar cell. Finally, the Figure 6.7 represents the photogenerated carriers against the position in the absorber layer. Here, we can see an increase in the photogenerated carriers at a position of 660 nm which is due to nc-Si:H material in the intrinsic layers. However, these photogenerated carreirs are not collected due to the barrier as shown in Figure 6.6.

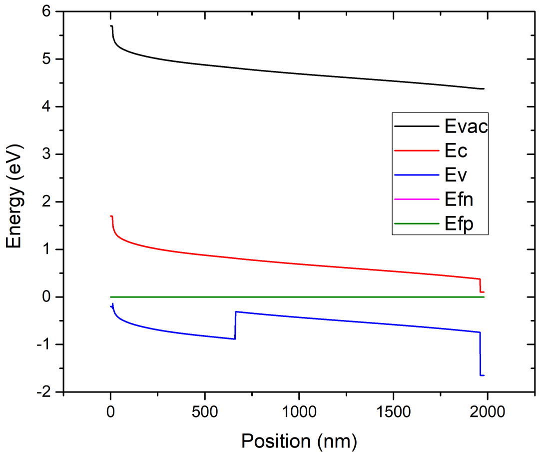

Figure 6.6: Band diagram for Case 1

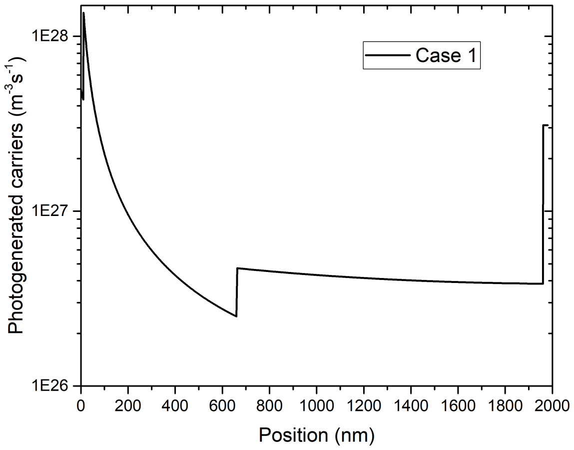

Figure 6.7: Photogenerated carriers for Case 1

### 6.1.2 Case 2

For the Case 2, the first growth layer was nc-Si:H followed by a-Si:H and the final layer as nc-Si:H. The band diagram for the Case 2 is shown in the Figure 6.8 suggesting the last nc-Si:H layer to be not contributing to the V$_{oc}$, as the a-Si:H barrier is of higher bandgap than that of nc-Si:H. This would prevent the hole transfer across the valence band from the last nc-Si:H layer. Furthermore, in the Figure 6.9 the photogenerated carriers are shown where the a-Si:H material seems to be contributing to the charge generation. However, the layer after the a-Si:H layer does not have any collection of charge generated.

The JV parameters as shown in the Table 6.2 suggest that the increase in the current from Case 1 is due to presence of a-Si:H after 650 nm. The Case 2 can provide higher current due to the presence of an a-Si:H layer, however, since the thickness of the nc-Si:H is not thick enough we do not reach the current densities of the base case.

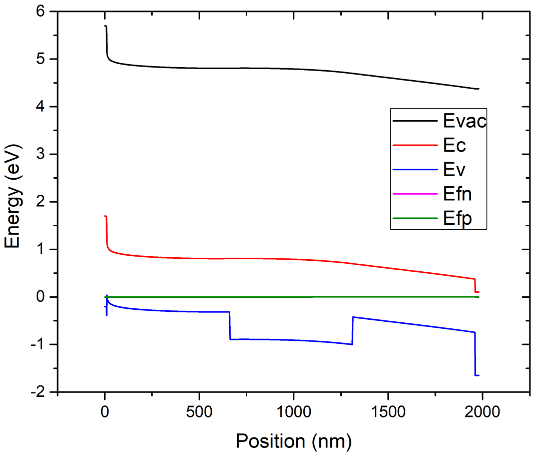

Figure 6.8: Band diagram for Case 2

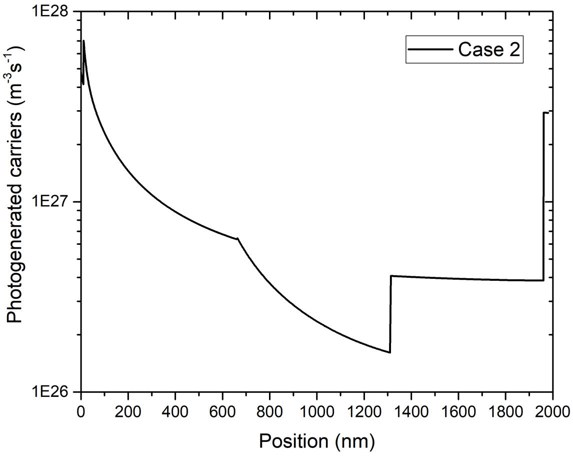

Figure 6.9: Photogenerated carriers for Case 2

The total recombination occurring in the intrinsic layer for the Case 2 is shown in Figure 6.10. Here it can be seen that till 650 nm of thickness, the total recombination follows the same trend as the total recombination in the base case. However, when we go to amorphous layer the total recombination increases. The total recombination increases even further after the introduction of the nc-Si:H layer. This suggests that the photogenerated carriers in the last layer are all recombined.

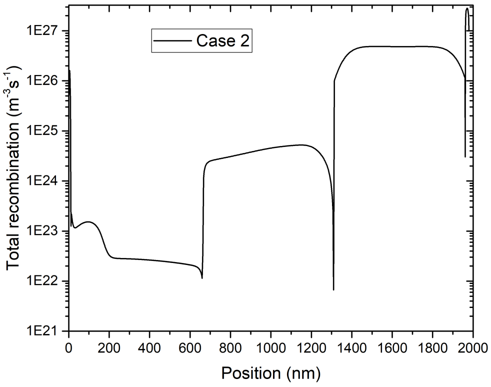

Figure 6.10: Total recombination occurring in the intrinsic layer for the Case 2

### 6.1.3 Case 3

The Case 3 simulated nc-Si:H/nc-Si:H/a-Si:H case where the barrier is after 1300 nm in the cell as seen from the Figure 6.11. The material in this configuration is seen to be acting like that with nanocrystalline silicon solar cell. The current densities observed are higher than that of the other cases due to the presence of a thicker nc-Si:H layer before the introduction of the a-Si:H layer.

The higher the amount of nanocrystalline structure without any interference from the amorphous material results in better performance of the solar cell similar to the base case as shown in the Figure 6.12. We get a $J_{sc}$ of 21.8 mA/cm$^2$ which is the highest observed for all the case studies. The base case was at 23.4 mA/cm$^2$ and 0.56 V. The $V_{oc}$ observed for the Case 3 is very similar to the base case suggesting the dominance of the nanocrystalline material in the configuration. This suggests that a presence of amorphous material in the stack does not influence the performance drastically if the growth layers are nanocrystalline. Hence, the sensitivity of the growth of the nanocrystalline silicon solar cell in the PECVD tool can be understood.

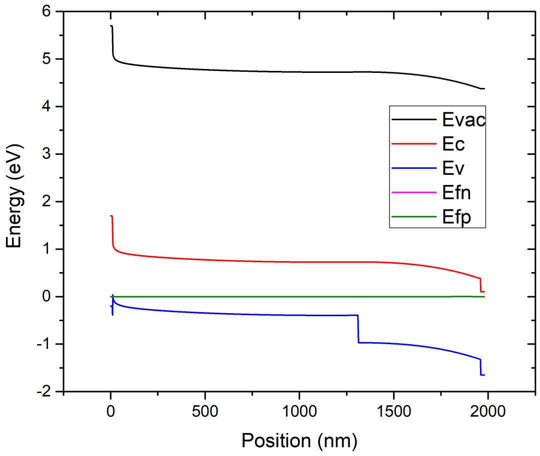

Figure 6.11: Band diagram for Case 3

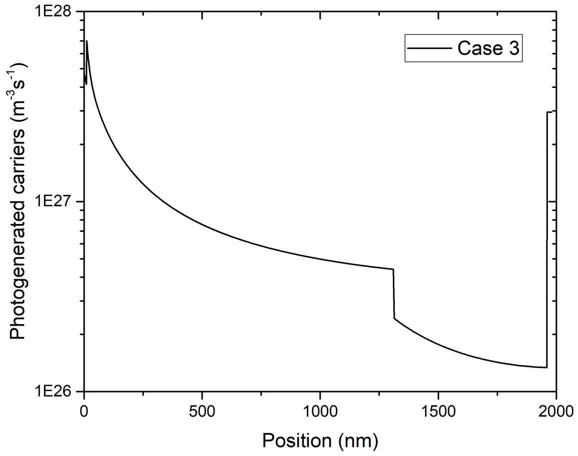

Figure 6.12: Photogenerated carriers for Case 3

## 6.1.4 Case 4

The Case 4 simulates configuration with higher amorphous material. The stack used for the simulation is a-Si:H/a-Si:H/nc-Si:H. The nc-Si:H layer is grown on a a-Si:H layer resulting in a decreased J$_{sc}$ as seen from the Table 6.2. The solar cell has a J$_{sc}$ and V$_{oc}$ very similar to that of a a-Si:H solar cell. The nc-Si:H layer does not seem to influence the performance of the solar cell. This trend can be understood from the Figure 6.13 which shows the barrier for the holes at around 1300 nm. This barrier prevents the transfer of holes across the valence band and hence prevent any influence of nc-Si:H on the solar cell performance. Furthermore, the Figure 6.14 shows that the photocurrent generation is happening till 1300 nm after which the nc-Si:H is not contributing to the carrier generation.

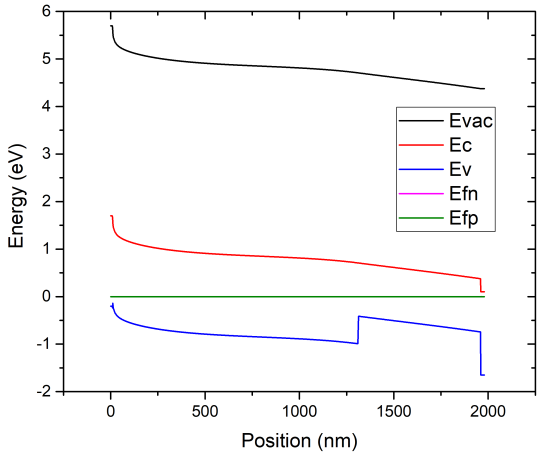

Figure 6.13: Band diagram for Case 4

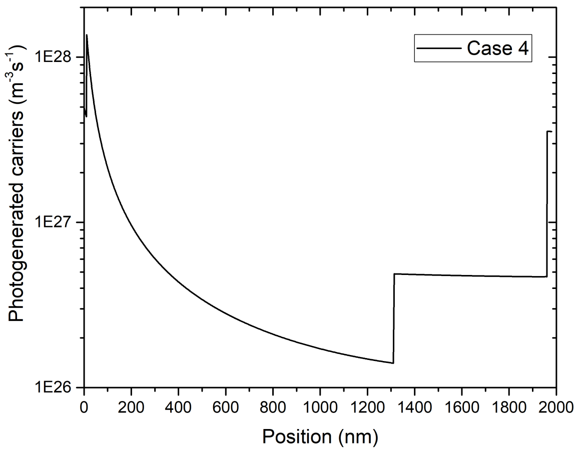

Figure 6.14: Photogenerated carriers for Case 4

## 6.1.5 Case 5

This case shows the effect of a nc-Si:H layer sandwiched between two a-Si:H layers. From the Figure 6.15 it can be seen that nc-Si:H material with the lower bandgap is placed in between two layers of a-Si:H material which has a higher band gap. The lower bandgap of nc-Si:H does not influence any properties of the solar cell and material acts as a a-Si:H. This can also been seen from the JV parameters which suggest a V$_{oc}$ of 0.91 V which is typical for amorphous silicon based single junction solar cells. Furthermore, from the Figure 6.16 it can be seen that the a-Si:H after the 650 nm does not contribute in the carrier generation. The effect of this can be understood from the J$_{sc}$ which is 13.1 mA/cm$^2$ for Case 5. This is 0.8 mA/cm$^2$ less than Case 4, showing that after a certain thickness of a-Si:H, the performance of the solar cell does not increase significantly.

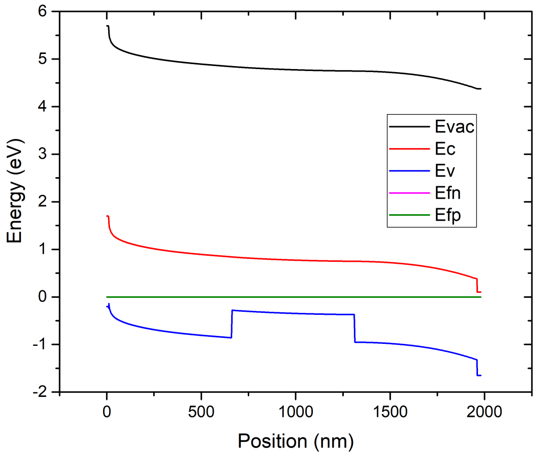

Figure 6.15: Band diagram for Case 5

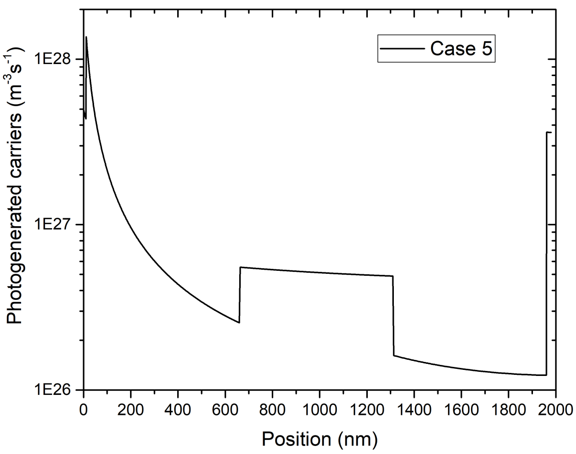

Figure 6.16: Photogenerated carriers for Case 5

### 6.1.6 Case 6

The final case in the simulation study included growing amorphous material on top of nanocrystalline material. The nc-Si:H first layer increases the J$_{sc}$ as more light can be absorbed in the first layer of the stack. The barrier for the holes in the valence band is shown in 6.17 where at 650 nm the a-Si:H material seems to be present with a larger bandgap. However, since the first layer of the stack was nanocrystalline based we can see that the amorphous material does not influence the J$_{sc}$ and the V$_{oc}$. Although, the J$_{sc}$ was still lower than that of a typical nc-Si:H cell. Hence, suggesting the first layer growth for a nanocrystalline material is critical.

### 6.1.7 Simulation results

The final JV parameters and the EQE results are from the simulation cases is discussed in the following section. Based on the results obtained, the nc-Si:H can be said to be a very sensitive material which can be influenced easily by the presence of a-Si:H material. Even a small thickness of a-Si:H can influence the solar cell parameters of the nc-Si:H as seen from the Table 6.2.

| | *Voc (V)* | *Jsc (mA/cm2)* | *FF* |
|---|---|---|---|
| **Base case** | 0.56 | 23.4 | 0.71 |
| **Case 1** | 0.91 | 13.1 | 0.72 |
| **Case 2** | 0.60 | 17.4 | 0.70 |
| **Case 3** | 0.58 | 21.8 | 0.70 |
| **Case 4** | 0.91 | 13.9 | 0.69 |
| **Case 5** | 0.91 | 13.1 | 0.71 |
| **Case 6** | 0.60 | 18.5 | 0.70 |

Table 6.2: Results for the JV parameters for the ASA simulation for the different case studies

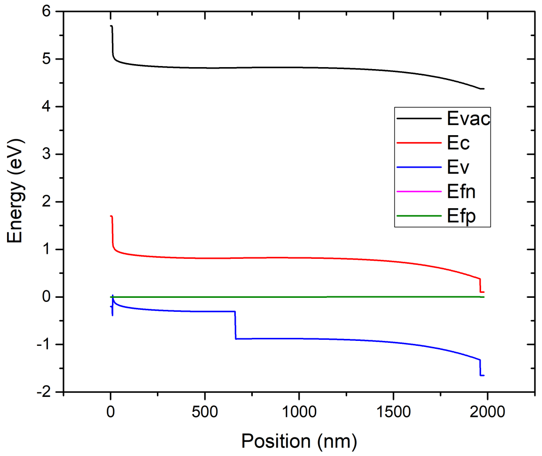

Figure 6.17: Band diagram for Case 6

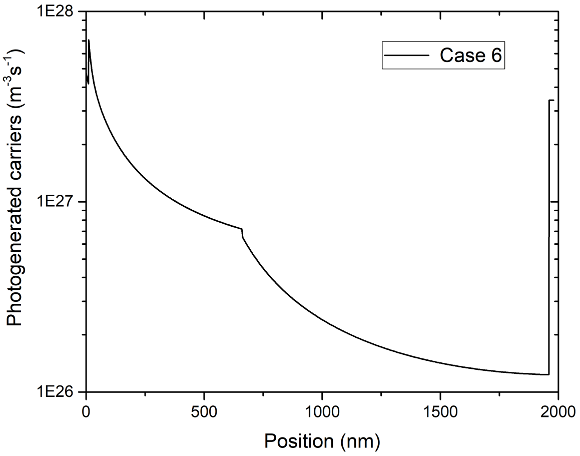

Figure 6.18: Photogenerated carriers for Case 6

The Figure 6.19 represents the EQE calculated from the ASA simulation for the various cases. Here, it can be seen that the Case 1, Case 4 and Case 5 behave exactly how a amorphous silicon solar cell behaves. These are the cases with the first growth layer consisting of a-Si:H. Furthermore, the Case 2, Case 3 and Case 6 show behaviour different from the a-Si:H, however, there could be low EQE values seen in the longer wavelength regions. This is due to the presence of a-Si:H layer reducing the thickness of the nc-Si:H layer and absorbing part of the solar spectrum. The case closest to the base case was Case 3 which is amorphous material grown on top of nanocrystalline material. To conclude, the results from the simulation study, the first layer growth in the nanocrysatlline silicon solar cell is critical. If the first layer deposited is too amorphous then the solar cell will act like amorphous silicon regardless of further depositions. The influence of a-Si:H in the middle is derogatory as a huge part of the EQE is lost leading to lower performance of the solar cell.

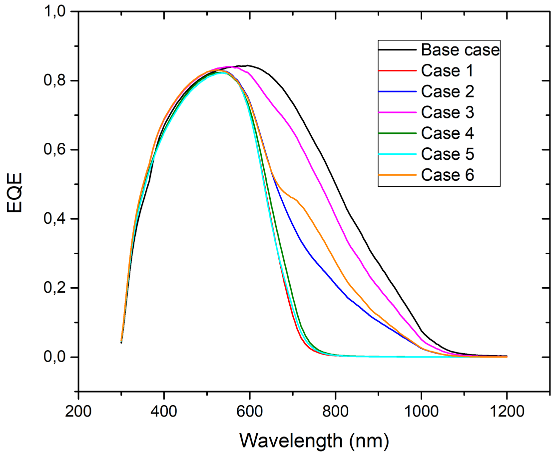

Figure 6.19: EQE results from the ASA simulation for the case studies

Furthermore, to understand the effect of a-Si:H layer at the end of the nc-Si:H deposition, a simulation with 400 nm of a-Si:H at the end of a 2000 nm nc-Si:H layer was carried out. The EQE results of the simulation are compared with the Base case which consists of 2000 nm of nc-Si:H layer. The Figure 6.20 shows the EQE comparison between the two cases. The results suggest that the 400 nm of additional a-Si:H at the end of the nanocrystalline intrinsic layer does not influence the EQE as the two curves almost overlap. Hence, we can conclude that the nc-Si:H deposition is not very sensitive to additional a-Si:H at the end of the desired nc-Si:H deposition. This can further help to mitigate future deposition problems in the PECVD tool at HyET Solar.

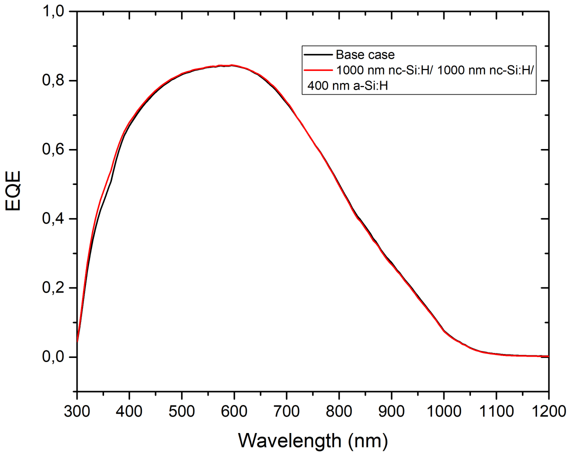

Figure 6.20: EQE results from the ASA simulation for the comparison between the Base case which is 2000 nm of nc-Si:H and the case with additional 400 nm of a-Si:H after the 2000 nm nc-Si:H intrinsic layers

## 6.2 Micromorph solar cell deposition at HyET solar

A series of experiments has been conducted at HyET Solar to deposit micromorph based solar cells in the R2R production process. The various production runs focused on developing a standard recipe for continuous production of micromorph solar cells in the HyET Solar production line. This work gives special emphasis to the latest tandem2production run based in the month of the August 2021. The main objective of the experiment was to deposit a good bottom cell based on microcrystalline silicon. Moreover, understanding a startup procedure for the bottom cell deposition so the quality of material deposited in each zone can be evaluated.

The different settings used for the bottom cell deposition in the August run are shown in the Table 6.3. Here 2 settings with different Silane flow rates and same Hydrogen flow rates are shown. Since, the PECVD tool has 5 zones for depositing the intrinsic layer various flow rates were used for different zones in the experiment. The Setting 1 uses high flow rate in Zone 3 and Zone 4 while lowering the flow rates in the consequent zones. The lower flow rates in the Zone 5, Zone 6 and Zone 7 produces lower silane dilution ratios. To understand the effect of higher silane dilution ratios in the Zone 5, Zone 6 and Zone 7, Setting 2 used higher Silane flow rates. This would give the comparison of different flow rates on the deposition of the nc-Si:H based bottom cell.

| ***Silane flows*** | ***Z3*** | ***Z4*** | ***Z5*** | ***Z6*** | ***Z7*** |
|---|---|---|---|---|---|
| **Setting 1** | High | High | Low | Low | Low |
| **Setting 2** | High | High | High | High | High |

Table 6.3: Different setting for the Silane flow used in August run for the production of tandem solar cell

### 6.2.1 Performance of the August run

The results from the August run experiment are presented in this section. The comparison between the Silane flow rates for the Zone 5, Zone 6 and Zone 7 is done by measuring the Illuminated JV and EQE measurement. SuperCoF processing methodology as discussed in Chapter 5 was used to process the solar cells.

Firstly, the results from the Illuminated JV measurement done at TU Delft are presented in the Figure 6.21 and 6.22. The figures compare the $V_{oc}$ and the FF for the two setting as discussed in Table 6.3. When comparing the $V_{oc}$ from the Figure 6.21 it can be seen that the higher dilution ratios of Setting 2 has lower $V_{oc}$ in comparison to Setting 1. Similar trends can be observed for FF where the lower Silane flows for Setting 1 provides better results. The average $V_{oc}$ observed for Setting 1 was 1.3 V and for Setting 2 was 1.2 V which is what is in the range of a typical micromorph solar cell. The FF for Setting 1 was on average 0.66 and the average FF for Setting 2 was about 0.60.

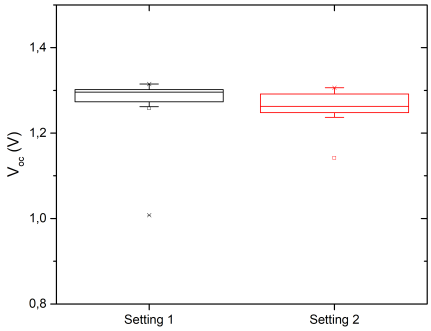

Figure 6.21: Comparison of $V_{oc}$ for different setting from August run

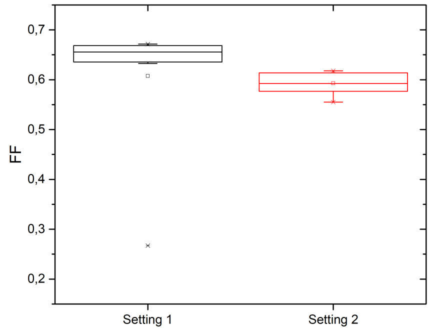

Figure 6.22: Comparison of FF for different setting from August run

The settings were measured on the EQE setup in TU Delft. the results from the EQE measurement are presented in Figure 6.23 and 6.24. The top cell measurements are shown in red which was prepared using the baseline recipe developed at HyET Solar. The top cell current observed from the EQE measurements was 9.45 mA/cm$^2$. However, the bottom cell current was observed to be lower than that of a typical micromorph cell. The bottom cell current densities measured with the EQE were 4.23 mA/cm$^2$ for Setting 1 and 4.88 mA/cm$^2$ for Setting 2.

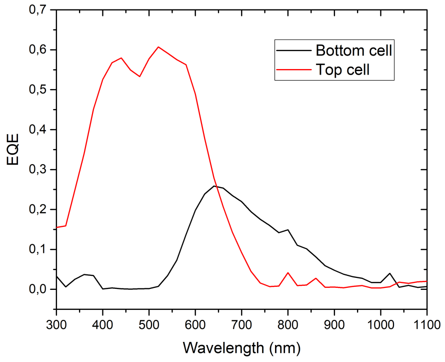

Figure 6.23: EQE for the tandem cell Setting 1

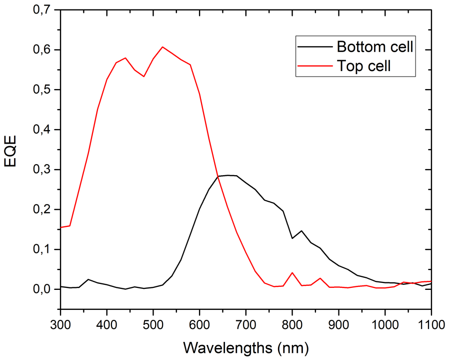

Figure 6.24: EQE for the tandem cell Setting 2

## 6.3 Continuous variable thickness (CVT) series

The continuous variable thickness (CVT) is a type of deposition condition used in the PECVD tool at HyET Solar. The Figure 6.25 represents a typical CVT deposition for the bottom cell. Here a stack of Al/FTO/AZO/Top cell is used to deposit the bottom cell with the varying thickness. Between the various

Position on Foil (PoF), the deposition can be stopped and started. The PoF A in the Figure 6.25 shows a position where the deposition under a certain Zone will start while PoF B depicts the position where the deposition under a zone ends. Since, the PECVD tool at HyET Solar consists of various zones, the CVT technique can be used to understand the deposition done under various zones. This deposition at certain PoF would represent a thickness which reaches the maximum at PoF B. Since, the CVT is on a R2R process, the stack produced under different zones will have underlying stacks having depositions from the previous zones as the roll progresses forward in the PECVD. Similar, to the bottom cell the top cell can be analyzed under the CVT series.

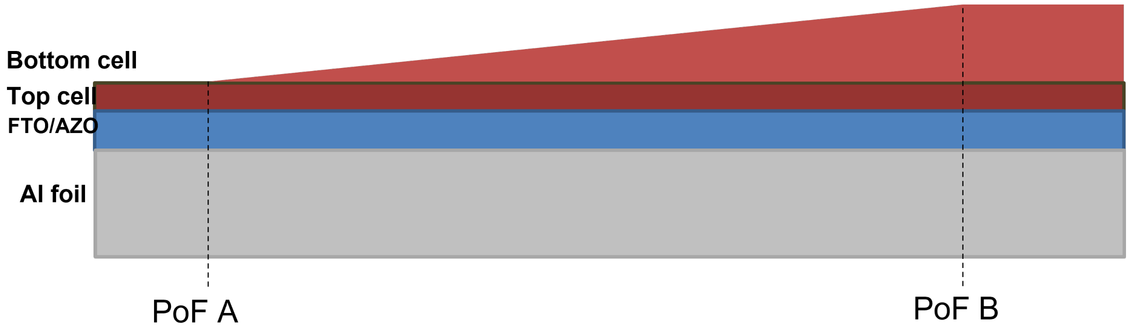

Figure 6.25: Schematic diagram of continuous variable thickness series for bottom cell deposition

Furthermore, the CVT analysis follow the Lambert Beer law which suggest with increasing absorbing layer volume, the current densities in the cell should increase. This is due to fact more light can be absorbed resulting in more generation of electron hole pair. This trend should be clearly seen in the single junction solar cell. For the tandem solar cell an EQE measurement needs to be done to understand the current densities of individual solar cells.

The CVT series in this work was used to understand the bottom and top cell depositions. This analysis would give insights on the performance of each zone on the quality of the cell. Firstly, the single junction solar cell based on a-Si:H fabricated in September 2021 are analyzed using the CVT. Furthermore, August run is analyzed on the CVT for the bottom cell deposited on the top cell.

### 6.3.1 Single junction CVT

The September run fabricated in HyET Solar was used to understand the top cell CVT performance. Here, the varying thickness solar cell from different PoF were fabricated using the CoF technique as discussed in Section 3.2. The different PoF's were from the different zones from the PECVD tool as seen from the Figure 6.26. The PoF are selected in such a way that the position is in the middle of the zone. Two different types of varying area solar cells were produced: 5 cm$^2$ and 2.5 cm$^2$. Furthermore, it is assumed that each zone deposits 60 nm of the intrinsic a-Si:H layer.

As seen from the Figure 6.26 the CVT series start from Zone 3 (Z3) which deposits around 30 nm of the intrinsic a-Si:H layer. The current densities were between 2 mA/cm$^2$ and 3 mA/cm$^2$. This is expected as a very thin intrinsic layer will have very low absorption which will not be generating the current well enough. Followed by Zone 3 is the Zone 4 (Z4) which should have Zone 3 thickness plus half of the Zone 4 thickness. The expected thickness of intrinsic layer for this PoF is around 90 nm. Here, the current densities increase considerably from the last zone. The large current densities suggest Lambert Beer relation for the deposition. Similarly, for Zone 5 (Z5) 12 mA/cm$^2$ are observed. This is accordance with the Lambert Beer law. Finally, in Zone 6 (Z6) the current densities start to get saturated. The current densities remain at 12 mA/cm$^2$. For the last Zone (Z7) the current densities increase marginally to 13 mA/cm$^2$. The expected thickness is 270 nm at Z7. Hence, using the CVT the Lambert Beer relation for the single junction amorphous silicon solar cell was understood.

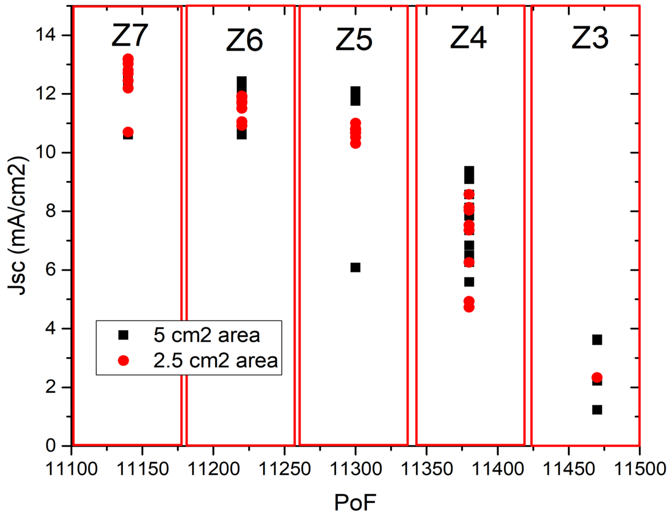

Figure 6.26: Current densities generated from the CVT single junction measurement

To conclude, the Lambert Beer relation was followed for the single junction amorphous silicon solar cell deposition. This experiment used the same recipe for the top cell deposition in a micromorph solar cell.

### 6.3.2 Micromorph Bottom cell CVT

The bottom cell of the micromorph solar cell fabricated in the August run at HyET Solar was analyzed with the CVT approach as seen in Section 6.3.1 to understand the deposition of nc-Si:H intrinsic in each zone of PECVD. As already discussed from the EQE measurements in the Section 6.2.1 the short circuit densities measured from the EQE results were low. The solar cells were fabricated using the SuperCoF technique as discussed in Chapter 5. These results are analyzed in similar fashion as that of the single junction CVT series discussed in Section 6.3.1. The main objective is to understand where the losses in the J$_{sc}$ are occurring. Finally, to understand if the bottom cell deposition follows the Lambert Beer relation.

The PoF for each Zone against the short circuit current densities are plotted in Figure 6.27. Here, each zone would we contributing to 400 nm of thickness since the expected thickness of the intrinsic layer in the bottom cell is 2000 nm. Starting with Zone 3 (Z3) in the figure, the J$_{sc}$ observed were around 2.5 mA/cm$^2$ to 3 mA/cm$^2$. These low current densities are due to thin absorber layer. Followed by Zone 3 is Zone 4 (Z4) where the expected thickness is around 450 nm at the first measurement PoF. Here, the J$_{sc}$ were around 4.5 mA/cm$^2$. In the same zone at another PoF near the center of the zone, the J$_{sc}$ measured were above 5.5 mA/cm$^2$, while reaching a maximum of 6 mA/cm$^2$ for some of the cells.

According to the Lambert Beer law the expected J$_{sc}$ after the Zone 4 should increase. This is due to increasing the absorber layer thickness. However, in Zone 5 (Z5) the current densities are in the same range as the Zone 4. The J$_{sc}$ observed in the Zone 5 is around 6 mA/cm$^2$. Around the full thickness of 1200 nm of Zone 5 we can start seeing the trend in decrease in the current densities as shown at the end of the zone in the Figure 6.25. The Zone 6 follows the Zone 5 deposition which shows a decreased J$_{sc}$ to about 5.5 mA/cm$^2$. This decrease in the current densities suggests problem with deposition as the expected trend of increase of current densities with increasing absorber thickness is not followed. Furthermore, as we move to Zone 7 (Z7) a further decrease in the short circuit current densities are observed. At the end of the full thickness of the stack at around 1800 nm in the middle of the Z7 the J$_{sc}$ observed were around 5 mA/cm$^2$. This further decrease in J$_{sc}$ from Zone 5 suggests that the deposition done under the August run for some of the zones is not nanocrystalline.

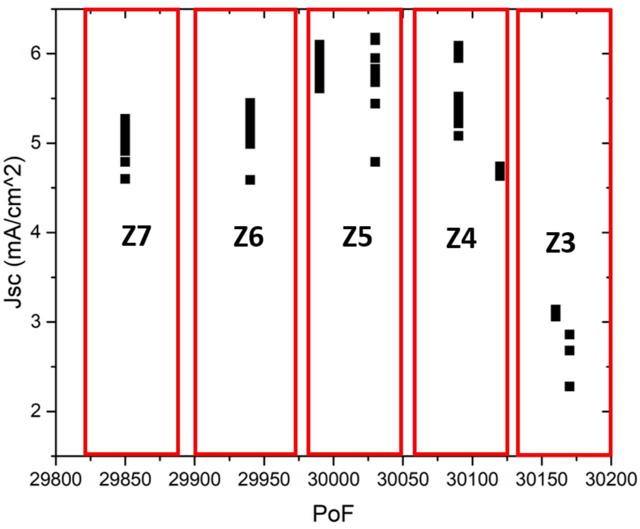

Figure 6.27: Current densities generated from the CVT bottom cell tandem solar cell measurement

The Eqe measured for the CVT bottom cell are shown in the Figure 6.28. Here, it can be seen that Zone 3 provides a noisy measurement for the bottom cell EQE due to thin intrinsic nc-Si:H layer. The Zone 4 shows the highest EQE but the shape of the EQE suggest too amorphous behaviour observed. Similar trends are shown in Zone 5 where the EQE drops further. As we go to a thicker absorber layer the EQE in Zone 6 and Zone 7 drops even further suggesting some of the zones of the PECVD deposition to be too amorphous. Till this point of the work the hypothesis for the bottom cell does suggest amorphous behaviour, however, the exact zone contributing to the amorphous deposition is still not understood.

To understand the exact contribution of each zone on the deposition of the bottom cell of the August run, the case studies from the ASA study are used. Here in Figure 6.29 it can be seen that Case 2 resembles most to the EQE results measured from the Zone 4 or Zone 5. The Case 2 of the ASA study represented the case where 650 nm of each layer of nc-Si:H/a-Si:H/nc-Si:H were deposited. Since, the comparison is between a single junction nc-Si:H based solar cell and tandem solar the EQE differs a bit. Furthermore, since the ASA case studies used 3 different zones instead of the actual 5 used in the PECVD tool the EQE curves do not overlap.

To conclude, on the nature of Zone 4 being amorphous and not Zone 5, the Case 3 simulation from the ASA is compared with the measured EQE as shown in the Figure 6.29. The Case 3 from the ASA simulation involves a nc-Si:H/nc-Si:H/a-Si:H structure. If the EQE curve of Case 3 overlapped with the Zone 5 then it could have concluded that Zone 5 is also amorphous. However, that is not the case observed from the results.

Overall, the Zone 5 does not completely overlap with the Case 2 curve, but still a reasonable fit can be seen which suggest that Z4 too be the problems causing the low short circuit current densities in the Zone 5 of the CVT deposition. This is possible since in Zone 4 deposition without the nc-Si:H, the amorphous material deposited can still collect electrons and holes. However, once the Zone 5 is deposited on top of Zone 4 the electron hole pair collection becomes difficult and reduction in the $J_{sc}$ can be seen. An initial observation was to understand that Zone 5 is creating the problem based on the CVT analysis but a detailed simulation of ASA suggest that it is Zone 4 that is too amorphous.

## 6.4 Results

The final results from the Simulation and the August run tandem solar cells measurement are discussed in this section. From the discussion of the previous section it is evident that Zone 4 is too amorphous. From the mass flow controller calibration data the silane dilution ratios of all the zones were calculated. The dilution ratios found for the Zone 4 and Zone 6 were greater than 1 suggesting too amorphous

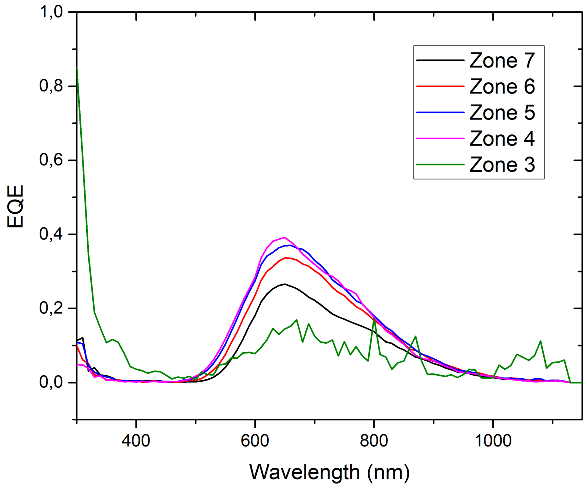

Figure 6.28: EQE results from the CVT bottom cell series from the August run

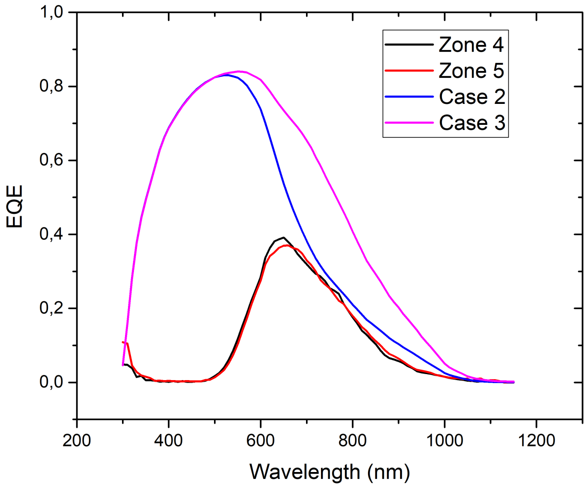

Figure 6.29: Comparison of EQE results from the CVT bottom cell series from the August run (Z4 and Z5) and Case 2 and Case 3 from ASA simulation

material in both the zones. Hence, to have better insights into the bottom cell deposition a cross-sectional imaging on SEM was conducted. Figure 6.30 show the top and bottom cell deposition under Setting 1 conditions. In the blue squares are the thickness of the various zones shown in the figure. It is assumed that each zone is depositing a thickness of 400 nm.

It can be seen from the cross-sectional image that Z4 is amorphous. It is based on the difference in the contrast of amorphous and nanocrystalline silicon material. The region near the Z4 shows typical a-Si:H features. However, it can also be seen that around the Z6 there is a transition from the nanocrystalline to amorphous material.

Finally, to validate the theory, a model in ASA was simulated. Here using the insights generated from the discussion, a nc-Si:H based single junction solar cell stack was modelled as shown in Appendix C. The stack consists of nc-Si:H/a-Si:H/nc-Si:H/a-Si:H/nc-Si:H intrinsic layer each with a thickness of 400 nm. The idea behind the stack is to mimic the bottom cell deposited in the August run with Zone 4 and Zone 6 being amorphous. the Figure 6.31 shows the photogenerated carriers for the simulation

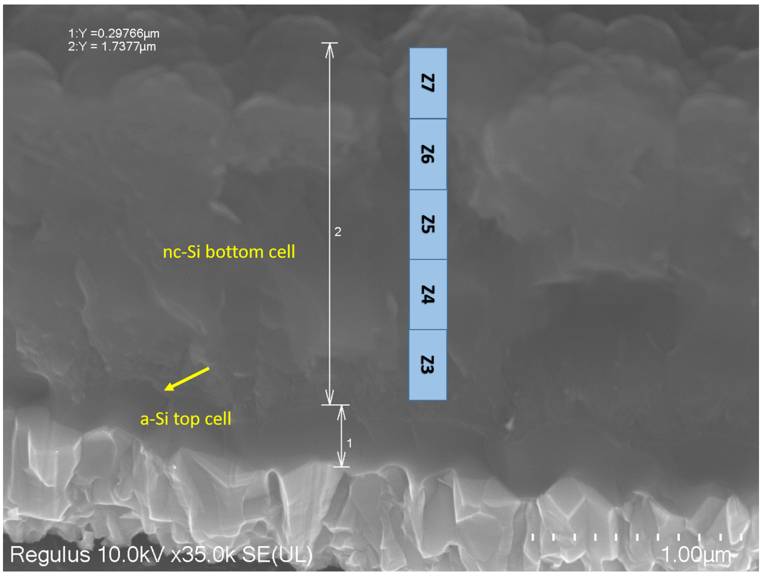

Figure 6.30: SEM cross-section of August run Setting 1

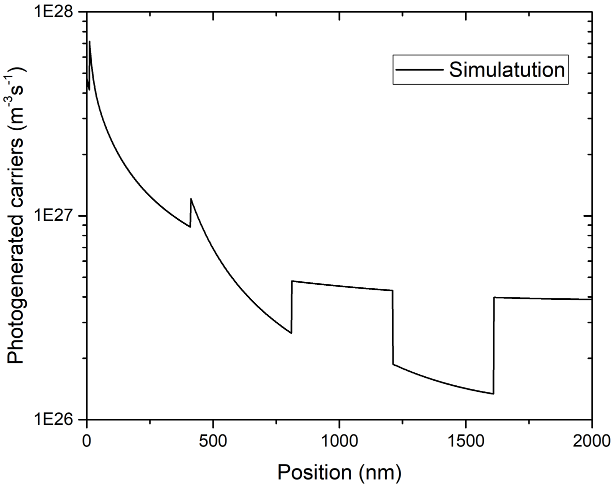

Figure 6.31: Photogenerated carriers for the nc-Si:H/a-Si:H/nc-Si:H.a-Si:H/nc-Si:H model developed for the simulation of the August run effect

done. The effect of the CVT Zone 4 can be explained by understanding the photogenerated carriers. It can be observed from the figure that the carriers generated at the end of Zone 4 due to a-Si:H can contribute to the current densities. However, the Zone 5 is not contributing to the current densities. It is due to this effect the Zone 4 showed better results although it was amorphous. Hence, based on the mass flow controller measurements, the SEM cross-section imaging and the ASA simulation results, it was concluded that the problem with August run bottom cell was with Zone 4 and Zone 6 being too amorphous.

The EQE results from the simulation model developed are compared with the measurement of the bottom cell of Setting 1 from the August run. The Figure 6.32 shows the final results from the comparison. Here it can be seen that when an a-Si:H layer of 400 nm is introduced after the Z5 deposition, the two EQE curves almost overlap. This provides better results from the Case 2 developed in the initial part of the chapter. Hence, the theory of Zone 4 and Zone 6 being too amorphous can be validated from the graph.

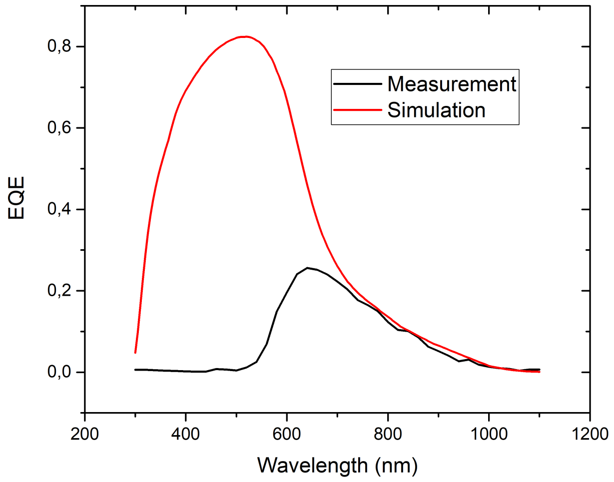

Figure 6.32: Final results from the EQE measurement from the Setting 1 August run tandem solar cells and ASA simulation

## 6.5 Conclusion

To fabricate micromorph solar cell various parameters need to be optimized. The last few tandem2production runs at HyET Solar focused on developing high performance tandem devices. However, due to deposition problems in the PECVD tool, limited performance was achieved in the tandem cells. This chapter addressed the problems of last few runs in HyET Solar to optimize the production of micromorph solar cells on aluminum substrate.

Firstly, a study based on ASA software was conducted to understand the effect of inclusion of a-Si:H layers in the nc-Si:H structure. Here, a stack of single junction nc-Si:H based solar cell was used. Finally, the results from the study show that the bottom cell deposition is sensitive to first growth layer in the solar cell. If the first layer deposited is too amorphous then the whole cell shows amorphous behaviour. Hence, Zone 3 in the PECVD tool becomes sensitive for the growth of micromorph cell.

Furthermore, the study also suggested that a amorphous layer at the end of the nanocrystalline layer does not affect the performance of the solar cell. Hence, if the Zone 7 becomes too amorphous, after a certain thickness of nanocrystalline, it should not affect the performance of the device.

Moreover, the August runs were analyzed based on EQE performance and JV parameters for two different settings with different silane flows in the Zone 5, Zone 6 and Zone 7. It can be seen that a higher silane flow results in too amorphous material in some of the zones and hence a lower silane flow is preferred. In the performance of the two settings, the one with lower silane flows showed better $V_{oc}$. Furthermore, the short current densities of each zone based on CVT were analyzed. It was shown that Zone 4/Zone 5 could be the problem for the low bottom cell performance of the August run.

Based on the ASA studies developed and the EQE measurements, the problem was concluded to be in Zone 4 which prevents the growth of nanocrystalline material. Furthermore, based on the mass flow controller measurements and SEM cross-section imagine Zone 6 was also understood to be amorphous. This theory was finally validated using the ASA model simulation results.

# Chapter 7

# Conclusions and outlooks

This thesis investigated various procedures to optimize the production process of thin film flexible solar cells. To reach the desired goals of FlamingoPV and develop a-Si:H/nc-Si:H and a-Si:H/nc-Si:H/nc-Si:H based solar cells the production process needs to provide high yield solar cells with faster learning cycles. This chapter discusses the most important conclusions from to this work that can help reach the goals. Furthermore, some recommendations are discussed for further research in this field.

## 7.1 Conclusion

The first problem of low yield of lab samples produced at HyET Solar has been studied. The theory of p-i-p shunt model was investigated to understand the effect of diffusion of Aluminium in the n-type silicon layers. The hypothesis suggested if the AZO layer is not optimized in terms of thickness then the diffused Al can counter-dope the n layer. To understand this effect a experiment was conducted where two stacks of back contact one with AZO and without AZO were sputtered. The diodes were then annealed and compared for the shunt resistance. It was concluded that the AZO layer is essential for high shunt resistance as the samples with just the Al layer showed low shunt resistance with a larger spread in the results. However, the diodes with the AZO showed better shunt resistance but still considerably low. After annealing the shunt resistance decreased marginally for the diodes with AZO/Al as the back contact. It was decided due to changes in the sputtering tool over years at HyET Solar the AZO layer thickness and properties were not optimized. Hence, a design of experiment was conducted to optimize the AZO layer based on electrical and optical properties.

The design of experiment was based on two factor two level screening for RF power and sputtering pressure. Using the spectroscopic ellipsometer the thickness was calculated. The current baseline sputtering time used at HyET Solar was optimized for 70 nm of AZO. Moreover, the ellipsometer measurements suggested higher sputter pressure and higher RF power provide the best refractive index values. The refractive index values were used in GenPro4 to understand the absorption in the intrinsic layer of the single junction. The Setting 1 which is the baseline setting with high pressure and low power conditions proved to provide the highest absorption in the intrinsic layer. Furthermore, spectrophotometer suggested lower sputter pressure to be ideal for lower absorption and current losses. It was concluded from Hall effect measurement that lower sputtering pressure provide better electrical properties. Finally, the settings were used to fabricate diodes, which were measured for shunt resistances. It could be seen that for better shunt resistances a higher power and higher sputter pressure provides the ideal growth of a dense and compact film. To conclude the experiment, matching the desired electrical and optical properties is a complex task as one might vary inversely with the other. Hence, based on the GenPro4 results the baseline setting was selected as the final sputtering conditions for future depositions.

The monolithic series interconnection process has been a bottleneck in the production of the lab samples at HyET Solar. Moreover, there is no standard laser power settings for the lab scale tandem or triple junction solar cells. Hence the concept of SuperCoF (Super Cell on Foil) was developed to ensure faster learning cycles for the lab line. Two approaches based on different types of contacting were developed. The first one involved contacting through a copper tape, while the second one involved partially laminating the cell and then contacting the back contact directly. The first approach was chosen to be the standard one based on the ease of doing step by step JV measurements. Furthermore, a series of triple junctions with two different types of back contact based on AZO/Al and ZAZAl were processed as SuperCoF. The results from the triple junction series are preliminary as the current matching was not done for the ZAZAl configuration. Various problems in the processing line were observed which lead to low yield of the triple junction series.

The PECVD tool at HyET Solar involves deposition using different zones. Based on the Lambert Beer relation it is expected that with increasing thickness the short circuit current densities increase. However, based on the CVT bottom cell series this was not observed. Furthermore, the performance of full stack of August run from Setting 1 and Setting 2 were too low suggesting amorphous layer in the bottom cell. Since, there are 5 zones in the PECVD tool, the exact zone could not be identified. Hence, a case study was carried out using the electrical simulation on ASA. The case study suggested the sensitivity parameters for the bottom cell deposition. It was understood that the first layer of the bottom cell deposition is crucial for the nanocrystalline silicon layers to grow. The last layer deposited under the Zone 7 may not be a problem if the proceedings layers are thick enough with nanocrystalline silicon characteristics.

Furthermore, the problem of August run was analyzed using the ASA simulation. From the information of the SEM analysis and the calibration of the mass flow controllers, it was understood that Zone 4 and Zone 6 are too amorphous. The calibration data from the mass flow controller suggested too high silane dilution ratio for the zones which might the reason for being too amorphous. Finally, based on this information a ASA model was developed for simulating the effect of zone 4 and zone 6 amorphous nature. The EQE generated from the simulation and the measurement overlapped proving the hypothesis of amorphous nature of the Zone 4 and Zone 6.

## 7.2 Outlooks

The conducted research highlighted the importance of optimization of the production process of the thin film flexible solar cell. To reach higher efficiencies and lifetime of the solar panels the production line needs to be optimized for faster learning cycles to develop more complex solar cell architectures. The following section will highlight some outlooks for future research that can further optimize the production process.

Firstly, to understand the losses due to open circuit resistance the lab scale line needs to be optimized. This was done in this work by optimizing the sputtering process. However, the sputtering optimization was not analyzed for open circuit resistance. This can be improved by fabricating SuperCoF for the different settings and measuring them for the open circuit resistance. This will help to improve the performance of solar cells and understanding the effect of back contact sputtering on the open circuit resistance. Furthermore, a SEM or TEM cross-sectional imaging could be done to understand the morphology of the film deposited.

Secondly, the SuperCoF series need to standardized for single and triple junction solar cells. The problem with single junction solar cells is low shunt resistance which can effect the performance of the SuperCoF. Although the first batches of triple junctions were processed as SuperCoF, however, the yield of the performance was very low. This can be improved with more cells processed for the triple junctions. The lamination and etching process needs to be standardized as well.

Finally, the mass flow controllers at the PECVD tool need to be calibrated more frequently. This resulted in problems in the August run. Furthermore, the silane dilution ratios need to be optimized for the deposition in the various zones as too high dilution ratios can result in too amorphous material. To develop standard recipe for the bottom cell deposition further experimentation needs to be done. The cells can be processed as SuperCoF as still there is no standard laser power for the micromorph solar cell. Finally, based on the improvements in the production line we can expect further growth in improving the efficiency of the solar cells produced at HyET Solar.

# Appendix A

# GenPro4 code for the sputtering optimization

```
clear Lay Int
%===LAYERS===
Lay(1).med = 'air';         Lay(1).thi = inf;
% INTERFACE 1
Lay(2).med = 'FTO';         Lay(2).thi = 0.700;
%INTERFACE 2
Lay(3).med = 'a-Si(i)';     Lay(3).thi = 0.300;
%INTERFACE 3
Lay(4).med = 'air';         Lay(4).thi = inf;

%===INTERFACES===        coatings are part of the interface
load('FactoryBaseline.mat');                    %Baseline TEXTURING

% Interface 1: between layer 1 and 2 (air/FTO) 0.001 = 1 nm
% TEXTURING
Int(1).model = 'wave';
Int(1).Z = -FactoryBaseline*10e-3;;
Int(1).xy = [40,40];


Int(1).coat(1).med = 'FTO'     Int(1).coat(1).thi = 0.700;
Int(2).coat(1).med = 'AZO';      Int(2).coat(1).thi = 0.020;
Int(2).coat(2).med = 'a-SiC(p)'; Int(2).coat(2).thi = 0.010;

%interface 2: between layer 2 and 3 (a-Si/air)

Int(3).coat(1).med = 'a-Si(n)';     Int(3).coat(1).thi = 0.020;
Int(3).coat(2).med = 'AZOSetting1'; Int(3).coat(2).thi = 0.070;
Int(3).coat(3).med = 'Al';          Int(3).coat(3).thi = 0.300;    %rear

%Note: interference occurs in 'coatings', not in 'layers'.
%===
S.wav = 0.300:0.005:1.000;
[Lay,Int,out] = GENPRO4(Lay,Int,S);        %both 'Lay' and 'Int' are input
```

# Appendix B

# Dark JV measurements

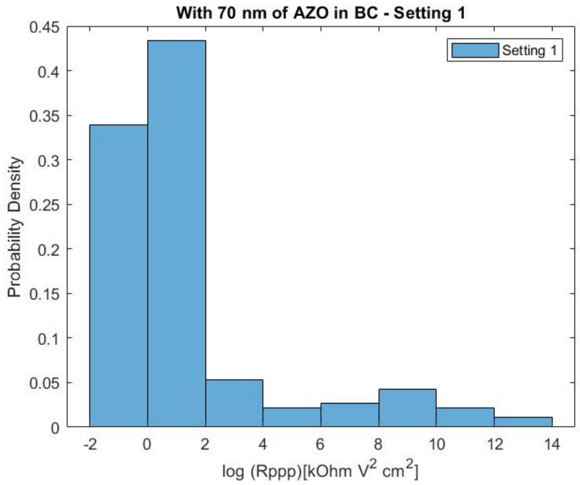

Figure B.1: Dark JV measurements for diodes for Setting 1

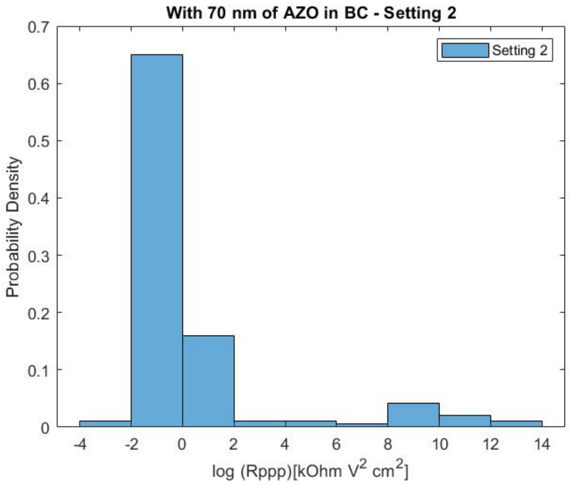

Figure B.2: Dark JV measurements for diodes for Setting 2

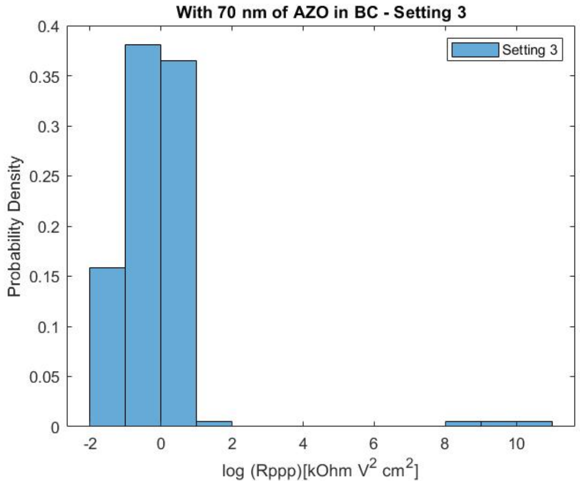

Figure B.3: Dark JV measurements for diodes for Setting 3

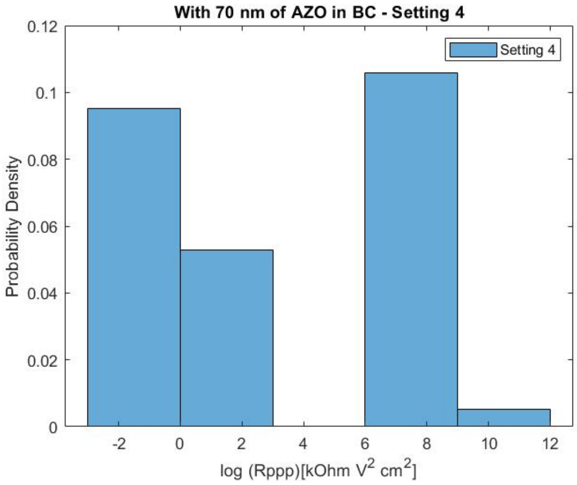

Figure B.4: Dark JV measurements for diodes for Setting 4

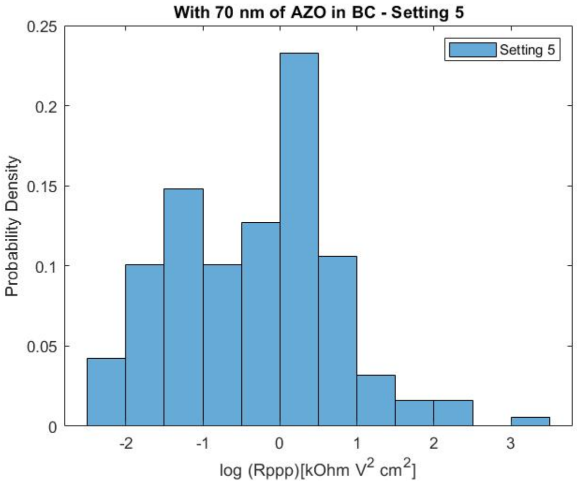

Figure B.5: Dark JV measurements for diodes for Setting 5

# Appendix C

# ASA code for simulating the August run effect

```
C  DEVICE DEFINITION;
layers          electrical=7 front=2 back=2;
grid[f.1]       d=700e-9;                           C  FTO (700 nm);
grid[f.2]       d=20e-9;                        C  AZO (20 nm);
grid[1]         d=10e-9 spaces=20;              C  nc-SiOx(p) (20 nm);
grid[2]         d=400e-9 spaces=500;    C  nc-Si(i)(300 nm);
grid[3]         d=400e-9 spaces=200;    C  a-Si(i) (300 nm);
grid[4]         d=400e-9 spaces=200;    C  nc-Si(i) (300 nm);
grid[5]         d=400e-9 spaces=200;    C  a-Si(i) (300 nm);
grid[6]         d=400e-9 spaces=200;    C  nc-Si(i) (300 nm);
grid[7]         d=20e-9 spaces=20;      C  nc-SiOx(n) (20 nm);
grid[b.1]       d=70e-9;                        C  AZO (70 nm);
grid[b.2]       d=300e-9;                           C  Al (300 nm);

C OPTICAL PARAMETERS OF LAYERS AND INTERFACES;

optical[f.1]    lnk.file=tud_FTO.in;    C FTO;
optical[f.2]    lnk.file=AZO.in;                C AZO;
optical[1]      lnk.file=nc-SiOx(p).in;     C p-layer;
optical[2]      lnk.file=nc-Si(i).in;       C i-layer;
optical[3]      lnk.file=a-Si(i).in;            C i-layer;
optical[4]      lnk.file=nc-Si(i).in;           C i-layer;
optical[5]      lnk.file=a-Si(i).in;            C i-layer;
optical[6]      lnk.file=nc-Si(i).in;       C i-layer;
optical[7]      lnk.file=nc-SiOx(n).in;     C n-layer;
optical[b.1]    lnk.file=AZO.in;                C AZO;
optical[b.2]    lnk.file=Al.in;                 C Al back contact;


C INTERFACE TEXTURING;
interface[i.2]  afm.file=AFM_FTO.in AFM.size=40e-6;
interface[i.2]  adf.s.rf=cossq adf.s.rb=cossq adf.s.tf=cossq adf.s.tb=cossq
                                adf.h.rf=cossq adf.h.rb=cossq adf.h.tf=cossq adf.h.tb=cossq;
interface[i.3]  afm.file=AFM_FTO.in AFM.size=40e-6;
interface[i.3]  adf.s.rf=cossq adf.s.rb=cossq adf.s.tf=cossq adf.s.tb=cossq
                                adf.h.rf=cossq adf.h.rb=cossq adf.h.tf=cossq adf.h.tb=cossq;
interface[i.11] afm.file=AFM_FTO.in AFM.size=40e-6;
interface[i.11] adf.s.rf=cossq adf.s.rb=cossq adf.s.tf=cossq adf.s.tb=cossq
                                adf.h.rf=cossq adf.h.rb=cossq adf.h.tf=cossq adf.h.tb=cossq;

C MATERIAL PARAMETERS OF LAYERS;

```

```
bands[1]        e.mob=1.90 chi=4.000 nc=4.0E+26 nv=4.0E+26 epsilon=11.9;
bands[2]        e.mob=1.12 chi=4.000 nc=2.5E+25 nv=2.5E+25 epsilon=11.9;
bands[3]        e.mob=1.70 chi=4.000 nc=2.0E+26 nv=2.0E+26 epsilon=11.9;
bands[4]        e.mob=1.12 chi=4.000 nc=2.5E+25 nv=2.5E+25 epsilon=11.9;
bands[5]        e.mob=1.70 chi=4.000 nc=2.0E+26 nv=2.0E+26 epsilon=11.9;
bands[6]        e.mob=1.12 chi=4.000 nc=2.5E+25 nv=2.5E+25 epsilon=11.9;
bands[7]        e.mob=1.75 chi=4.275 nc=4.0E+26 nv=4.0E+26 epsilon=11.9;

mobility[1]     mu.e=10.0e-4   mu.h=1.0e-4;
mobility[2]     mu.e=75.0e-4   mu.h=30.0e-4;
mobility[3]     mu.e=20.0e-4   mu.h=5.0e-4;
mobility[4]     mu.e=75.0e-4   mu.h=30.0e-4;
mobility[5]     mu.e=20.0e-4   mu.h=5.0e-4;
mobility[6]     mu.e=75.0e-4   mu.h=30.0e-4;
mobility[7]     mu.e=10.0e-4   mu.h=1.0e-4;

doping[1]       e.act.acc=0.20;
doping[7]       e.act.don=0.10;

variable        SIGMA1=0.7e-15 SIGMA2=SIGMA1 SIGMA3=0.7e-16;

C DENSITY OF STATES PARAMETERS OF LAYERS;
vbtail[all]     levels=50 c.neut=SIGMA1 e.range=0.9;
vbtail[1]       n.emob=1e28 e.char=0.085 c.pos=SIGMA2;
vbtail[2]       n.emob=2e25 e.char=0.015 c.pos=SIGMA2;
vbtail[3]       n.emob=4e27 e.char=0.050 c.pos=SIGMA2;
vbtail[4]       n.emob=2e25 e.char=0.015 c.pos=SIGMA2;
vbtail[5]       n.emob=4e27 e.char=0.050 c.pos=SIGMA2;
vbtail[6]       n.emob=2e25 e.char=0.015 c.pos=SIGMA2;
vbtail[7]       n.emob=1e28 e.char=0.090 c.pos=SIGMA2;

cbtail[all]     levels=50 c.neg=SIGMA1 e.range=0.9;
cbtail[1]       n.emob=1e28 e.char=0.080 c.neut=SIGMA2;
cbtail[2]       n.emob=1e26 e.char=0.010 c.neut=SIGMA2;
cbtail[3]       n.emob=2e27 e.char=0.027 c.neut=SIGMA2;
cbtail[4]       n.emob=1e26 e.char=0.010 c.neut=SIGMA2;
cbtail[5]       n.emob=2e27 e.char=0.027 c.neut=SIGMA2;
cbtail[6]       n.emob=1e26 e.char=0.010 c.neut=SIGMA2;
cbtail[7]       n.emob=1e28 e.char=0.080 c.neut=SIGMA2;


dbond[1]        n=1.0e23 e.neut=-0.65;
dbond[1]        levels=40 e.corr=0.2 d.e=0.144 e.range=5.0
                        ce.pos=3e-14 ce.neut=3e-15
                        ch.neg=3e-14 ch.neut=3e-15;
dbond[2]        n=3.0e20 e.neut=-0.70;
dbond[2]        levels=40 e.corr=0.2 d.e=0.144 e.range=5.0
                        ce.pos=3e-14 ce.neut=3e-15
                        ch.neg=3e-14 ch.neut=3e-15;
dbond[3]        n=2.0e21;
dbond[3]        levels=40 e.corr=0.2 d.e=0.144 e.range=5.0
                        ce.pos=3e-14 ce.neut=3e-15
                        ch.neg=3e-14 ch.neut=3e-15;
dbond[4]        n=3.0e20 e.neut=-0.70;
dbond[4]        levels=40 e.corr=0.2 d.e=0.144 e.range=5.0
                        ce.pos=3e-14 ce.neut=3e-15
                        ch.neg=3e-14 ch.neut=3e-15;
dbond[5]        n=2.0e21;
dbond[5]        levels=40 e.corr=0.2 d.e=0.144 e.range=5.0
                        ce.pos=3e-14 ce.neut=3e-15
                        ch.neg=3e-14 ch.neut=3e-15;
```

```
dbond[6]         n=3.0e20 e.neut=-0.70;
dbond[6]         levels=40 e.corr=0.2 d.e=0.144 e.range=5.0
                         ce.pos=3e-14 ce.neut=3e-15
                         ch.neg=3e-14 ch.neut=3e-15;
dbond[7]         n=1.0e24 e.neut=-1.25;
dbond[7]         levels=40 e.corr=0.2 d.e=0.144 e.range=5.0
                         ce.pos=3e-14 ce.neut=3e-15
                         ch.neg=3e-14 ch.neut=3e-15;


C GENERAL SETTINGS;
settings         newton gummel.starts=2 max.step.reduc=0;
settings         damp=6 max.iter=50;

model            amorphous;


C CALCULATING GENERATION PROFILE;

opticgen         spectrum=am15_300-1500.in gp3;
print            opticgen file=Opticgen_casec.gen;
print            absorption  file=Abs_casec.abt;
print            absorptance file=Abtc_casec.abs;


C CALCULATING SPECTRAL RESPONSE;
settings         sr.flux=1.0e20;
solve            equil;
solve            sr wl.start=300nm wl.step=5nm wl.end=1200nm illum;
print            sr file=EQE_casec.dat gnu;


C CALCULATING DARK J-V;
variable         v_start=-1.5 v_end=1.5;
model            poole.frenkel;
solve            equil;
print            bands file=band_casec.dat gnu;


C CALCULATING ILLUMINATED J-V (AM1.5 simulation);
variable         v_start=-1.5;
solve            equil;
solve            v.start=v_start v.end=v_end n.step=99 illum;
print            jv file=JV_casec.asp headers=false;
print            solpar file=PAR_casec.par;
```

# Bibliography

[1] V. Benda and L. Černá, “PV cells and modules – State of the art, limits and trends,” *Heliyon*, vol. 6, no. 12, 2020.

[2] P. Rappaport, “The Photovoltaic Effect and its Utilization,” *RCA Laboratories, Princeton NJ*, 1959.

[3] O. K. Simya, P. Radhakrishnan, A. Ashok, K. Kavitha, and R. Althaf, “Engineered nanomaterials for energy applications,” *Handbook of Nanomaterials for Industrial Applications*, pp. 751–767, 2018.

[4] T. Zhang and H. Yang, *High efficiency plants and building integrated renewable energy systems: Building-integrated photovoltaics (BIPV)*, 2018.

[5] G. Ali, M. Omar, A. K. Khan, and M. Faisal Nadeem, “Recent Challenges of Solar Cell Technologies; A Critical Analysis,” *RAEE 2018 - International Symposium on Recent Advances in Electrical Engineering*, 2018.

[6] G. Conibeer, “Third-generation photovoltaics,” *Materials Today*, vol. 10, no. 11, pp. 42–50, 2007.

[7] S. Sharma, K. K. Jain, and A. Sharma, “Solar Cells: In Research and Applications—A Review,” *Materials Sciences and Applications*, vol. 06, no. 12, pp. 1145–1155, 2015.

[8] K. L. Chopra, P. D. Paulson, and V. Dutta, “Thin-film solar cells: An overview,” *Progress in Photovoltaics: Research and Applications*, vol. 12, no. 2-3, pp. 69–92, 2004.

[9] K. Jäger, J. Lenssen, P. Veltman, and E. Hamers, “Large-area production of highly efficient flexible light-weight thin-film silicon pv modules.”

[10] B. Rech and H. Wagner, “Potential of amorphous silicon for solar cells,” *Applied Physics A: Materials Science and Processing*, vol. 69, no. 2, pp. 155–167, 1999.

[11] A. Shah, “Thin film silicon solar cells,” *EPFL Press*, 2010.

[12] A. Smets, K. Jäger, O. Isabella, R. van Swaaij, and M. Zeman, *Solar Energy: The physics and engineering of photovoltaic conversion, technologies and systems*. UIT Cambridge Limited, 2016.

[13] M. T. Boyd, S. A. Klein, D. T. Reindl, and B. P. Dougherty, “Evaluation and validation of equivalent circuit photovoltaic solar cell performance models,” *Journal of Solar Energy Engineering*, vol. 133, 3 2011. [Online]. Available: https://doi.org/10.1115/1.4003584

[14] E. M. Rodrigues, R. Melício, V. M. Mendes, and J. P. Catalão, “Simulation of a solar cell considering single-diode equivalent circuit model,” *Renewable Energy and Power Quality Journal*, vol. 1, pp. 369–373, 5 2011.

[15] S. Dongaonkar, K. Y, D. Wang, M. Frei, S. Mahapatra, and M. A. Alam, “On the nature of shunt leakage in amorphous silicon p-i-n solar cells,” *IEEE Electron Device Letters*, vol. 31, pp. 1266–1268, 2010.

[16] S. Dongaonkar, Y. Karthik, S. Mahapatra, and M. A. Alam, “Physics and statistics of non-ohmic shunt conduction and metastability in amorphous silicon p-i-n solar cells,” *IEEE Journal of Photovoltaics*, vol. 1, pp. 111–117, 2011.

[17] O. Breitenstein, J. P. Rakotoniaina, M. H. A. Rifai, and M. Werner, “Shunt types in crystalline silicon solar cells,” *Progress in Photovoltaics: Research and Applications*, vol. 12, pp. 529–538, 2004.

[18] S. Dongaonkar, J. D. Servaites, G. M. Ford, S. Loser, J. Moore, R. M. Gelfand, H. Mohseni, H. W. Hillhouse, R. Agrawal, M. A. Ratner, T. J. Marks, M. S. Lundstrom, and M. A. Alam, “Universality of non-ohmic shunt leakage in thin-film solar cells,” *Journal of Applied Physics*, vol. 108, 2010.

[19] M. S. Haque, H. A. Naseem, and W. D. Brown, “Aluminum-induced degradation and failure mechanisms of a-si:h solar cells,” *Solar Energy Materials and Solar Cells*, vol. 41-42, pp. 543–555, 1996.

[20] G. E. Nostrand and J. J. Hanak, “Method of removing the effects of electrical shorts and shunts created during the fabrication process of a solar cell,” Sep 1979.

[21] K. Rmkanans and J. Shewchun, “A better approach to the evaluation of the series resistance of solar cellst,” pp. 19–497.

[22] M. W. Denhoff and N. Drolet, “The effect of the front contact sheet resistance on solar cell performance,” *Solar Energy Materials and Solar Cells*, vol. 93, pp. 1499–1506, 9 2009.

[23] V. M. Airaksinen, “Silicon wafer and thin film measurements,” pp. 381–390, 1 2015.

[24] G. T. Koishiyev and J. R. Sites, “Impact of sheet resistance on 2-d modeling of thin-film solar cells,” *Solar Energy Materials and Solar Cells*, vol. 93, pp. 350–354, 3 2009.

[25] M. S. El-Eskandarany, “Introduction,” pp. 1–11, 2020.

[26] K. O. Ukoba, A. C. Eloka-Eboka, and F. L. Inambao, “Review of nanostructured nio thin film deposition using the spray pyrolysis technique,” *Renewable and Sustainable Energy Reviews*, vol. 82, pp. 2900–2915, 2 2018.

[27] H. O. Pierson, *Handbook of chemical vapor deposition : principles, technology, and applications*. Noyes Publications, 1999.

[28] S. M. Shang and W. Zeng, *Conductive nanofibres and nanocoatings for smart textiles*. Elsevier Ltd, 2013.

[29] G. Faraji, H. S. Kim, and H. T. Kashi, *Introduction*. Elsevier, 2018.

[30] R. J. Martín-Palma and A. Lakhtakia, *Vapor-Deposition Techniques*. Elsevier Inc., 2013.

[31] O. Kluth, G. Schöpe, J. Hüpkes, C. Agashe, J. Müller, and B. Rech, “Modified thornton model for magnetron sputtered zinc oxide: Film structure and etching behaviour,” *Thin Solid Films*, vol. 442, pp. 80–85, 2003.

[32] D. maree Kivell, “Microstructural control of zno films deposited by rf magnetron sputtering for ultrasound transducers,” 2013.

[33] A. M. Dagamseh, B. Vet, F. D. Tichelaar, P. Sutta, and M. Zeman, “Zno:al films prepared by rf magnetron sputtering applied as back reflectors in thin-film silicon solar cells,” *Thin Solid Films*, vol. 516, pp. 7844–7850, 2008.

[34] D. Song, A. G. Aberle, and J. Xia, “Optimisation of zno:al films by change of sputter gas pressure for solar cell application,” *Applied Surface Science*, vol. 195, pp. 291–296, 2002.

[35] A. M. Dagamseh, B. Vet, P. Šutta, and M. Zeman, “Modelling and optimization of a-si:h solar cells with zno:al back reflector,” *Solar Energy Materials and Solar Cells*, vol. 94, pp. 2119–2123, 2010.

[36] K. Choy, “Chemical vapour deposition of coatings.” [Online]. Available: www.elsevier.com/locate/pmatsci

[37] K. Gupta, N. K. Jain, and R. Laubscher, “Surface property enhancement of gears,” pp. 167–196, 2017.

[38] P. Babal, H. J. V. Veen, M. Workum, A. H. M. Smets, and M. Zeman, “Doped silicon oxide layers for tandem silicon solar cells,” *Renewable Energy and the Environment Optics and Photonics Congress*, 2012.

[39] J.-W. A. Schüttauf, “Amorphous and crystalline silicon based heterojunction solar cells,” 1980.

[40] S. N. Agbo, “Growth and characterization of thin film nanocrystalline silicon materials and solar cells,” 2012.

[41] J. Robertson, “Growth mechanism of hydrogenated amorphous silicon.” [Online]. Available: www.elsevier.com/locate/jnoncrysol

[42] A. Matsuda, “Growth mechanism of microcrystalline silicon obtained from reactive plasmas.”

[43] K. Dorywalski, I. Maciejewski, and T. Krzyżyński, “Spectroscopic ellipsometry technique as a materials characterization tool for mechatronic systems—the case of composition and doping concentration monitoring in sbn crystals,” *Mechatronics*, vol. 37, pp. 33–41, 8 2016.

[44] R. K. Kothandaraman, “Development of four-terminal devices utilising thin-lm solar cells.” [Online]. Available: http://repository.tudelft.nl/.

[45] S. Elzwawi, “Cathodic arc zinc oxide for active electronic devices,” 2015.

[46] V. Avrutin, N. Izyumskaya, and H. Morkoç, “Amorphous and micromorph si solar cells: Current status and outlook,” pp. 526–542, 2014.

[47] O. Isabella, J. Krč, and M. Zeman, “Modulated surface textures for enhanced light trapping in thin-film silicon solar cells,” *Applied Physics Letters*, vol. 97, 9 2010.